Global stability and control of swirling jets and flames

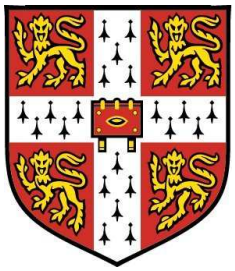

Ubaid Ali Qadri

Trinity College

University of Cambridge

A dissertation submitted for the degree of

Doctor of Philosophy

Department of Engineering
April 2013

This dissertation is the result of my own work and includes nothing that is the outcome of work done in collaboration, except where specifically indicated in the text. No part of this dissertation has already been, or is concurrently being, submitted for any degree, diploma or qualification.

This dissertation contains no more than 50,000 words and 80 figures.

.....
Ubaid Ali Qadri

Abstract

Large-scale unsteady flow structures play an influential role in the dynamics of many practical flows, such as those found in gas turbine combustion chambers. This thesis is concerned primarily with large-scale unsteady structures that arise due to self-sustained hydrodynamic oscillations, also known as global hydrodynamic instability. Direct numerical simulation (DNS) of the Navier–Stokes equations in the low Mach number limit is used to obtain a steady base flow, and the most unstable direct and adjoint global modes. These are combined, using a structural sensitivity framework, to identify the region of the flow and the feedback mechanisms that are responsible for causing the global instability. Using a Lagrangian framework, the direct and adjoint global modes are also used to identify the regions of the flow where steady and unsteady control, such as a drag force or heat input, can suppress or promote the global instability.

These tools are used to study a variety of reacting and non-reacting flows to build an understanding of the physical mechanisms that are responsible for global hydrodynamic instability in swirling diffusion flames. In a non-swirling lifted jet diffusion flame, two modes of global instability are found. The first mode is a high-frequency mode caused by the instability of the low-density jet shear layer in the premixing zone. The second mode is a low-frequency mode caused by an instability of the outer shear layer of the flame. Two types of swirling diffusion flames with vortex breakdown bubbles are considered. They show qualitatively similar behaviour to the lifted jet diffusion flames. The first type of flame is unstable to a low-frequency mode, with wavemaker located at the flame base. The second type of flame is unstable to a high-frequency mode, with wavemaker located at the upstream edge of the vortex breakdown bubble. Feedback from density perturbations is found to have a strong influence on the unstable modes in the reacting flows. The wavemaker of the high-frequency mode in the reacting flows is very similar to its non-reacting counterpart. The low-frequency mode, however, is only observed in the reacting flows. The presence of reaction increases the influ-

ence of changes in the base flow mixture fraction profiles on the eigenmode. This increased influence acts through the heat release term.

These results emphasize the possibility that non-reacting simulations and experiments may not always capture the important instability mechanisms of reacting flows, and highlight the importance of including heat release terms in stability analyses of reacting flows.

Contents

Contents v

Preface x

1 Introduction 1

1.1 Context . . . 1
1.2 Background . . . 3
1.3 Scope of this work . . . 9

2 Mathematical formulation 13

2.1 Governing equations . . . 13
2.2 Linear global stability analysis . . . 17
2.3 Sensitivity to internal feedback . . . 18
2.3.1 Derivation . . . 19
2.3.2 The wavemaker . . . 23
2.4 Sensitivity to a control force . . . 24
2.4.1 Sensitivity to steady forcing . . . 25
2.4.2 Sensitivity to unsteady forcing . . . 28
2.5 Extension to reacting flows . . . 28
2.6 Local stability analysis . . . 36

3 Numerical implementation 39

3.1 Details of the code . . . 39
3.2 Base flow . . . 41
3.2.1 Procedure . . . 41

3.2.2 Boundary Conditions 42
3.3 Direct and adjoint global modes 43
3.3.1 Procedure 43
3.3.2 Boundary conditions 45
3.4 Adjoint base flow 47
3.5 Local stability analysis 47

4 Passive control of global instability in low-density jets 49
4.1 Introduction 49
4.2 Flow configuration 51
4.3 Global stability and structural sensitivity 53
4.4 Sensitivity to a control force 55
4.5 Passive control using an axisymmetric control ring 57
4.5.1 The effect of an adiabatic control ring 57
4.5.2 The effect of a heated control ring 60
4.6 A physical interpretation of the control in terms of the modification of the base flow 61
4.6.1 The effect of a drag force in the shear layer 65
4.6.2 The effect of a heat source in the jet core 66
4.7 Summary 67
4.8 Appendix 69

5 Spiral vortex breakdown: its physical origin and control 73
5.1 Introduction 73
5.2 Flow configuration 77
5.3 Validation 78
5.4 Global stability and structural sensitivity 82
5.4.1 Helical mode, $m = -1$ 82
5.4.2 Double-helical mode, $m = -2$ 96
5.5 Sensitivity to a control force 100
5.5.1 Helical mode, $m = -1$ 100
5.5.2 Double-helical mode, $m = -2$ 102
5.6 Summary 103

6 Global stability and control of swirling jets 107
6.1 Introduction . . . 107
6.2 Flow configuration . . . 110
6.3 Before vortex breakdown . . . 112
6.3.1 Global stability . . . 112
6.3.2 Local stability . . . 116
6.4 Bubble state . . . 119
6.4.1 Global stability and structural sensitivity . . . 121
6.4.2 Sensitivity to a control force . . . 122
6.5 Cone state . . . 124
6.5.1 Global stability and structural sensitivity . . . 125
6.5.2 Sensitivity to a control force . . . 125
6.6 The effect of variable-density and heat addition . . . 128
6.7 Summary . . . 128

7 Global stability and control of a lifted jet diffusion flame 133
7.1 Introduction . . . 133
7.2 Flow configuration . . . 136
7.3 Global stability and structural sensitivity . . . 137
7.3.1 Comparison to previous studies . . . 142
7.4 Sensitivity to a control force . . . 146
7.5 Summary . . . 149

8 Global stability and control of swirling diffusion flames 153
8.1 Introduction . . . 153
8.2 Flow configuration . . . 154
8.3 Swirling jet diffusion flame, without coflow . . . 155
8.3.1 Global stability and structural sensitivity . . . 155
8.3.2 Sensitivity to a control force . . . 160
8.4 Swirling diffusion flame, with strong coflow . . . 161
8.4.1 Global stability and structural sensitivity . . . 163
8.4.2 Sensitivity to a control force . . . 166
8.5 Summary . . . 168

9 Concluding remarks **171**

9.1 Summary of work completed 171

9.2 Main conclusions 174

9.3 Further work 175

References **179**

Preface

This thesis describes work that I have done over the last 3 and a half years on the development of the Low Mach Number Sensitivity (L'MaNS) code, and its subsequent use to study various non-reacting and reacting flow configurations. This work has been done under the supervision of Dr. Matthew Juniper at the Department of Engineering. I'd like to thank him for his guidance and supervision over, not only the 3 and a half years of my PhD, but also the preceding 2 years of my undergraduate degree here at Cambridge. I have benefited tremendously from his insight into physics, his approach to problem-solving and research, and his meticulous attention to detail. He has taught me the art of scientific writing, and I'd like to think that I now know the difference between 'that' and 'which'. Finally, I'd like to thank Matthew for the freedom he has given me in my research, and for his patience with my approach to work, which I think can most kindly be described as 'laid back'.

The jump from an engineering undergraduate degree to research on hydrodynamic stability was not easy, and I am grateful to the people that have helped me out along the way. In particular, I'd like to thank Dr. Gary Chandler, for his help during the early part of my PhD, and Dr. Chris Heaton, for providing me with a code that showed me how I could implement complex numbers in the L'MaNS code. In various parts of this thesis, a local stability analysis has been used to support the global stability analysis. I'd like to thank Dhiren Mistry and Matthew Juniper for performing this local stability analysis. A special mention must be made of *InstaFlow*, the local stability analysis tool that has been developed in this research group and continues to grow from strength to strength.

My time at Cambridge would not have been possible without the financial support of Trinity College - they have funded both my undergraduate and post-graduate studies, and I'd like to take this opportunity to thank them for this opportunity of a lifetime. I'm also grateful to the EPSRC and AIM Network, the Department of Engineering, and Trinity College for funding my attendance at numerous conferences around the world.

The computations were performed using the Darwin Supercomputer of the University of Cambridge High Performance Computing Service (http://www.hpc.cam.ac.uk/), and using the Stokes cluster at the Department of Engineering. I'd like to thank Peter Benie for help in setting up my accounts on Stokes and Darwin, and for help in resolving all those compiler issues and segmentation faults. Finally, I'd like to thank Dr. Outi Tammisola for letting me run simulations on her computer, whenever I needed a result urgently.

On a personal level, I'd like to thank my lab-mates, both past and present, for the relaxed working environment that made it a pleasure to go to work every day, and for their patience with my propensity to waste time. The lads at Devonshire Road deserve a mention for helping me maintain some sense of balance between my work and my social life over the last 2 years. Finally, I'd like to thank my family for their support and patience during the course of writing this thesis. Alhamdulillah, it's done now :)

1

Introduction

1.1 Context

The combustion of liquid and gaseous fossil fuels provides a large proportion of the energy required for transportation and electrical power generation in the world today. The mixing of the fuel with the oxidizer plays an important role in determining the efficiency of the combustion process. Good mixing leads to efficient combustion, which can reduce the operational and manufacturing costs involved.

Mixing has been defined, in Broadwell & Mungal (1991), as 'the process of diffusion of substances across intermaterial surfaces'. This process can be promoted by increasing the surface area that is available for diffusion, and by increasing the concentration gradients that drive diffusion. Both of these can be achieved by a process which Broadwell & Mungal (1991) quote as 'stirring': 'the mechanical process whereby fluids are distributed more uniformly within a given domain'. This, they note, 'is a purely kinematical aspect dependent on flow parameters', whereas 'mixing depends on material properties such as diffusivities'. [1]

[1] This distinction was first suggested by C. Eckart in Journal of Marine Research, VII, 3, 265 (1948).

Fuel injectors improve the rate of mixing through this 'stirring' mechanism. They are designed to produce turbulent flows with large velocity gradients (shear). These turbulent shear flows often have large-scale structures that are very efficient at stirring, stretching, and folding the fluid. These large-scale structures have been observed in non-reacting turbulent shear layers (Brown & Roshko, 1974), jets (Crow & Champagne, 1971), and wakes (Wygnanski *et al.*, 1986). In combustion systems, these large-scale structures can have a profound effect on the structure and stability of the flame. (Coats, 1996)

Swirl is imparted to flows in fuel injectors for two main reasons. Firstly, swirling jets have been found to have higher spreading rates and to produce better mixing between the jet fluid and the surrounding fluid compared to non-swirling jets (Panda & McLaughlin, 1994). Secondly, in combustion systems, swirl is used to stabilize the flame through the formation of a central recirculation zone (CRZ) that ensures a supply of fresh reactants to, and removal of hot products away from the flame front. This CRZ is caused by vortex breakdown, which occurs in highly swirling flows. In most situations, a large-scale unsteady helical mode, commonly referred to as the precessing vortex core (PVC), evolves around this CRZ. The review articles by Syred (2006) and Huang & Yang (2009) provide an extensive overview of the numerical and experimental evidence for these structures in practical combustion systems.

The unsteady hydrodynamic structures present in both swirling and non-swirling flows can also interact with other modes in the combustion system, such as the acoustics, to lead to complex instability behaviour. In particular, unsteady heat release from the flame can couple with pressure oscillations caused by the acoustics, leading to high-amplitude oscillations that are referrred to as thermoacoustic instability. This is a major challenge facing many gas-turbine manufacturers today. Chakravarthy *et al.* (2007) and Sivakumar & Chakravarthy (2008) have shown that the large-scale structures arising from the hydrodynamics can set the frequency of these thermoacoustic in-

stabilities. The exact relationship between the hydrodynamics and the thermoacoustic modes of instability is not known precisely and is still an area of current research. This thesis, however, is only concerned with the hydrodynamic instability.

Advances in computing power and diagnostic techniques have made it easier to understand the way flows behave. In contrast, understanding why they behave that way and how we might change that behaviour has not been as straightforward and forms the motivation for this thesis. In particular, this thesis is motivated by the aim of deriving sensitivity information that can aid designers. This sensitivity information includes identifying which regions of the flow are most influential in causing the large-scale hydrodynamic structures and how one might change the frequency and prominence of these structures by making small changes to the design.

1.2 Background

Although most practical applications feature flows that are turbulent, this thesis is concerned with large-scale unsteady structures that develop in laminar flows. Hydrodynamic instability can lead to unsteadiness in flows that have steady boundary conditions. This was first shown experimentally by Reynolds (1884) for flow in a pipe. He found that unsteady structures developed in the steady laminar flow in a pipe when the velocity of the water in the pipe was above a critical value. Around the same time, theoretical studies by Helmholtz and William Thomson (Lord Kelvin), on the effect of wind on a surface of water, and Lord Rayleigh, on the growth of sinusoidal perturbations on the surface of a liquid jet, laid the foundations for the use of linear stability analysis to study the response of steady laminar flows to small perturbations.

The stability of shear flows, which are particularly relevant for this thesis, was first investigated by Rayleigh (1880) for the case of inviscid flow between two fixed walls. The flow was assumed to be parallel, which means that it

was the same at each streamwise location. Here, Rayleigh derived the famous inflexion point theorem, which states that an inflexion point in the velocity profile is a necessary condition for the flow to be unstable. In doing so, he used the method of normal modes, which has since become the standard procedure of studying linear stability. The method consists of decomposing the perturbations into modes of different wavelengths and calculating the frequency with which these modes grow or decay. Typically, the analysis leads to an equation that relates the wavenumber (the inverse of the wavelength) and frequency of the perturbations. This equation is referred to as the dispersion relation for the flow. This dispersion relation is solved as a complex eigenvalue problem - the one-dimensional eigenfunction provides the shape of the mode, while the complex eigenvalue determines whether this mode grows or decays.

In the early 20th century, the method of normal modes was applied to study the stability of viscous parallel shear flows. This led to the Orr-Sommerfeld equations, which define an initial value problem that determines whether perturbations of a specified spatial wavelength grow or decay in time. The dispersion relation is solved for a complex frequency and real wavenumber. This analysis is referred to as a temporal stability analysis. The spatial analogue of this problem, which determines whether perturbations of a specified frequency grow or decay in space, was developed in the mid 20th century to study the instability of flows developing over space such as boundary layers. Here, the dispersion relation is solved for a real frequency and complex wavenumber. This analysis is referred to as a spatial stability analysis. A full review of these methods of analysis can be found in Drazin & Reid (1981).

In situations where perturbations may grow in both space and time, a purely temporal or purely spatial stability analysis may be insufficient to characterize the stability. The development of spatio-temporal stability theory resolved this by using the concept of absolute instability, which was originally developed in the field of plasma physics. A parallel flow is described as convectively unstable if the linear response to a localized impulse

spreads only downstream of the location of the impulse. In this case, the energy at the site of the impulse decays in the long time limit and the flow eventually returns to its base state. In contrast, a parallel flow is described as absolutely unstable if the linear response to a localized impulse spreads both upstream and downstream of the location of the impulse. In this case, the energy at the site of the impulse grows in the long time limit, and the impulse reponse dominates over the base state. In a spatio-temporal stability analysis, the dispersion relation is solved for complex frequency and complex wavenumber. These ideas and their application to shear flows are reviewed in detail by Huerre & Monkewitz (1990).

In many situations, flows are not parallel but evolve in the streamwise direction. In cases that are only weakly non-parallel, the WKBJ approximation can be used to extend the concept of absolute instability of parallel flows to non-parallel flows. This approximation states that the wavelength of the instability is much smaller than the spatial scale over which the base flow changes. The spatio-temporal stability can then be determined for each streamwise location of the flow, by assuming that the flow there is locally parallel and only varies in one spatial dimension. Such an analysis is, therefore, referred to as a local linear stability analysis.

Huerre & Monkewitz (1990) showed that the global behaviour of the flow is related to its local stability properties. If a sufficiently large region of the flow is absolutely unstable, the flow behaves as an oscillator. It supports self-sustained oscillations at a well-defined frequency. These self-sustained oscillations are known as global modes and arise from a purely hydrodynamic feedback loop (Chomaz *et al.*, 1988; Huerre & Monkewitz, 1985). A classical example of such a flow is the flow behind a cylinder. Such a flow is said to be linearly globally unstable. In contrast, if a flow is convectively unstable everywhere, the flow behaves as an amplifer. It is very sensitive to external perturbations and amplifies these disturbances spatially. A classical example of such a flow is a uniform density jet. Such a flow is said to be linearly globally stable.

For flows that are strongly non-parallel, a linear global stability analysis is more appropriate. This applies the normal mode approach to study the growth of two- and three-dimensional perturbations on top of a steady two- or three-dimensional base flow. Zebib (1987) and Jackson (1987) studied the linear global stability of two-dimensional viscous flow past a circular cylinder. They solved two-dimensional eigenvalue problems and obtained the growth rate, frequency, and the two-dimensional eigenfunction for the most unstable mode.

In many practical flows, the normal mode approach and most unstable eigenmode have been unable to explain experimental observations. For example, the normal mode approach predicts pipe flow and plane Couette flow to have no unstable eigenvalues for any flow velocity, whereas experimental observations clearly show unsteady behaviour beyond a critical Reynolds number. One explanation for this discrepancy has been the discovery that the linearized Navier–Stokes operator that governs the growth of the perturbations in viscous shear flows is non-normal (Butler & Farrell, 1992). This means that the linear eigenfunctions are not orthogonal to each other. They can, therefore, interact to produce perturbation growth that is greater than that predicted by the most unstable linear eigenmode. This is of particular importance to flows that are linearly globally stable because large transient growth can occur even though a normal-mode approach would predict that all perturbations should decay in the long time limit. (Schmid, 2007).

More precisely, though, a non-normal operator is one which does not commute with its adjoint. This is analogous to the concept of a non-normal matrix which does not commute with its conjugate transpose. The normal mode approach can be applied to the adjoint operator in the same way as the direct linear operator. Salwen & Grosch (1981) showed that the adjoint eigenfunctions of the Orr-Sommerfeld equations are bi-orthogonal with their direct linear counterparts. This means that for each linear eigenmode, there exists only one adjoint eigenmode that is non-orthogonal to it. This adjoint

eigenvalue is the complex conjugate of the direct linear eigenvalue.

A direct consequence of the non-normality of the linear operator is that the eigenvalues can be quite sensitive to small perturbations. This leads to the idea of the pseudospectrum of the linear operator (Trefethen *et al.*, 1993), which defines how the spectrum of eigenvalues changes for small perturbations to the linear operator. For flows with large non-normality, a small perturbation of the linear operator can produce a large modification of the spectrum. From a physical point of view, this means that a small change in the flow can change the global behaviour of the flow. This was demonstrated experimentally by Strykowski & Sreenivasan (1990) on the vortex shedding that arises in the wake behind a circular cylinder. By placing a small control cylinder in a suitable location, they were able to suppress the vortex shedding entirely. The same problem was first investigated numerically by Hill (1992) using a linear global stability analysis around the cylinder wake. He showed that the two-dimensional adjoint eigenfunction (or adjoint global mode) can be used to quantify the effect of steady and unsteady forces on the unstable eigenvalue.

The physical interpretation of the adjoint global mode is summarized nicely by Chomaz (2005). In a flow that is globally unstable and behaves as an oscillator, the adjoint global mode represents the initial condition that maximizes the amplitude of the direct global mode at any time, or equivalently, the sensitivity of the eigenvalue to external open-loop harmonic forcing. This may be useful for thermoacoustics as it can identify where the hydrodynamic mode is receptive to acoustic forcing, which produces velocity and pressure perturbations in the hydrodynamics. The adjoint global mode can be used to calculate the sensitivity of the eigenvalue to a small perturbation to the linear operator. This is called the structural sensitivity (Giannetti & Luchini, 2007) and physically, this can be used to identify the region of the flow that is most influential in determining the growth rate and frequency of the global mode. Giannetti & Luchini (2007) showed that this region, which they called the wavemaker, is given by the overlap of the

direct and adjoint global modes. [1] This is useful in understanding the inherent dynamics of the flow and the mechanisms that cause the self-sustained oscillations. When considering control of these oscillations, however, it is important to take into account that a control force will have an effect on the base flow as well as on the linear operator. This was recognized originally by Hill (1992), and described in more detail by Marquet *et al.* (2008*a*) for the cylinder wake. They calculated the sensitivity of the eigenvalue to arbitrary base flow modifications, and to steady forcing. This is expected to be most useful from a practical point of view to develop passive control and boundary modification strategies to promote or suppress the instability. These techniques have now been applied to a variety of flows that behave as oscillators, such as, the compressible flow behind axisymmetric bodies (Meliga *et al.*, 2010), the case of a jet impinging on a flat plate (Meliga & Chomaz, 2010), and planar wakes typically found in the paper-making industry (Tammisola, 2011). These techniques have also been applied to study flows that behave as amplifiers, and have also been used to derive reduced-order models of flows for closed-loop control. A review of these techniques and their applications can be found in Sipp *et al.* (2010).

It is important to realize that these linear analyses that have been discussed so far are strictly only valid near the threshold of instability (or bifurcation point). Even near the bifurcation point, the linear analysis predicts the initial growth of perturbations, but once these pertubations become sufficiently large, nonlinear effects start becoming important, and the flow saturates to a nonlinear limit cycle (or a nonlinear global mode). For a weakly-nonparallel flow, Pier & Huerre (2001) extended the local linear stability analysis to predict the frequency of the nonlinear global mode that develops in a spatially developing wake. They showed that the nonlinear global frequency is determined by the local absolute frequency at the streamwise location where the flow first becomes absolutely unstable. For the more strongly non-parallel case of the cylinder wake, Pier (2002) found that the

[1] This overlap is defined as the dyadic product of the direct and adjoint global mode vectors.

local frequency selection criterion was less accurate. Near the bifurcation point, a weakly nonlinear approach can also be applied to the global stability analysis (Chomaz, 2005). This involves the use of Landau equations to model the amplitude of the global mode. In this thesis, however, only a linear stability analysis near the bifurcation point is used.

In the context of swirling flows, there have been numerous studies on the invscid and viscous linear stability of parallel swirling flows. The well-known Batchelor vortex (Batchelor, 1964), which was derived as a model for the trailing line vortex downstream of a wing, has received considerable attention. This analytical profile has also been found to be a good model for swirling flows in other applications, such as those downstream of vortex breakdown states. Both temporal and spatio-temporal stability local stability analyses have been performed, and a full review of these local stability results would be quite long. A concise review, however, can be found in §1.1 of Heaton *et al.* (2009). The main point that is important for the purpose of this thesis is that increasing swirl generally tends to promote local absolute instability for non-axisymmetric perturbations. At the time when work for this thesis was begun, the only study of the global stability of a swirling flow was that of Heaton *et al.* (2009), who considered the weakly non-parallel Batchelor vortex and found modes with azimuthal wavenumbers $m = -1$ (helical) and $m = -2$ (double-helical) to be globally unstable. The sensitivity of these modes was not, however, investigated.

1.3 Scope of this work

This thesis is part of a wider effort to identify the regions that are most influential in causing hydrodynamic instabilities in flows with strong density and velocity gradients, such as fuel injectors. It continues on from the work of Chandler (2010), who developed linearized direct and adjoint algorithms for the low Mach number Navier–Stokes equations, which are suitable to study hydrodynamic instability in flows with strong density and velocity

gradients. Chandler developed two types of adjoint algorithms: a continuous adjoint, which involved deriving the adjoint low Mach number equations, and a discrete adjoint, which involved calculating the conjugate transpose of each step of the direct algorithm. Chandler implemented these algorithms in an axisymmetric direct numerical simulation code from a previous study. Due to its convenience, only the discrete adjoint was implemented for reacting flows, whereas both the continuous and discrete adjoints were implemented for non-reacting flows. Chandler (2010) used these tools to obtain the direct and adjoint global modes for the axisymmetric mode of instability of a low-density jet and a lifted jet diffusion flame, and calculated the structural sensitivity for these flows.

In this thesis, these tools are extended to include the capability to study swirling flows and non-axisymmetric modes of instability. The continuous adjoint approach is favoured in this thesis, and therefore, a continuous adjoint scheme (which is slightly different to the scheme proposed by Chandler) has been implemented for reacting flows. In addition, the tools are extended to obtain the sensitivity of the modes of instability to steady forcing and changes in the base flow. These extensions produce a set of tools that can now be used to study a variety of both swirling and non-swirling reacting and non-reacting flows. The mathematical formulation and the numerical implementation of these tools is described in chapters 2 and 3.

These tools are then used to study a variety of flows, of increasing complexity, to build an understanding of the physical mechanisms that are responsible for global hydrodynamic instability in swirling diffusion flames. As a first step, in chapter 4, the tools are applied to study passive control of a globally unstable low-density jet. In chapters 5 and 6, the tools are applied, for the first time, to study the origin and passive control of the spiral modes of vortex breakdown. To understand the feedback mechanisms that influence the growth rate and frequency of the unstable mode, the components of the structural sensitivity tensor are considered in more detail. In chapter 5, the tools are applied to the Grabowski velocity profile (Grabowski & Berger,

1976), which is well-studied numerically. This means that the results can be compared to previous studies to establish the validity of the tools developed in this thesis. In chapter 6, the tools are applied to a velocity profile that is a good model for the velocities measured in experiments near the exit plane of swirling jets. The sensitivity maps are compared to those obtained for the Grabowski profile. In chapter 7, the lifted jet diffusion flame that was originally considered by Chandler (2010) is revisited and studied in more detail to understand the origin of, and the possible control of the unstable modes. Finally, in chapter 8, the tools are applied to study global hydrodynamic instability in a swirling flame. The modes of instability are compared to and found to be related to the modes of instability seen in the previous chapters. This thesis ends with a summary of the work completed and some possibilities of how this work may be continued and extended.

2

Mathematical formulation

This chapter is devoted to formulating the linear global stability and sensitivity analyses based on the low Mach number equations. The equations governing the motion of the base flow and those governing the motion of perturbations on top of this base flow are presented. The adjoint of the linearized operator is used to obtain the sensitivity of the growth rate and frequency of these perturbations to feedback inherent to the flow, and to open-loop steady and unsteady forcing.

2.1 Governing equations

This thesis considers the motion of a viscous fluid in a cylindrical domain with length X_{max} and radius R_{max}, using cylindrical coordinates (x, r, θ). The flow has density, ρ, pressure, p, temperature, T, and velocity, $\mathbf{u} = (u_x, u_r, u_\theta)^T$. The physical properties of the flow, namely the viscosity, μ, thermal conductivity, λ, and the specific heat capacity at constant pressure, c_p are all assumed to be uniform throughout the flow and to remain constant. The inlet boundary, at $x = 0$, is labelled Ω_{in}. The outlet boundary, at $x = X_{max}$, is labelled Ω_{out}. The lateral boundary, at $r = R_{max}$, is labelled Ω_{lat}.

The motion of the fluid is governed by a set of equations which describe the conservation of mass (the continuity equation), conservation of momen-

tum (the Navier–Stokes equations), and conservation of energy and any other scalar quantity. An additional equation of state is required to make this a complete set of equations. In nondimensional form, these equations may be written as

$$\frac{\partial \rho}{\partial t} + \mathbf{u} \cdot \nabla \rho = -\rho \nabla \cdot \mathbf{u}, \tag{2.1a}$$

$$\frac{\partial (\rho \mathbf{u})}{\partial t} = -\frac{1}{\gamma Ma^2} \nabla p + \nabla \cdot \left(\frac{1}{S_1 Re} \tau - \rho \mathbf{u}\mathbf{u} \right) + Ri(1-\rho)\hat{\mathbf{g}} \tag{2.1b}$$

$$\rho \left(\frac{\partial T}{\partial t} + \mathbf{u} \cdot \nabla T \right) = \frac{1}{S_1 RePr} \nabla^2 T, \tag{2.1c}$$

$$p = \rho \left((S_1 - 1)T + 1 \right), \tag{2.1d}$$

where $\tau = \left[\nabla \mathbf{u} + (\nabla \mathbf{u})^T \right] - \frac{2}{3} (\nabla \cdot \mathbf{u}) I$ is the viscous stress tensor. The nondimensional parameters and variables are defined in Tables 2.1 and 2.2 in terms of a reference length L_0, a reference velocity U_0, and two reference values of the density and temperature: ρ_0 and T_0 and ρ_1 and T_1. The values of these depend on the specific flow profile being studied. There are many possible ways of nondimensionalizing the equations of motion. The definitions used in this thesis follow those used in earlier studies of Nichols (2005) and Chandler (2010). The same results can be obtained with different definitions, as long as the parameters are scaled appropriately.

In the limit of low Mach number, an approximate set of equations can be derived which allows for density variations due to temperature or due to the mixing of different species but excludes density variations due to pressure. This has the effect of excluding acoustic waves, which significantly reduces the computational cost of solving these equations.

To derive these low Mach number (LMN) equations, the independent variables in the equations above are expanded as power series in $\epsilon = \gamma Ma^2$ in the form $u = u^{(0)} + \epsilon u^{(1)} + O(\epsilon^2)$. The pressure term in the momentum equation contains a factor of $1/\epsilon$ and hence, the term retained in the momentum equation is the first-order term $-\nabla p^{(1)}$. The zeroth order mo-

Nondimensional variable	Definition
Length	$x \equiv \frac{x^*}{L_0}$
Velocity	$\mathbf{u} \equiv \frac{\mathbf{u}^*}{U_0}$
Temperature	$T \equiv \frac{T^* - T_0}{T_1 - T_0}$
Pressure, p	$p \equiv \frac{p^*}{\rho_0 R_g T_0}$
Density	$\rho \equiv \frac{\rho^*}{\rho_0}$
Time	$t \equiv \frac{t^* U_0}{L_0}$

Table 2.1: Nondimensional variables defined in terms of dimensional variables (starred), physical constants and the reference values.

Nondimensional parameter	Definition
Mach number	$Ma \equiv \frac{U_0}{\gamma R_g T_0}$
Density ratio	$S_1 \equiv \frac{\rho_0}{\rho_1}$
Reynolds number	$Re \equiv \frac{\rho_1 U_0 L_0}{\mu}$
Prandtl number	$Pr \equiv \frac{\mu c_p}{\lambda}$
Richardson number	$Ri \equiv \frac{g L_0}{U_0^2}$

Table 2.2: Nondimensional parameters defined in terms of dimensional variables (starred), physical constants and the reference values.

mentum equation gives $\nabla p^{(0)} = 0$ and the zeroth order equation of state gives $p^{(0)} = \rho\,[(S_1 - 1)T + 1]$. All other variables are approximated by the zeroth order term in their series.

This implies that the zeroth order pressure (which is referred to as the thermodynamic pressure), is uniform in space. In this thesis, the computational domain is assumed to be open, which implies that the thermodynamic pressure is also constant in time. Using the equation of state and the definition of the nondimensional pressure, it can be shown that $p^{(0)} = 1$. In the LMN equations, the first order pressure $p^{(1)}$ is referred to as the hydrodynamic pressure because it is associated with the fluid motion and does not affect the thermodynamic state of the fluid. In nondimensional form, the LMN equations are

$$\frac{\partial \rho}{\partial t} + \mathbf{u} \cdot \nabla \rho = -\rho \nabla \cdot \mathbf{u}, \tag{2.2a}$$

$$\frac{\partial (\rho \mathbf{u})}{\partial t} = -\nabla p + \nabla \cdot (\frac{1}{S_1 Re}\tau - \rho \mathbf{u}\mathbf{u}) + Ri(1-\rho)\hat{\mathbf{g}}, \tag{2.2b}$$

$$\rho(\frac{\partial T}{\partial t} + \mathbf{u} \cdot \nabla T) = \frac{1}{S_1 RePr}\nabla^2 T, \tag{2.2c}$$

$$\rho\,[(S_1 - 1)T + 1] = 1, \tag{2.2d}$$

where the superscript has been dropped from the hydrodynamic pressure. These equations can be expressed in terms of the momentum, $\mathbf{m} = \rho\mathbf{u}$, temperature and pressure as

$$\frac{\partial \mathbf{q}}{\partial t} = \mathcal{N}(\mathbf{q}), \tag{2.3}$$

where $\mathbf{q} \equiv (m_x,\, m_r,\, m_\theta,\, T)^T$ is the state vector and $\mathcal{N}$ is a nonlinear differential operator representing the action of the equations on the state vector. The density, ρ, is not included in the state vector because it can be derived from the temperature, T. The pressure, p, is not included in the state vector because it can be derived from the other flow variables in this incompressible formulation.

2.2 Linear global stability analysis

In this thesis, the stability of axisymmetric flows is studied. A steady axisymmetric solution to equation (2.3) is required. This steady solution, labelled $\bar{\mathbf{q}} \equiv \left(\bar{m}_x,\, \bar{m}_r,\, \bar{m}_\theta,\, \bar{T}\right)^T$, is referred to as the *base flow* and is obtained using the procedures described in §3.2.1. [1] The evolution of small perturbations, which are labelled $\mathbf{u}', \rho'$ *etc.*, on top of the base flow is governed by the linearized equations of motion:

$$\frac{\partial \rho'}{\partial t} = -\nabla \cdot \mathbf{m}', \tag{2.4a}$$

$$\frac{\partial \mathbf{m}'}{\partial t} = -\nabla p' - \nabla \cdot (\bar{\rho}\bar{\mathbf{u}}\mathbf{u}' + \bar{\rho}\mathbf{u}'\bar{\mathbf{u}} + \rho'\bar{\mathbf{u}}\bar{\mathbf{u}}) + \frac{1}{S_1 Re}\nabla \cdot \tau' + Ri\rho'\hat{\mathbf{g}}, \tag{2.4b}$$

$$\bar{\rho}\frac{\partial T'}{\partial t} = -\mathbf{m}' \cdot \nabla \bar{T} - \bar{\rho}\bar{\mathbf{u}} \cdot \nabla T' + \frac{1}{S_1 RePr}\nabla^2 T', \tag{2.4c}$$

$$\frac{\rho'}{\bar{\rho}} = -\frac{(S_1 - 1)T'}{((S_1 - 1)\bar{T} + 1}, \tag{2.4d}$$

where $\mathbf{m}' \equiv \bar{\rho}\mathbf{u}' + \rho'\bar{\mathbf{u}}$ is the linearized momentum and $\tau' = \left[\nabla \mathbf{u}' + (\nabla \mathbf{u}')^T\right] - \frac{2}{3}(\nabla \cdot \mathbf{u}')I$ is the linearized viscous stress tensor. This set of equations can be represented as

$$\frac{\partial \mathbf{q}'}{\partial t} = \mathbf{L}\mathbf{q}', \tag{2.5}$$

where $\mathbf{q}' \equiv (m_x',\, m_r',\, m_\theta',\, T')^T$ is the state vector and $\mathbf{L}$ is a linear differential operator representing the action of the equations on the state vector.

Following the normal mode approach, these linear perturbations are decomposed into Fourier modes in time and the azimuthal direction:

$$\mathbf{q}'(x, r, \theta, t) = \hat{\mathbf{q}}(x, r)e^{\dot{\imath}m\theta + \lambda t}, \tag{2.6}$$

[1] The steady base flow is a solution to the nonlinear LMN Navier–Stokes equations, but it may be unstable, in which case the steady base flow will not exist in practice.

where m is the azimuthal wavenumber and $\lambda \equiv \sigma + \mathrm{i}\omega$ contains the growth rate, σ, and frequency, ω. Substituting (2.6) into (2.5) leads to an eigenvalue problem, in which m has been incorporated into the linear operator as a parameter:

$$\lambda \hat{\mathbf{q}} = \mathbf{L}_m \hat{\mathbf{q}}. \tag{2.7}$$

For each azimuthal wavenumber, m, only certain values of λ satisfy (2.7). Each of these eigenvalues has a corresponding two-dimensional eigenfunction, $\hat{\mathbf{q}}(x, r)$. Each eigenvalue/eigenfunction pair is labelled a *direct global mode*. The linear stability of each direct global mode is determined by its growth rate, σ. If $\sigma < 0$ it is linearly globally stable. If $\sigma > 0$, it is linearly globally unstable. In this linear analysis, the flow tends to the form of the global mode with highest σ in the long-time limit and therefore this mode determines the system's overall stability.

2.3 Sensitivity to internal feedback

As mentioned earlier, global instability arises due to purely hydrodynamic feedback mechanisms in the flow. Mathematically, these feedback mechanisms are inherent to the linearized operator $\mathbf{L}_m$. As a simple thought exercise, one may consider the effect of changing these feedback mechanisms to control the global instability. The eigenvalue of the global mode is a function of the linear operator and the base flow, $\lambda = f\left(\mathbf{L}_m, \bar{\mathbf{q}}\right)$. For a simple function $G = f(x, y)$, the change in G due to small change in x is given by $\delta G = \frac{\partial G}{\partial x}\delta x$. Similarly, the change in the eigenvalue due to a small change in the linear operator is given by

$$\delta\lambda = \langle \nabla_{\mathbf{L}_m}\lambda, \delta\mathbf{L}_m \rangle, \tag{2.8}$$

where $\nabla_{\mathbf{L}_m}\lambda$ is a complex function that represents the functional derivative of λ with respect to $\mathbf{L}_m$. Formally, this is defined as

$$\nabla_{\mathbf{L}_m}\lambda = \lim_{\epsilon \to 0}\left(\frac{\lambda(\mathbf{L}_m + \epsilon\delta\mathbf{L}_m, \bar{\mathbf{q}}) - \lambda(\mathbf{L}_m, \bar{\mathbf{q}})}{\epsilon}\right). \tag{2.9}$$

This is labelled the sensitivity of the eigenvalue to a small change in the linear operator or, in short, the *structural sensitivity*. The notation $\langle \mathbf{a}, \mathbf{b} \rangle$ denotes an inner product over a volume V,

$$\langle \mathbf{a}, \mathbf{b} \rangle = \frac{1}{V} \int_V \mathbf{a}^H \mathbf{b} \, dV, \tag{2.10}$$

where $\mathbf{a}^H$ denotes the Hermitian (*i.e.* complex conjugate transpose) of $\mathbf{a}$.

2.3.1 Derivation

Using ideas from optimal control theory, the sensitivity function can be calculated by formulating a Lagrangian problem for λ. Equation (2.7) acts as a constraint in this problem. For now, changes in the base flow are neglected and only changes in the linear operator are considered. The Lagrangian problem is then given by

$$\mathcal{L} = \lambda - \langle \mathbf{a}, \lambda \hat{\mathbf{q}} - \mathbf{L}_m \hat{\mathbf{q}} \rangle \tag{2.11}$$

The complex vector field $\mathbf{a}$ is the Lagrange multiplier in this problem. To find the sensitivity function, the functional derivative of $\mathcal{L}$ with respect to all variables other than $\mathbf{L}_m$ must be set to zero. The sensitivity function will then be given by the the functional derivative of $\mathcal{L}$ w.r.t $\mathbf{L}_m$. Firstly, setting the functional derivative of $\mathcal{L}$ w.r.t $\hat{\mathbf{q}}$ to zero gives

$$\langle \nabla_{\hat{\mathbf{q}}} \mathcal{L}, \delta\hat{\mathbf{q}} \rangle = \lim_{\epsilon \to 0} \left(\frac{-\langle \mathbf{a}, \epsilon(\lambda \delta\hat{\mathbf{q}} - \mathbf{L}_m \delta\hat{\mathbf{q}}) \rangle}{\epsilon} \right) = 0 \tag{2.12a}$$

$$\Rightarrow -\langle \mathbf{a}, \lambda \delta\hat{\mathbf{q}} \rangle + \langle \mathbf{a}, \mathbf{L}_m \delta\hat{\mathbf{q}} \rangle = 0. \tag{2.12b}$$

Using results from the field of functional analysis, the second term can be rearranged to give

$$\langle \mathbf{a}, \mathbf{L}_m \delta\hat{\mathbf{q}} \rangle = \langle \mathbf{L}_m^+ \mathbf{a}, \delta\hat{\mathbf{q}} \rangle + \text{boundary terms}, \tag{2.13}$$

where $\mathbf{L}_m^+$ is the corresponding adjoint operator of $\mathbf{L}_m$. The adjoint operator can be seen to be a generalization of the conjugate transpose of a matrix. The boundary terms are set to zero by choosing suitable boundary conditions (§3.3.2). Then, substituting (2.13) into (2.12) gives

$$\langle -\lambda^* \mathbf{a}, \delta\hat{\mathbf{q}} \rangle + \langle \mathbf{L}_m^+ \mathbf{a}, \delta\hat{\mathbf{q}} \rangle = 0 \tag{2.14a}$$

$$\langle -\lambda^* \mathbf{a} + \mathbf{L}_m^+ \mathbf{a}, \delta\hat{\mathbf{q}} \rangle = 0 \tag{2.14b}$$

A non-trivial solution of this is obtained by solving

$$-\lambda^* \mathbf{a} + \mathbf{L}_m^+ \mathbf{a} = 0, \tag{2.15}$$

or equivalently,

$$\lambda^* \mathbf{a} = \mathbf{L}_m^+ \mathbf{a}, \tag{2.16}$$

where $\lambda^* \equiv \sigma - \mathrm{i}\omega$ is the complex conjugate of the corresponding direct eigenvalue. This is an eigenvalue problem and by comparing it to (2.7), the Lagrange multiplier $\mathbf{a}$ can be interpreted as the adjoint eigenfunction or the *adjoint global mode* $\hat{\mathbf{q}}^+$.

There are two ways to obtain the adjoint operator. The first way is the discrete adjoint approach, which involves taking the conjugate transpose of the discretized linear operator matrix to obtain the discretized adjoint operator matrix. The second way is the continous adjoint approach, which involves deriving the adjoint equations from the linearized NS equations and then discretizing the adjoint equations. Chandler discussed both these approaches for the LMN equations and showed that they gave the same results. He found that the discrete adjoint is easier to debug than the continuous adjoint and its eigenvalue matches the direct solution to machine precision. On the other hand, the continuous adjoint offers physical insight and Chandler found that it produced better resolved eigenmodes and converged faster than the discrete adjoint for the same spatial resolution. Therefore, in this thesis, the continuous adjoint approach is used.

In the continuous adjoint approach, the adjoint equations are derived from the direct governing equations by integration by parts. For the LMN equations, Chandler (2010) found that the direct equations (2.4) need to be rearranged into a suitable form before deriving the adjoint equations. This is necessary so that the two sets of equations can be solved using a similar algorithm, which reduces numerical errors that arise when solving the adjoint equations. The Lagrangian problem (2.11) is then written as

$$
\begin{aligned}
\mathcal{L} = \lambda \quad & - \left\langle \hat{p}^{+}, (S_1 - 1)\left(\bar{m}_i \frac{\partial \hat{T}}{\partial \hat{x}_i} - \frac{1}{S_1 Re Pr}\frac{\partial^2 \hat{T}}{\partial x_i^2}\right) + \frac{\partial}{\partial x_i}\left(\frac{\hat{m}_i}{\bar{\rho}}\right)\right\rangle \cdots \\
& - \left\langle \hat{m}_i^{+}, \lambda \hat{m}_i + \frac{\partial}{\partial x_j}\left(\frac{\bar{m}_j \hat{m}_i}{\bar{\rho}} + \frac{\hat{m}_j \bar{m}_i}{\bar{\rho}} - \frac{\hat{\rho}\bar{m}_j \bar{m}_i}{\bar{\rho}^2}\right) + \frac{\partial \hat{p}}{\partial x_i} \cdots \right. \\
& - \left. \frac{1}{S_1 Re}\left(\frac{\partial^2}{\partial x_j^2}\left(\frac{\hat{m}_i}{\bar{\rho}} - \frac{\hat{\rho}\bar{m}_i}{\bar{\rho}^2}\right) + \frac{1}{3}\frac{\partial^2}{\partial x_j \partial x_i}\left(\frac{\hat{m}_i}{\bar{\rho}} - \frac{\hat{\rho}\bar{m}_i}{\bar{\rho}^2}\right)\right) - Ri\hat{\rho}\hat{\mathbf{g}}\right\rangle \cdots \\
& - \left\langle \hat{T}^{+}, \lambda \hat{T} + \frac{\bar{m}_i}{\bar{\rho}}\frac{\partial \hat{T}}{\partial x_i} + \frac{\hat{m}_i}{\bar{\rho}}\frac{\partial \bar{T}}{\partial x_i} - \frac{1}{S_1 Re Pr \bar{\rho}}\frac{\partial^2 \hat{T}}{\partial x_i^2}\right\rangle \cdots \\
& - \left\langle \hat{\rho}^{+}, \frac{\hat{\rho}}{\bar{\rho}^2} + (S_1 - 1)\hat{T}\right\rangle .
\end{aligned}
\tag{2.17}
$$

The adjoint pressure acts as the Lagrange multiplier for the continuity equation. This rearrangement is required to eliminate the $\partial\rho/\partial t$ term that was present in the continuity equation in (2.4). This term would have led to a $\partial\hat{p}^{+}/\partial t$ term in the adjoint equations, which is not present in the direct equations. From (2.17), the adjoint equations are derived by taking the functional derivative w.r.t the direct global mode fields as outlined in equations (2.12) to (2.14). The adjoint eigenvalue problem is then defined by the following

set of adjoint LMN equations:

$$\frac{\partial \hat{m}_i^+}{\partial x_i} = 0 \tag{2.18a}$$

$$\lambda^* \hat{m}_i^+ = \frac{\bar{m}_j}{\bar{\rho}}\left(\frac{\partial \hat{m}_i^+}{\partial x_j} + \frac{\partial \hat{m}_j^+}{\partial x_i}\right) + \frac{1}{\bar{\rho}}\frac{\partial \hat{p}^+}{\partial x_i} + \frac{1}{S_1 Re \bar{\rho}}\left(\frac{\partial^2 \hat{m}_i^+}{\partial x_j^2} + \frac{1}{3}\frac{\partial^2 \hat{m}_j^+}{\partial x_j \partial x_i}\right) - \frac{\hat{T}^+}{\bar{\rho}}\frac{\partial \bar{T}}{\partial x_i} \tag{2.18b}$$

$$\lambda^* \hat{T}^+ = \bar{m}_i \frac{\partial}{\partial x_i}\left(\frac{\hat{T}^+}{\bar{\rho}} + (S_1 - 1)\hat{p}^+\right) + \frac{1}{S_1 RePr}\frac{\partial^2}{\partial x_i^2}\left(\frac{\hat{T}^+}{\bar{\rho}} + (S_1 - 1)\hat{p}^+\right) - (S_1 - 1)\hat{\rho}^+ \tag{2.18c}$$

$$\hat{\rho}^+ = -\bar{m}_i \bar{m}_j \frac{\partial \hat{m}_i^+}{\partial x_j} - Ri\bar{\rho}^2 \hat{m}_i^+ g_i - \frac{\bar{m}_i}{S_1 Re}\left(\frac{\partial^2 \hat{m}_i^+}{\partial x_j^2} + \frac{1}{3}\frac{\partial^2 \hat{m}_j^+}{\partial x_j \partial x_i}\right) \tag{2.18d}$$

Returning to the Lagrangian problem, setting the functional derivative of $\mathcal{L}$ w.r.t. $\mathbf{a}$ (now relabelled $\hat{\mathbf{q}}^+$) to zero gives

$$\langle \nabla_{\hat{\mathbf{q}}^+}\mathcal{L}, \delta\hat{\mathbf{q}}^+\rangle = \lim_{\epsilon\to 0}\left(\frac{-\epsilon\langle \delta\hat{\mathbf{q}}^+, \lambda\hat{\mathbf{q}} - \mathbf{L}_m\hat{\mathbf{q}}\rangle}{\epsilon}\right) = 0 \tag{2.19a}$$

$$\Rightarrow -\langle \hat{\mathbf{q}}^+, \lambda\hat{\mathbf{q}} - \mathbf{L}_m\hat{\mathbf{q}}\rangle = 0. \tag{2.19b}$$

A non-trivial solution of this is simply the direct eigenvalue problem (2.7).

Next, setting the functional derivative of $\mathcal{L}$ w.r.t. λ to zero gives

$$\langle \nabla_\lambda\mathcal{L}, \delta\lambda\rangle = \lim_{\epsilon\to 0}\left(\frac{\epsilon\delta\lambda - \langle \hat{\mathbf{q}}^+, \epsilon\delta\lambda\hat{\mathbf{q}}\rangle}{\epsilon}\right) = 0 \tag{2.20a}$$

$$\Rightarrow \delta\lambda - \langle \hat{\mathbf{q}}^+, \hat{\mathbf{q}}\rangle\delta\lambda = 0. \tag{2.20b}$$

This provides a normalization condition for the direct and adjoint global modes:

$$\langle \hat{\mathbf{q}}^+, \hat{\mathbf{q}}\rangle = 1. \tag{2.21}$$

Finally, the functional derivative of $\mathcal{L}$ w.r.t. $\mathbf{L}_m$ is given by

$$\langle \nabla_{\mathbf{L}_m} \mathcal{L}, \delta \mathbf{L}_m \rangle = \lim_{\epsilon \to 0} \left(\frac{-\langle \hat{\mathbf{q}}^+, -\epsilon \delta \mathbf{L}_m \hat{\mathbf{q}} \rangle}{\epsilon} \right) \tag{2.22a}$$

$$= \langle \hat{\mathbf{q}}^+, \delta \mathbf{L}_m \hat{\mathbf{q}} \rangle. \tag{2.22b}$$

By setting all other functional derivatives to zero, the change in the eigenvalue due to a change in the feedback in the linear operator is given by the expression in (2.22)b. The sensitivity of the eigenvalue to internal feedback, or the structural sensitivity, is given by the dyadic product of the direct and adjoint state vectors

$$\nabla_{\mathbf{L}_m} \lambda = \hat{\mathbf{q}} (\hat{\mathbf{q}}^+)^*. \tag{2.23}$$

2.3.2 The wavemaker

The concept of the structural sensitivity was developed by Hill (1992) and Giannetti & Luchini (2007) for the incompressible Navier–Stokes equations, for which the structural sensitivity is given by the dyadic product of the direct and adjoint global mode velocity vectors, $S_{ij} = \hat{\mathbf{u}}_i (\hat{\mathbf{u}}_j^+)^*$. For two-dimensional direct and adjoint global modes, each component of the sensitivity tensor can be visualized as a two-dimensional map that shows the regions of the flow where feedback between the components of the velocity is strong. Giannetti & Luchini (2007) used the Frobenius norm of this sensitivity tensor to identify where a modification in the linearized equations produces the greatest drift of the eigenvalue and thereby reveal the region of the flow that acts as the wavemaker.

For the formulation of the LMN equations used in this thesis, the equivalent definition to that of Giannetti & Luchini (2007) is given by the dyadic product of the direct and adjoint momentum vectors, $S_{ij} = \hat{\mathbf{m}}_i (\hat{\mathbf{m}}_j^+)^*$. The components of this complex-valued 3×3 tensor show how feedback between the components of the linearized momentum vector affects the growth rate and frequency of the global mode. The Frobenius norm of this tensor is

equivalent to evaluating the expression

$$|\nabla_G \lambda|_{max} = \|(\hat{\mathbf{m}}^+)^H\| \|\hat{\mathbf{m}}^+\|, \tag{2.24}$$

where $\hat{\mathbf{m}}$ and $\hat{\mathbf{m}}^+$ represent the direct and adjoint global mode momentum fields that have been normalized according to (2.21). In this thesis, the Frobenius norm of the sensitivity tensor is used to identify the region of the flow that drives the global mode but it cannot reveal the feedback mechanisms active in this region. This additional information is obtained by analysing the individual components of the sensitivity tensor.

2.4 Sensitivity to a control force

So far, only the sensitivity of the eigenvalue to feedback between the perturbations has been considered. From an engineer's perspective, it would be useful to know the effect of external forces on the unstable mode. Depending on the application, engineers might want either to suppress the unstable mode (to delay transition, for instance) or to promote it (to increase mixing, for instance).

The effect of a small control force on the unstable eigenvalue is considered here. The control force is modelled by adding mass, momentum and energy source terms to the right-hand side of equation (2.3):

$$\frac{\partial \mathbf{q}}{\partial t} = \mathcal{N}(\mathbf{q}) + \mathbf{F}, \tag{2.25}$$

where $\mathbf{F} \equiv (\varrho, \mathbf{f}, \psi)^T$ contains the source terms added to the right-hand side of the continuity, momentum and energy equations respectively. The variables ϱ, $\mathbf{f}$ and ψ are the nondimensional rates of addition per unit volume of mass, momentum and thermal energy into the flow. In this linear stability framework, the control force has a steady component ($\bar{\mathbf{F}}$) that acts on the base flow ($\bar{\mathbf{q}}$) and an unsteady component ($\mathbf{f}'$) that acts on the linear per-

turbation ($\mathbf{q}'$) . The effects of these two components are modelled separately following the approach of Marquet *et al.* (2008*b*).

The eigenvalue of the global mode, $\lambda = \sigma + \mathrm{i}\omega$, is a function of the base flow fields ($\bar{\mathbf{q}}$) and these are, in turn, functions of the steady components of the forcing terms ($\bar{\mathbf{F}}$). The eigenvalue can, thus, be considered to be a function of the steady component of the forcing terms, $\lambda = f(\bar{\mathbf{F}})$. Similarly, the eigenvalue can also be considered to be a function of the unsteady component of the forcing terms, $\lambda = f(\mathbf{f}')$. In this linear analysis, an eigenvalue of a global mode is only sensitive to unsteady harmonic forcing at the same frequency as the natural frequency of the global mode. The unsteady forcing is assumed to take the form $\mathbf{f}' = \hat{\mathbf{f}}(x, r)e^{\mathrm{i}\omega t}$, where $\hat{\mathbf{f}}(x, r)$ represents the spatial structure of the forcing term.

Following the approach in §2.3, the sensitivity functions are calculated by formulating a Lagrangian problem for λ. Changes in the base flow are now considered in addition to changes at the perturbation level. The Lagrangian is now given by

$$\mathcal{L} = \lambda - \langle \bar{\mathbf{q}}^+, \mathcal{N}\bar{\mathbf{q}} - \bar{\mathbf{F}} \rangle - \langle \hat{\mathbf{q}}^+, \lambda\hat{\mathbf{q}} - \mathbf{L}_m\hat{\mathbf{q}} - \hat{\mathbf{f}} \rangle, \tag{2.26}$$

where the Lagrange multipliers $\bar{\mathbf{q}}^+$ and $\hat{\mathbf{q}}^+$ can be interpreted as the adjoint base flow and the adjoint global mode respectively.

2.4.1 Sensitivity to steady forcing

The change in the eigenvalue due to a small variation of the steady force is given by

$$\delta\lambda_{\bar{\mathbf{F}}} = \langle \nabla_{\bar{\mathbf{F}}}\lambda, \delta\bar{\mathbf{F}} \rangle, \tag{2.27}$$

where $\nabla_{\bar{\mathbf{F}}}\lambda$, the functional derivative of λ w.r.t $\bar{\mathbf{F}}$, is labelled the *sensitivity of the eigenvalue to steady forcing*. To find the sensitivity function, the functional derivatives of $\mathcal{L}$ with respect to all variables other than $\bar{\mathbf{F}}$ must be set

to zero. As in the previous section, the derivative w.r.t $\hat{\mathbf{q}}$ leads to a set of equations that defines the adjoint eigenvalue problem (2.16). The derivative w.r.t $\hat{\mathbf{q}}^+$ leads to a set of equations that defines the direct eigenvalue problem (2.7). The derivative w.r.t λ leads to the normalization condition for the direct and adjoint eigenmodes (2.21).

The derivative w.r.t $\bar{\mathbf{q}}$ leads to a set of equations for the adjoint base flow fields, $\bar{\mathbf{L}}^+\bar{\mathbf{q}}^+ = \bar{\mathbf{g}}^+$. For incompressible flow, the adjoint base flow operator $\bar{\mathbf{L}}^+$ is equivalent to the adjoint global mode operator $\mathbf{L}^+$. For our formulation of the LMN equations, however, these two operators are different. The adjoint base flow equations can be written in full as

$$\frac{\partial \bar{m}_i^+}{\partial x_i} = 0, \tag{2.28a}$$

$$-\frac{\bar{m}_j}{\bar{\rho}}\left(\frac{\partial \bar{m}_i^+}{\partial x_j} - \frac{\partial \bar{m}_j^+}{\partial x_i}\right) - \frac{\partial \bar{p}^+}{\partial x_i} - \frac{1}{S_1 Re\bar{\rho}}\left(\frac{\partial^2 \bar{m}_i^+}{\partial x_j^2} + \frac{1}{3}\frac{\partial^2 \bar{m}_j^+}{\partial x_j \partial x_i}\right) + \bar{T}^+\frac{\partial \bar{T}}{\partial x_i} = \bar{f}_i^+, \tag{2.28b}$$

$$-\bar{m}_i\frac{\partial \bar{T}^+}{\partial x_i} - \frac{1}{S_1 RePr}\frac{\partial^2 \bar{T}^+}{\partial x_i^2} + (S_1 - 1)\bar{\rho}\bar{\rho}^+ = \bar{\psi}, \tag{2.28c}$$

$$\frac{\bar{m}_i\bar{m}_j}{\bar{\rho}^2}\frac{\partial \bar{m}_i^+}{\partial x_j} + \frac{\bar{m}_i}{S_1 Re\bar{\rho}^2}\left(\frac{\partial^2 \bar{m}_i^+}{\partial x_j^2} + \frac{1}{3}\frac{\partial^2 \bar{m}_j^+}{\partial x_j \partial x_i}\right) + \frac{\bar{\rho}^+}{\bar{\rho}} = \bar{\varrho}^+. \tag{2.28d}$$

The complex fields that constitute $\bar{\mathbf{g}}^+ \equiv (0, \bar{f}_i^+, \bar{\psi}^+)^T$ and $\bar{\varrho}^+$ on the RHS need to be calculated first from the base flow and the direct and adjoint

global modes as

$$\begin{aligned}
\bar{f_i}^+ &\equiv \left(\frac{\hat{m}_j^*}{\bar{\rho}} - \frac{\hat{\rho}^*\bar{m}_j}{\bar{\rho}^2}\right)\left(\frac{\partial \hat{m}_i^+}{\partial x_j} + \frac{\partial \hat{m}_j^+}{\partial x_i}\right) - \frac{\hat{\rho}^*}{S_1 Re \bar{\rho}^2}\left(\frac{\partial^2 \hat{m}_i^+}{\partial x_j^2} + \frac{1}{3}\frac{\partial^2 \hat{m}_j^+}{\partial x_j \partial x_i}\right)\cdots \\
&\cdots - \left(\frac{\hat{T}^+}{\bar{\rho}} + (S_1 - 1)\hat{p}^+\right)\frac{\partial \hat{T}^*}{\partial x_i}, \qquad (2.29a) \\
\bar{\psi}_T^+ &\equiv \frac{\partial}{\partial x_j}\left(\frac{\hat{T}^+ \hat{m}_j^*}{\bar{\rho}}\right), \qquad (2.29b) \\
\bar{\varrho}^+ &\equiv 2\frac{\hat{\rho}^*\hat{\rho}^+}{\bar{\rho}^3} - \frac{\hat{m}_j^*}{\bar{\rho}^2}\frac{\partial \hat{p}^+}{\partial x_j} + \frac{\hat{T}^+}{\bar{\rho}^2}\left(\bar{m}_j \frac{\partial \hat{T}^*}{\partial x_j} + \hat{m}_j^* \frac{\partial \bar{T}}{\partial x_j}\right)\cdots \\
&\cdots - \frac{\hat{T}^+}{S_1 Re Pr \bar{\rho}^2}\frac{\partial^2 \hat{T}^*}{\partial x_j^2} - \left(\frac{\bar{m}_i \hat{m}_j^*}{\bar{\rho}^2} + \frac{\hat{m}_i^* \bar{m}_j}{\bar{\rho}^2} - \frac{2\hat{\rho}^*\bar{m}_i\bar{m}_j}{\bar{\rho}^3}\right)\frac{\partial \hat{m}_i^+}{\partial x_j}\cdots \\
&\cdots - \frac{1}{S_1 Re}\left(\frac{\hat{m}_j^*}{\bar{\rho}^2} - \frac{\hat{\rho}^*\bar{m}_j}{\bar{\rho}^3}\right)\left(\frac{\partial^2 \hat{m}_i^+}{\partial x_j^2} + \frac{1}{3}\frac{\partial^2 \hat{m}_j^+}{\partial x_j \partial x_i}\right) \qquad (2.29c)
\end{aligned}$$

The complex fields that constitute $\bar{\mathbf{g}}^+$ describe the sensitivity of the eigenvalue to arbitrary local base flow modifications, which do not necessarily obey the NS equations. For example, $\bar{f_x}^+$ can be used to obtain the effect of increasing only the axial momentum at a certain point in the flow, while keeping the other components of the base flow momentum unchanged. This differs from the adjoint base flow field $\bar{\mathbf{m}}_x^+$, which describes the effect of applying a steady axial body force at a certain point in the flow. This axial body force produces changes in all components of the momentum, such that the NS equations are satisfied.

Once the terms in (2.29) have been calculated, the adjoint base flow equations (2.28) can be solved. Since the base flow is axisymmetric, these equations are solved for an azimuthal wavenumber $m = 0$. This ensures that the adjoint base flow is axisymmetric.

The derivative of $\mathcal{L}$ w.r.t $\bar{\mathbf{F}}$ gives

$$\delta\lambda_{\bar{\mathbf{F}}} = \langle \bar{\mathbf{q}}^+, \delta\bar{\mathbf{F}} \rangle. \qquad (2.30)$$

The sensitivity of the eigenvalue to steady forcing is therefore obtained from the relevant adjoint base flow field. For example, the sensitivity to momentum forcing is given by the adjoint baseflow momentum, $\bar{\mathbf{m}}^+(x,r)$. The real part represents the sensitivity of the growth rate, σ, while the imaginary part represents the sensitivity of the frequency, ω, to a small steady force.

2.4.2 Sensitivity to unsteady forcing

The change in the eigenvalue due to a small variation of the spatial structure of the harmonic force is given by

$$\delta\lambda_{\hat{\mathbf{f}}} = \langle \nabla_{\hat{\mathbf{f}}}\lambda, \delta\hat{\mathbf{f}} \rangle, \tag{2.31}$$

where $\nabla_{\hat{\mathbf{f}}}\lambda$ is labelled the *sensitivity of the eigenvalue to harmonic forcing.*

The derivative of $\mathcal{L}$ w.r.t $\hat{\mathbf{f}}$ gives

$$\delta\lambda_{\hat{\mathbf{f}}} = \langle \hat{\mathbf{q}}^+, \delta\hat{\mathbf{f}} \rangle. \tag{2.32}$$

The sensitivity of the eigenvalue to harmonic forcing is therefore obtained from the relevant adjoint global mode fields.

2.5 Extension to reacting flows

The formulation presented in this chapter is easily extended to consider a fuel reacting with an oxidizer to produce a flame. The reacting LMN equations presented in Nichols & Schmid (2008) are used here. These are similar to the non-reacting LMN equations described in §2.1, except for a few differences. Firstly, an additional equation is required to model the difference in composition between the fuel and oxidizer. This additional equation is similar to the non-reacting energy equation, but describes the evolution of the mixture fraction of fuel, Z, which is a scalar field with a value of $Z = 1$ for pure

fuel and $Z = 0$ for pure oxidizer. Secondly, the energy equation is modified to include a source term to model the heat release due to reaction between the fuel and oxidizer. Thirdly, the equation of state is modified to include a dependence on both temperature and composition. The nondimensional reacting LMN equations are expressed as

$$\frac{\partial \rho}{\partial t} + \nabla \cdot (\rho \mathbf{u}) = 0 \tag{2.33a}$$

$$\frac{\partial (\rho \mathbf{u})}{\partial t} = -\nabla p + \nabla \cdot (\frac{1}{S_1 Re}\tau - \rho \mathbf{u}\mathbf{u}) + Ri(1-\rho)\hat{\mathbf{g}}, \tag{2.33b}$$

$$\rho(\frac{\partial Z}{\partial t} + \mathbf{u} \cdot \nabla Z) = \frac{1}{S_1 ReSc}\nabla^2 Z, \tag{2.33c}$$

$$\rho(\frac{\partial T}{\partial t} + \mathbf{u} \cdot \nabla T) = \frac{1}{S_1 RePr}\nabla^2 T + Da\rho^3\omega, \tag{2.33d}$$

$$\rho\left[(S_1 - 1)Z + 1\right]\left[(S_2 - 1)T + 1\right] = 1, \tag{2.33e}$$

where $\tau = \left[\nabla \mathbf{u} + (\nabla \mathbf{u})^T\right] - \frac{2}{3}(\nabla \cdot \mathbf{u})I$ is the viscous stress tensor. The source term, $Da\rho^3\omega$, is equivalent to the nondimensional rate of enthalpy release per unit volume. The Damkohler number, Da, represents the ratio between the rate of production of reaction product and the rate of fluid convection. For the rate of reaction, ω, a simple Arrhenius law is used, which is identical to the one used by Nichols & Schmid (2008):

$$\omega = \left\{\left(Z - \frac{T}{s+1}\right)\left(1 - Z - \frac{sT}{s+1}\right) - \kappa T^2\right\} \exp\left[\frac{-\beta(1-T)}{1-\alpha(1-T)}\right]. \tag{2.34}$$

The chemistry of the reaction is described by the mass stoichiometric ratio, s, the equilibrium constant, κ, the heat release parameter, $\alpha \equiv (\tilde{T}_f - T_0)/\tilde{T}_f$, and the Zeldovich number $\beta \equiv \alpha\tilde{T}_a/\tilde{T}_f$, where $\tilde{T}_a$ (K) is the dimensional activation temperature of the reaction, and $\tilde{T}_f$ (K) is the dimensional adiabatic flame temperature. The additional nondimensional parameter in the equations is the temperature ratio $S_2 \equiv \tilde{T}_f/T_0$. The values of the chemical parameters depend on the fuel-oxidizer mixture being considered and can be

obtained from references such as Poinsot & Veynante (2005).

As for the non-reacting equations, a steady axisymmetric base flow is obtained and the evolution of small perturbations on top of this reacting base flow is given by the linearized reacting LMN equations:

$$\frac{\partial \rho'}{\partial t} = -\nabla \cdot \mathbf{m}', \tag{2.35a}$$

$$\frac{\partial \mathbf{m}'}{\partial t} = -\nabla p' - \nabla \cdot (\bar{\rho}\bar{\mathbf{u}}\mathbf{u}' + \bar{\rho}\mathbf{u}'\bar{\mathbf{u}} + \rho'\bar{\mathbf{u}}\bar{\mathbf{u}}) + \frac{1}{S_1 Re}\nabla \cdot \tau' + Ri\rho'\hat{\mathbf{g}}, \tag{2.35b}$$

$$\bar{\rho}\frac{\partial Z'}{\partial t} = -\mathbf{m}' \cdot \nabla \bar{Z} - \bar{\rho}\bar{\mathbf{u}} \cdot \nabla Z' + \frac{1}{S_1 ReSc}\nabla^2 Z', \tag{2.35c}$$

$$\bar{\rho}\frac{\partial T'}{\partial t} = -\mathbf{m}' \cdot \nabla \bar{T} - \bar{\rho}\bar{\mathbf{u}} \cdot \nabla T' + \frac{1}{S_1 RePr}\nabla^2 T' + Da\bar{\rho}^2\omega', \tag{2.35d}$$

$$\frac{\rho'}{\bar{\rho}^2} = -\bar{K}_1 T' - \bar{K}_2 Z', \tag{2.35e}$$

where the linearized reaction rate is $\omega' \equiv \bar{\rho}\bar{K}_Z Z' + \bar{\rho}\bar{K}_T T' + 3\rho'\bar{\omega}$, and the additional scalar fields used for ease of reference are

$$\bar{K}_1 \equiv (S_2 - 1)\left((S_1 - 1)\bar{Z} + 1\right), \tag{2.36}$$

$$\bar{K}_2 \equiv (S_1 - 1)\left((S_2 - 1)\bar{T} + 1\right), \tag{2.37}$$

$$\bar{K}_Z \equiv \left(1 - 2\bar{Z} - \frac{s-1}{s+1}\bar{T}\right)\exp\left[\frac{-\beta(1-\bar{T})}{1-\alpha(1-\bar{T})}\right], \tag{2.38}$$

$$\bar{K}_T \equiv \left\{\left[\left(\bar{Z} - \frac{\bar{T}}{s+1}\right)\left(1 - \bar{Z} - \frac{s\bar{T}}{s+1}\right) - \kappa\bar{T}^2\right]\frac{\beta}{\left(1-\alpha(1-\bar{T})\right)^2}\cdots + 2\bar{T}\left(\frac{s}{(s+1)^2} - \kappa\right) - \frac{1+(s-1)\bar{Z}}{s+1}\right\}\exp\left[\frac{-\beta(1-\bar{T})}{1-\alpha(1-\bar{T})}\right]. \tag{2.39}$$

Chandler (2010) derived a set of adjoint reacting LMN equations using the same procedure as for the non-reacting equations but only implemented and used the discrete adjoint for reacting flows. In this thesis, however, the continuous adjoint approach is used for the reacting cases. The reacting

adjoint equations derived by Chandler (2010) are given by

$$\frac{\partial \hat{m}_i^+}{\partial x_i} = 0 \tag{2.40a}$$

$$\lambda^* \hat{m}_i^+ = \frac{\bar{m}_j}{\bar{\rho}}\left(\frac{\partial \hat{m}_i^+}{\partial x_j} + \frac{\partial \hat{m}_j^+}{\partial x_i}\right) + \frac{1}{\bar{\rho}}\frac{\partial \hat{p}^+}{\partial x_i} + \frac{1}{S_1 Re \bar{\rho}}\left(\frac{\partial^2 \hat{m}_i^+}{\partial x_j^2} + \frac{1}{3}\frac{\partial^2 \hat{m}_j^+}{\partial x_j \partial x_i}\right) - \frac{\hat{T}^+}{\bar{\rho}}\frac{\partial \bar{T}}{\partial x_i} - \frac{\hat{Z}^+}{\bar{\rho}}\frac{\partial \bar{Z}}{\partial x_i} \tag{2.40b}$$

$$\lambda^* \hat{Z}^+ = \bar{m}_i \frac{\partial}{\partial x_i}\left(\frac{\hat{Z}^+}{\bar{\rho}} + \bar{K}_2 \hat{p}^+\right) + \frac{1}{S_1 ReSc}\frac{\partial^2}{\partial x_i^2}\left(\frac{\hat{Z}^+}{\bar{\rho}} + \bar{K}_2 \hat{p}^+\right) + Da\bar{\rho}^3\left(\frac{\hat{T}^+}{\bar{\rho}} + \bar{K}_1 \hat{p}^+\right)\bar{K}_Z - \bar{K}_2 \hat{\rho}^+ \tag{2.40c}$$

$$\lambda^* \hat{T}^+ = \bar{m}_i \frac{\partial}{\partial x_i}\left(\frac{\hat{T}^+}{\bar{\rho}} + \bar{K}_1 \hat{p}^+\right) + \frac{1}{S_1 RePr}\frac{\partial^2}{\partial x_i^2}\left(\frac{\hat{T}^+}{\bar{\rho}} + \bar{K}_1 \hat{p}^+\right) + Da\bar{\rho}^3\left(\frac{\hat{T}^+}{\bar{\rho}} + \bar{K}_1 \hat{p}^+\right)\bar{K}_T - \bar{K}_1 \hat{\rho}^+ \tag{2.40d}$$

$$\hat{\rho}^+ = -\bar{m}_i \bar{m}_j \frac{\partial \hat{m}_i^+}{\partial x_j} - Ri\bar{\rho}^2 \hat{m}_i^+ g_i - \frac{\bar{m}_i}{S_1 Re}\left(\frac{\partial^2 \hat{m}_i^+}{\partial x_j^2} + \frac{1}{3}\frac{\partial^2 \hat{m}_j^+}{\partial x_j \partial x_i}\right) - 3Da\bar{\rho}^4 \bar{\omega}\left(\frac{\hat{T}^+}{\bar{\rho}} + \bar{K}_1 \hat{p}^+\right) \tag{2.40e}$$

These equations were coded but the scheme was found to be numerically unstable due to the presence of reacting terms in the definition of the adjoint density - the last term in (2.40e). Any small error in the calculation of the adjoint density was being magnified by multiplication with the Damkohler number, which was typically $O(10^6)$. This numerical instability can be avoided by using equation (2.35e) to express the ρ' term in the linearized reaction rate, ω', in (2.35d), in terms of T' and Z'. This leads to the

following set of adjoint reacting LMN equations:

$$\frac{\partial \hat{m}_i^+}{\partial x_i} = 0 \tag{2.41a}$$

$$\lambda^* \hat{m}_i^+ = \frac{\bar{m}_j}{\bar{\rho}}\left(\frac{\partial \hat{m}_i^+}{\partial x_j} + \frac{\partial \hat{m}_j^+}{\partial x_i}\right) + \frac{1}{\bar{\rho}}\frac{\partial \hat{p}^+}{\partial x_i} + \frac{1}{S_1 Re \bar{\rho}}\left(\frac{\partial^2 \hat{m}_i^+}{\partial x_j^2} + \frac{1}{3}\frac{\partial^2 \hat{m}_j^+}{\partial x_j \partial x_i}\right) - \frac{\hat{T}^+}{\bar{\rho}}\frac{\partial \bar{T}}{\partial x_i} - \frac{\hat{Z}^+}{\bar{\rho}}\frac{\partial \bar{Z}}{\partial x_i} \tag{2.41b}$$

$$\lambda^* \hat{Z}^+ = \bar{m}_i \frac{\partial}{\partial x_i}\left(\frac{\hat{Z}^+}{\bar{\rho}} + \bar{K}_2 \hat{p}^+\right) + \frac{1}{S_1 ReSc}\frac{\partial^2}{\partial x_i^2}\left(\frac{\hat{Z}^+}{\bar{\rho}} + \bar{K}_2 \hat{p}^+\right) + Da\bar{\rho}^3\left(\frac{\hat{T}^+}{\bar{\rho}} + \bar{K}_1 \hat{p}^+\right)\left(\bar{K}_Z - 3\bar{K}_2 \bar{\rho}\bar{\omega}\right) - \bar{K}_2 \hat{p}^+ \tag{2.41c}$$

$$\lambda^* \hat{T}^+ = \bar{m}_i \frac{\partial}{\partial x_i}\left(\frac{\hat{T}^+}{\bar{\rho}} + \bar{K}_1 \hat{p}^+\right) + \frac{1}{S_1 RePr}\frac{\partial^2}{\partial x_i^2}\left(\frac{\hat{T}^+}{\bar{\rho}} + \bar{K}_1 \hat{p}^+\right) + Da\bar{\rho}^3\left(\frac{\hat{T}^+}{\bar{\rho}} + \bar{K}_1 \hat{p}^+\right)\left(\bar{K}_T - 3\bar{K}_1 \bar{\rho}\bar{\omega}\right) - \bar{K}_1 \hat{p}^+ \tag{2.41d}$$

$$\hat{\rho}^+ = -\bar{m}_i \bar{m}_j \frac{\partial \hat{m}_i^+}{\partial x_j} - Ri\bar{\rho}^2 \hat{m}_i^+ g_i - \frac{\bar{m}_i}{S_1 Re}\left(\frac{\partial^2 \hat{m}_i^+}{\partial x_j^2} + \frac{1}{3}\frac{\partial^2 \hat{m}_j^+}{\partial x_j \partial x_i}\right) \tag{2.41e}$$

The sensitivity analysis for the reacting equations follows in exactly the same manner as for the non-reacting equations. The structural sensitivity is defined in the same way by equation (2.23). The hydrodynamic wavemaker may once again be identified by taking the Frobenius norm of the sensitivity tensor as defined by equation (2.24). However, for variable-density and reacting flows, the role of feedback involving the mixture fraction and temperature is likely to be important. The components of the sensitivity tensor defined in terms of the full state vector, instead of just the momentum vector, may provide additional information about the underlying feedback mechanisms responsible for causing the global instability. The relative magnitudes of the components involving momentum, temperature and mixture fraction can be compared to each other - this comparison is valid as long as the direct and adjoint global modes have been normalized according to equation (2.21).

The sensitivity to steady forcing is obtained from the adjoint base flow, which is defined by the equations

$$\frac{\partial \bar{m}_i^+}{\partial x_i} = 0 \tag{2.42a}$$

$$-\frac{\bar{m}_j}{\bar{\rho}}\left(\frac{\partial \bar{m}_i^+}{\partial x_j} - \frac{\partial \bar{m}_j^+}{\partial x_i}\right) - \frac{\partial \bar{p}^+}{\partial x_i} - \frac{1}{S_1 Re\bar{\rho}}\left(\frac{\partial^2 \bar{m}_i^+}{\partial x_j^2} + \frac{1}{3}\frac{\partial^2 \bar{m}_j^+}{\partial x_j \partial x_i}\right) + \bar{T}^+\frac{\partial \bar{T}}{\partial x_i} + \bar{Z}^+\frac{\partial \bar{Z}}{\partial x_i} = \bar{f}_i^+ \tag{2.42b}$$

$$-\bar{m}_i\frac{\partial \bar{Z}^+}{\partial x_i} - \frac{1}{S_1 ReSc}\frac{\partial^2 \bar{Z}^+}{\partial x_i^2} - Da\bar{\rho}^3\bar{T}^+\left(\bar{K}_Z - 3\bar{K}_2\bar{\rho}\bar{\omega}\right) + \bar{K}_2\bar{\rho}\bar{\rho}^+ = \bar{\psi}_Z \tag{2.42c}$$

$$-\bar{m}_i\frac{\partial \bar{T}^+}{\partial x_i} - \frac{1}{S_1 RePr}\frac{\partial^2 \bar{T}^+}{\partial x_i^2} - Da\bar{\rho}^3\bar{T}^+\left(\bar{K}_T - 3\bar{K}_1\bar{\rho}\bar{\omega}\right) + \bar{K}_1\bar{\rho}\bar{\rho}^+ = \bar{\psi}_T \tag{2.42d}$$

$$\frac{\bar{m}_i\bar{m}_j}{\bar{\rho}^2}\frac{\partial \bar{m}_i^+}{\partial x_j} + \frac{\bar{m}_i}{S_1 Re\bar{\rho}^2}\left(\frac{\partial^2 \bar{m}_i^+}{\partial x_j^2} + \frac{1}{3}\frac{\partial^2 \bar{m}_j^+}{\partial x_j \partial x_i}\right) + \frac{\bar{\rho}^+}{\bar{\rho}} = \bar{\varrho}^+. \tag{2.42e}$$

The complex fields that constitute $\bar{\mathbf{g}}^+ \equiv (0, \bar{f}_i^+, \bar{\psi}_Z^+, \bar{\psi}_T^+)^T$ and $\bar{\varrho}^+$ represent the sensitivity of the eigenvalue to local base flow modifications and are given

by

$$\bar{f}_i{}^+ \equiv \left(\frac{\hat{m}_j^*}{\bar{\rho}} - \frac{\hat{\rho}^*\bar{m}_j}{\bar{\rho}^2}\right)\left(\frac{\partial \hat{m}_i^+}{\partial x_j} + \frac{\partial \hat{m}_j^+}{\partial x_i}\right) - \frac{\hat{\rho}^*}{S_1 Re\bar{\rho}^2}\left(\frac{\partial^2 \hat{m}_i^+}{\partial x_j^2} + \frac{1}{3}\frac{\partial^2 \hat{m}_j^+}{\partial x_j \partial x_i}\right)$$
$$\cdots - \left(\frac{\hat{T}^+}{\bar{\rho}} + \bar{K}_1\hat{p}^+\right)\frac{\partial \hat{T}^*}{\partial x_i} - \left(\frac{\hat{Z}^+}{\bar{\rho}} + \bar{K}_2\hat{p}^+\right)\frac{\partial \hat{Z}^*}{\partial x_i}, \tag{2.43a}$$

$$\bar{\psi}_Z^+ \equiv \frac{\partial}{\partial x_j}\left(\frac{\hat{Z}^+\hat{m}_j^*}{\bar{\rho}}\right) - (S_2-1)(S_1-1)\hat{p}^+\left(\bar{m}_j\frac{\partial \hat{T}^*}{\partial x_j} - \frac{1}{S_1 RePr}\frac{\partial^2 \hat{T}^*}{\partial x_j^2}\right)$$
$$\cdots - (S_2-1)(S_1-1)\hat{\rho}^+\hat{T}^*$$
$$+Da\bar{\rho}^2\hat{p}^+\Big[\bar{\rho}\left(\bar{K}_1\delta\bar{K}_{Z,\delta Z} + (S_2-1)(S_1-1)\bar{K}_Z\right)\hat{Z}^*$$
$$+\bar{\rho}\left(\bar{K}_1\delta\bar{K}_{T,\delta Z} + (S_2-1)(S_1-1)\bar{K}_T\right)\hat{T}^*$$
$$-3\bar{\rho}^2\Big(\left(\bar{K}_1^2\bar{K}_Z + 2(S_2-1)(S_1-1)\bar{K}_1\bar{\omega}\right)\hat{T}^*$$
$$+\left(\bar{K}_1\bar{K}_2\bar{K}_Z + (S_2-1)(S_1-1)\bar{K}_2\bar{\omega}\right)\hat{Z}^*\Big)\Big]$$
$$+Da\bar{\rho}^2\left(\delta\bar{K}_{Z,\delta Z}\hat{Z}^* + \delta\bar{K}_{T,\delta Z}\hat{T}^*\right)\hat{T}^+$$
$$-3Da\bar{\rho}^3\hat{T}^+\left(\left(\bar{K}_1\bar{K}_Z + (S_2-1)(S_1-1)\bar{\omega}\right)\hat{T}^* + \bar{K}_2\bar{K}_Z\hat{Z}^*\right), \tag{2.43b}$$

$$\bar{\psi}_T^+ \equiv \frac{\partial}{\partial x_j}\left(\frac{\hat{T}^+\hat{m}_j^*}{\bar{\rho}}\right) - (S_2-1)(S_1-1)\hat{p}^+\left(\bar{m}_j\frac{\partial \hat{Z}^*}{\partial x_j} - \frac{1}{S_1 ReSc}\frac{\partial^2 \hat{Z}^*}{\partial x_j^2}\right)$$
$$\cdots - (S_2-1)(S_1-1)\hat{\rho}^+\hat{Z}^*$$
$$+Da\bar{\rho}^2\hat{p}^+\Big[\bar{\rho}\bar{K}_1\delta\bar{K}_{Z,\delta T}\hat{Z}^* + \bar{\rho}\bar{K}_1\delta\bar{K}_{T,\delta T}\hat{T}^*$$
$$-3\bar{\rho}^2\Big(\bar{K}_1^2\bar{K}_T\hat{T}^*$$
$$+\left(\bar{K}_1\bar{K}_2\bar{K}_T + (S_2-1)(S_1-1)\bar{K}_1\bar{\omega}\right)\hat{Z}^*\Big)\Big]$$
$$+Da\bar{\rho}^2\left(\delta\bar{K}_{Z,\delta T}\hat{Z}^* + \delta\bar{K}_{T,\delta T}\hat{T}^*\right)\hat{T}^+$$
$$-3Da\bar{\rho}^3\hat{T}^+\left(\left(\bar{K}_2\bar{K}_T + (S_2-1)(S_1-1)\bar{\omega}\right)\hat{Z}^* + \bar{K}_1\bar{K}_T\hat{T}^*\right), \tag{2.43c}$$

and

$$\begin{aligned}
\bar{\varrho}^{+} \quad \equiv \quad & 2\frac{\hat{\rho}^{*}\hat{\rho}^{+}}{\bar{\rho}^{3}} - \frac{\hat{m}_{j}^{*}}{\bar{\rho}^{2}}\frac{\partial\hat{p}^{+}}{\partial x_{j}} \\
\cdots \quad & + \frac{\hat{T}^{+}}{\bar{\rho}^{2}}\left(\bar{m}_{j}\frac{\partial\hat{T}^{*}}{\partial x_{j}} + \hat{m}_{j}^{*}\frac{\partial\bar{T}}{\partial x_{j}}\right) + \frac{\hat{Z}^{+}}{\bar{\rho}^{2}}\left(\bar{m}_{j}\frac{\partial\hat{Z}^{*}}{\partial x_{j}} + \hat{m}_{j}^{*}\frac{\partial\bar{Z}}{\partial x_{j}}\right) \\
\cdots \quad & - \frac{\hat{T}^{+}}{S_{1}RePr\bar{\rho}^{2}}\frac{\partial^{2}\hat{T}^{*}}{\partial x_{j}^{2}} - \frac{\hat{Z}^{+}}{S_{1}RePr\bar{\rho}^{2}}\frac{\partial^{2}\hat{Z}^{*}}{\partial x_{j}^{2}} \\
\cdots \quad & - \left(\frac{\bar{m}_{i}\hat{m}_{j}^{*}}{\bar{\rho}^{2}} + \frac{\hat{m}_{i}^{*}\bar{m}_{j}}{\bar{\rho}^{2}} - \frac{2\hat{\rho}^{*}\bar{m}_{i}\bar{m}_{j}}{\bar{\rho}^{3}}\right)\frac{\partial\hat{m}_{i}^{+}}{\partial x_{j}} \\
\cdots \quad & - \frac{1}{S_{1}Re}\left(\frac{\hat{m}_{j}^{*}}{\bar{\rho}^{2}} - \frac{\hat{\rho}^{*}\bar{m}_{j}}{\bar{\rho}^{3}}\right)\left(\frac{\partial^{2}\hat{m}_{i}^{+}}{\partial x_{j}^{2}} + \frac{1}{3}\frac{\partial^{2}\hat{m}_{j}^{+}}{\partial x_{j}\partial x_{i}}\right) \\
\cdots \quad & + 3Da\bar{\rho}^{2}\bar{K}_{1}\hat{p}^{+}(\bar{K}_{Z}\hat{Z}^{*} + \bar{K}_{T}\hat{T}^{*}) + 2Da\bar{\rho}\hat{T}^{+}(\bar{K}_{Z}\hat{Z}^{*} + \bar{K}_{T}\hat{T}^{*}) \\
\cdots \quad & - 12Da\bar{\rho}^{3}\bar{\omega}\bar{K}_{1}\hat{p}^{+}(\bar{K}_{1}\hat{T}^{*} + \bar{K}_{2}\hat{Z}^{*}) - 9Da\bar{\rho}^{2}\bar{\omega}\hat{T}^{+}(\bar{K}_{1}\hat{T}^{*} + \bar{K}_{2}\hat{Z}^{*}).
\end{aligned} \tag{2.44}$$

The additional scalar fields introduced by linearizing the expressions in (2.38) and (2.39) around $\bar{Z}$ and $\bar{T}$ are given by

$$\delta\bar{K}_{Z,\delta Z} \equiv -2\exp\left[\frac{-\beta(1-\bar{T})}{1-\alpha(1-\bar{T})}\right], \tag{2.45}$$

$$\begin{aligned}
\delta\bar{K}_{Z,\delta T} = \delta\bar{K}_{T,\delta Z} \equiv & \left[\left(1 - 2\bar{Z} - \frac{s-1}{s+1}\bar{T}\right)\frac{\beta}{\left(1-\alpha(1-\bar{T})\right)^{2}}\cdots\right. \\
& \left. - \frac{s-1}{s+1}\right]\exp\left[\frac{-\beta(1-\bar{T})}{1-\alpha(1-\bar{T})}\right],
\end{aligned} \tag{2.46}$$

and

$$\begin{aligned}\delta\bar{K}_{T,\delta T} \equiv \Bigg\{ \Bigg[\Bigg(-\frac{1}{s+1}\left(1-\bar{Z}-\frac{s\bar{T}}{s+1}\right) - \frac{s}{s+1}\left(\bar{Z}-\frac{\bar{T}}{s+1}\right) - 2\kappa\bar{T}\Bigg)\cdots \\ -\frac{2\alpha}{1-\alpha(1-\bar{T})}\left(\left(\bar{Z}-\frac{\bar{T}}{s+1}\right)\left(1-\bar{Z}-\frac{s\bar{T}}{s+1}\right)-\kappa\bar{T}^2\right)\cdots \\ +\frac{\beta}{\left(1-\alpha(1-\bar{T})\right)^2}\left(\left(\bar{Z}-\frac{\bar{T}}{s+1}\right)\left(1-\bar{Z}-\frac{s\bar{T}}{s+1}\right)-\kappa\bar{T}^2\right)\cdots \\ +\left(2\bar{T}\left(\frac{s}{(s+1)^2}-\kappa\right)-\frac{1+(s-1)\bar{Z}}{s+1}\right)\Bigg]\frac{\beta}{\left(1-\alpha(1-\bar{T})\right)^2}\cdots \\ +2\left(\frac{s}{(s+1)^2}-\kappa\right)\Bigg\}\exp\left[\frac{-\beta(1-\bar{T})}{1-\alpha(1-\bar{T})}\right]. \end{aligned} \tag{2.47}$$

This section has shown that a sensitivity analysis using the reacting LMN equation is similar to that using the non-reacting LMN equations, with the exception that additional terms appear that model the effect of heat release from the chemical reaction on the eigenvalue. As mentioned by Chandler (2010), it is important to note that the exponential in the nonlinear reaction rate term, ω, makes the linearized reaction rate term very sensitive to $\bar{T}$.

2.6 Local stability analysis

The local stability analysis is performed using the fully compressible Navier–Stokes equations. As for the global analysis, the velocity, density, and pressure fields are decomposed into a steady base flow and a small perturbation. The compressible Navier–Stokes equations for the perturbation are expressed as five PDEs in five primitive variables, $(\rho', u'_x, u'_r, u'_\theta, p')$. For the local analysis, the flow is assumed to exhibit two well-separated length scales: an instability wavelength, λ_l, and a length scale that characterizes the streamwise non-uniformity of the base flow, L_l. The local streamwise dependence of the global mode is then assumed to take the form $\exp(\mathrm{i}kx)$ such that (2.6) becomes

$$\mathbf{q}_l(x,r,\theta,t) = \tilde{\mathbf{q}}(r)e^{\mathrm{i}(kx+m\theta-\omega t)}, \tag{2.48}$$

where $\mathbf{q}_l \equiv (\rho', u_x', u_r', u_\theta', p')^T$ is the local state vector, $\omega = \mathrm{i}\lambda$ is the local angular frequency and k is the local wavenumber. Substituting (2.48) into the compressible Navier–Stokes equations converts the five PDEs into five ODEs, as defined in the Appendix of Lesshafft (2007). For the variable-density flows considered in this thesis, the Mach number is set to a nominal value of 0.01. For the uniform-density flows considered in this thesis, the Mach number, density perturbations, ρ', and the base flow density gradient, $\partial\bar{\rho}/\partial r$, are set to zero. The resultant eigenvalue problem is then solved using the procedure described in §3.5.

In a full local analysis, the first step is to calculate the absolute growth rate for each streamwise slice by finding saddle points of $\omega(k)$ in the complex k-plane. This determines the locations of absolute instability in the flow, which is a useful diagnostic tool for understanding the behaviour of the global mode. The second step is to estimate the complex frequency of the global mode and the streamwise position of its wavemaker region. These are calculated by continuing the absolute growth rate into the complex x-plane. The third step is to evaluate the local spatial wavenumbers at each slice and then to calculate the corresponding global mode shape by integrating these over the domain. These steps, and their application to a two-dimensional shear flow, are demonstrated in Juniper *et al.* (2011).

The ratio λ_l/L_l, which must be small for a local analysis to be rigorously valid, is labelled ϵ. In the flows featuring vortex breakdown in this thesis, ϵ is small downstream of the vortex breakdown bubble but large around the vortex breakdown bubble. This means that the local analysis becomes invalid around the vortex breakdown bubble. This has a particularly strong effect on the second step so, in this thesis, only the first step is performed.

3

Numerical implementation

In the previous chapter, the linear global stability analysis was formulated and the sensitivity of the eigenvalue to internal feedback and external steady and unsteady forcing was derived. It was shown that the analysis requires a steady solution to the LMN equations, the solution of two large eigenvalue problems to obtain the direct and adjoint global modes, and the solution of a large linear equation to obtain the adjoint base flow. In this chapter, the numerical techniques used for these purposes are described. The techniques rely on direct numerical simulation (DNS) of the LMN equations. The code used is based on the nonlinear DNS code developed by Nichols (2005) and the direct linear and adjoint solvers of Chandler (2010), which were for axisymmetric perturbations. In this chapter, the main features of the code and the procedures for obtaining the steady base flow and the direct and adjoint global modes are outlined. The modifications that were made to handle swirling flow and non-axisymmetric modes of instability are also discussed.

3.1 Details of the code

The code is written in FORTRAN90 and utilizes OpenMP for parallel computation. The equations of motion are discretized on a collocated grid with S_x and S_r points in the axial and radial directions. Sixth-order compact

finite difference schemes are used to calculate spatial derivatives in the axial and radial directions. The co-ordinate singularity at $r = 0$ (the centreline) is treated using an asymptotic method proposed by Constantinescu & Lele (2002).

The equations are solved using an explicit projection method, similar to that used by Chorin (1968). The momentum equations are stepped forward in time, ignoring the pressure gradient term, to give an intermediate momentum field $\mathbf{m}_*$. Taking the divergence of this and including the effect of the change in density from the energy equation leads to a Poisson equation for the pressure. This equation is solved by applying a discrete cosine transform in the axial direction (calculated using Fast Fourier Transforms) and then solving the resulting large matrix inversion problem using an efficient algorithm that is based on the Thomas algorithm. The pressure gradient term is then calculated and used to correct the intermediate field to give the momentum at the next time step.

During the matrix inversion, a Dirichlet condition, $p = 0$, is enforced on Ω_{lat}. Chandler (2010) used a quarter-wave cosine transform to enforce a Neumann condition, $\partial p/\partial x = 0$, on Ω_{in} and a Dirichlet condition, $p = 0$, on Ω_{out}. This is, however, not appropriate for swirling flows because the swirl creates a radial pressure gradient. To resolve this, a half-wave cosine transform is used instead. This enforces a Neumann condition, $\partial p/\partial x = 0$, on both Ω_{in} and Ω_{out}.

Time-stepping is implemented through a fourth-order Runge-Kutta scheme. The coupling between the pressure and the momentum boundary conditions, however, restricts the code to being first order accurate in time. The full details of the code and the nonlinear solution algorithm can be found in Nichols (2005) and Nichols *et al.* (2007).

3.2 Base flow

3.2.1 Procedure

Two methods are used to obtain steady base flows in this thesis. For some flows, it is sufficient to march the nonlinear equations of motion forward in time, while constraining the flow variables to be axisymmetric at each timestep. This works because these flows are globally stable to axisymmetric disturbances. This is true for many uniform-density swirling flows and wake flows.

Other flows, such as the low-density jet studied in Chapter 4, are globally unstable to axisymmetric disturbances. For such flows, standard time-stepping would not lead to a steady base flow. A steady base flow can be obtained for such cases by applying selective-frequency damping (SFD) (Akervik *et al.*, 2006) to the nonlinear DNS. At every timestep, unstable frequencies are damped through the use of a low-pass filter. The advantage of this method, compared to other techniques such as Newton iteration methods, is that it requires making very little changes to the existing code, is easy to implement, does not require large computational memory, and does not require a good initial guess to converge to a steady solution. In contrast, Newton methods require a good initial guess to converge to a steady solution, and require large computational expense becasue a large matrix problem has to be solved at each iteration.

The steady axisymmetric base flow satisfies equation (2.3) in the limit $\partial \mathbf{q}/\partial t = 0$. Practically, a steady state is assumed when the l^2-norm of the difference between the base flow state vectors at two successive time-steps is less than 10^{-6}.

3.2.2 Boundary Conditions

A suitable inlet flow profile is imposed on Ω_{in}. This consists of specifying profiles for the three components of the velocity, and the temperature or mixture fraction profile, which determines the density profile. This profile is specific to each flow being studied. In this thesis, the cases studied are a low-density non-swirling jet (Chapter 4), a uniform-density swirling jet model known as the Grabowski profile (Chapter 5), a swirling jet model that represents velocities measured in experiments (Chapter 6), and a diffusion flame formed in a low-density non-swirling (Chapter 8), and swirling jet (Chapter 9).

The boundary conditions on the lateral and outlet boundaries are chosen so as to model flow into a semi-infinite domain in the downstream and radial directions. For the momentum, a traction-free boundary condition ($\tau \cdot \hat{\mathbf{n}} = 0$, where $\hat{\mathbf{n}}$ is the unit vector normal to the boundary) is applied on Ω_{lat}, and a convective boundary condition ($\partial \mathbf{m}/\partial t + U_c \cdot \partial \mathbf{m}/\partial x = 0$ with U_c set to the maximum outlet axial velocity) is applied on Ω_{out}. For the temperature, a Dirichlet boundary condition ($T = 0$) is applied on Ω_{lat} and a convective boundary condition is applied on Ω_{out}.

The introduction of swirl affects the boundary condition used for the intermediate momentum in the projection step. The boundary condition on the intermediate momentum needs to be compatible with the actual momentum and pressure boundary conditions. The momentum at the $(n+1)$-th time step is related to the intermediate momentum by

$$\bar{\mathbf{m}}_{n+1} = \bar{\mathbf{m}}_* - \Delta t \nabla \bar{p}. \tag{3.1}$$

Hence, the boundary conditions on the components of the intermediate mo-

mentum are given by

$$\bar{m}_x^* = \bar{m}_x^{n+1} + \Delta t \frac{\partial \bar{p}}{\partial x}, \tag{3.2a}$$

$$\bar{m}_r^* = \bar{m}_r^{n+1} + \Delta t \frac{\partial \bar{p}}{\partial r}, \tag{3.2b}$$

$$\bar{m}_\theta^* = \bar{m}_\theta^{n+1} + \frac{\Delta t}{r} \frac{\partial \bar{p}}{\partial \theta}. \tag{3.2c}$$

Because we are considering axisymmetric flow, the $\partial \bar{p}/\partial \theta$ term is zero everywhere. On Ω_{in}, the Poisson solver enforces $\partial p/\partial x = 0$, but $\partial p/\partial r$ is not zero for a swirling flow. Therefore, only the intermediate radial momentum at Ω_{in} needs to be corrected using $\partial p/\partial r$ from the previous time step. The intermediate axial and azimuthal momentum boundary conditions are identical to the actual momentum boundary conditions. For a domain of sufficiently large radius R_{max}, it has been found to be safe to use the same boundary condition for the intermediate momentum and the actual momentum. This relies on the azimuthal velocity being sufficiently small near Ω_{lat}. The convective boundary condition on Ω_{out} is applied before the intermediate momentum is calculated and an explicit boundary condition for the intermediate momentum is not required.

3.3 Direct and adjoint global modes

3.3.1 Procedure

The linear direct and adjoint global modes are calculated by solving the discretized versions of the eigenvalue problems (2.7) and (2.16). Instead of using a large matrix approach, this is done using ARPACK, a software library that implements the implicitly restarted Arnoldi method (IRAM) (Lehoucq *et al.* (1998)) to obtain the eigenvalues and eigenmodes of a standard eigenvalue problem

$$A\mathbf{x} = \lambda \mathbf{x}. \tag{3.3}$$

The Arnoldi method is an iterative method. It starts off with a guess solution for the eigenmodes, and, at each iteration, produces a better approximation to the actual eigenmodes of the problem. The convergence of the solution is determined by computing a residual. The iterations are stopped when the residual falls below a specified threshold.

In this thesis, the matrix A corresponds to the matrix exponential of the discretized versions of the linear direct or adjoint operators $\mathbf{L}_m$ or $\mathbf{L}_m^+$ over a time-period ΔT. The matrix-vector product $A\mathbf{x}$ is achieved by using the linear direct or adjoint code to march an initial state vector provided by ARPACK forward by a time $\Delta T = N\Delta t$, where Δt is the uniform time-step employed for each of the N time-steps. None of these matrices is ever constructed in full.

The eigenfunctions of $\mathbf{L}_m$ or $\mathbf{L}_m^+$ are the same as those of A, whereas the eigenvalues are related by

$$\lambda_A = e^{\lambda_L \Delta T}, \tag{3.4a}$$

$$\lambda_L = \frac{\ln \lambda_A}{N\Delta t}, \tag{3.4b}$$

where the subscripts A and L refer to the corresponding matrices. In practice, the convergence of ARPACK is influenced by the time ΔT. If the value of ΔT is too large or too small in comparison to the period of the eigenmode, convergence will be slow. In practice, ΔT is set to a value that is around 60% of the period of the global mode for the flow case being investigated. (Chandler, personal communication, 2010)

An alternative to this matrix-free time-stepping approach to obtain the eigenmodes is to construct a large matrix. In both cases, the Arnoldi method may be used. The latter approach requires a large amount of memory because the discretized versions of L are often dense matrices in practice (Theofilis, 2003). The boundary conditions on these matrices have to be treated with care because these matrices can often be near-singular. The large-

matrix approach also often leads to spurious pressure modes. In contrast, these problems were not encountered with the time-stepping approach implemented here. One disadvantage of the time-stepping approach, however, is that the eigenmodes are affected by the temporal accuracy of the time-stepping scheme. The code used for this thesis is only first-order accurate in time, so small time-steps need to be used for high-accuracy. The choice of time-step is further affected by the fact that, for three-dimensional perturbations developing over a swirling base flow, the CFL number for numerical stability is smaller than for two-dimensional perturbations developing over a non-swirling base flow. Although the time-stepping approach is easier to implement and has low memory usage, it can take more computational time.

The solution algorithms used are identical to those developed by Chandler (2010). Complex versions of the direct linear and adjoint codes developed by Chandler (2010) have been developed. Complex numbers are required to handle the imaginary components that arise when non-zero azimuthal modes of swirling flows are considered. Following the approach of Heaton *et al.* (2009), this has been implemented by working with two sets of real variables (representing the real and imaginary parts) rather than a single set of complex variables. This is becase it was not clear how the low-level routines in Nichols' DNS code would deal with complex variables. In terms of computational costs, the two approaches are more or less equivalent because FORTRAN deals with a complex variable by storing it as two real variables.

3.3.2 Boundary conditions

In the direct code, a homogenous Dirichlet boundary condition is used for the momentum and temperature on Ω_{in}, Ω_{lat}, and Ω_{out}. On Ω_{out}, a convective boundary condition is used. The pressure boundary conditions are identical to those used for the base flow. The boundary conditions on the intermediate momentum are derived in the same way as for the base flow. On Ω_{in}, the radial and azimuthal intermediate momentum fields need to be

corrected with the pressure from the previous time-step. On Ω_{lat}, only the radial intermediate momentum is corrected with the pressure from the previous time-step. On Ω_{out}, no correction is required as the convective boundary condition sets the correct condition on the intermediate momentum.

In the adjoint code, the boundary conditions have to be chosen such that the boundary terms arising from the derivation of the adjoint equations are zero. It is sufficient to use homogeneous Dirichlet boundary conditions for the adjoint momentum and temperature on all boundaries. The boundary conditions on the intermediate momentum are derived in the same way as for the base flow and direct code. The radial intermediate momentum field is corrected on Ω_{lat}, while the radial and azimuthal intermediate momentum fields on Ω_{in} and Ω_{out} are corrected with the pressure from the previous time-step.

The centreline boundary conditions have to be worked out for non-zero azimuthal modes based on the asymptotic analysis of Constantinescu & Lele (2002).

This gives, at the centreline $r = 0$

for $m = 0$,

$$\begin{aligned} m_x &= \text{derived using asymptotics}, && (3.5a)\\ m_r &= 0, && (3.5b)\\ m_\theta &= 0, && (3.5c)\\ T &= \text{derived using asymptotics}, && (3.5d) \end{aligned}$$

for $m = \pm 1$,

$$\begin{aligned} m_x &= 0, && (3.6a)\\ \mathrm{Re}(m_r) &= m.\mathrm{Im}(m_\theta), && (3.6b)\\ \mathrm{Im}(m_r) &= -m.\mathrm{Re}(m_\theta), && (3.6c)\\ T &= 0, && (3.6d) \end{aligned}$$

and for $|m| > 1$,

$$m_x = 0 \tag{3.7a}$$
$$m_r = 0 \tag{3.7b}$$
$$m_\theta = 0 \tag{3.7c}$$
$$T = 0 \tag{3.7d}$$

3.4 Adjoint base flow

The adjoint base flow is obtained by solving the discretized version of the set of equations (2.28). A matrix-free time-stepping approach is used once again. Time-derivative terms are added to the LHS of equations (2.28)b-c and the adjoint time-stepping code is modified to solve this new set of equations. The equations are marched forward in time until the l^2-norm of the difference between the adjoint base flow state vectors at two successive time-steps is less than 10^{-8}.

As mentioned in section 2.4.1, for an axisymmetric base flow, the adjoint base flow is also axisymmetric. The centreline conditions on the adjoint base flow are obtained following equations (3.5). The boundary conditions are identical to the boundary conditions in the adjoint code.

3.5 Local stability analysis

The local stability analysis is carried out using the MATLAB-based program *Instaflow*, described in detail in Juniper *et al.* (2011). At each streamwise location, the four ODEs arising from §2.6 are discretized on a Chebyshev-spaced grid in the r-direction. This produces a generalized matrix eigenvalue problem, which is the dispersion relation for this slice of the flow.

This dispersion relation is solved to obtain the complex absolute fre-

quency, ω_0, as a function of streamwise distance, x, by finding saddle points in the complex k-plane and then checking that they are valid pinch points, as defined by Briggs-Bers (Briggs, 1964).

4

Passive control of global instability in low-density jets

This chapter is devoted to studying the passive control of low-density jets near the point of instability. A low-density jet can either be a hot jet, in which the temperature of the jet fluid is higher than that of the ambient fluid, or a light jet, in which the molecular weight of the jet species is lower than that of the surrounding fluid. In this chapter, an isothermal helium jet near the threshold of global instability is considered. The structural sensitivity is obtained and compared with that from a local stability analysis. The sensitivity of the marginally unstable eigenvalue to open-loop steady forcing is obtained and this is used to study how a thin hot-wire can be used to control the growth rate and frequency of the global mode.

The content of this chapter has been submitted as a journal article to Physics of Fluids, co-authored with Gary Chandler and Matthew Juniper. The local absolute growth rate has been obtained by Matthew Juniper.

4.1 Introduction

Many studies have shown that the stability of a jet discharging into an ambient fluid depends strongly on the jet's density. For example, spectra of

hot-wire velocity measurements in helium-air jets (Sreenivasan *et al.*, 1989) and pressure measurements in heated air jets (Monkewitz *et al.*, 1990) showed that low density jets exhibit sharp discrete peaks in the measured spectra, while uniform density jets exhibit weak broad peaks. These sharp discrete peaks are caused by self-excited varicose oscillations in the low-density jets, which arise because the initially steady jet is globally unstable. (Lesshafft *et al.*, 2006)

Several experimental studies have examined the control of these self-excited oscillations. These studies have used loudspeakers for active feedback control (Hallberg & Strykowski, 2008), and thin hot wires (Srinivasan *et al.*, 2010) or co-flow (Hallberg *et al.*, 2007) for passive control. The goal of such control is to render the jet globally stable, either by adding a feedback mechanism or by perturbing the base flow. For this goal, a global linear stability analysis around the steady base flow is the most appropriate tool, both in the form of a structural sensitivity analysis (Giannetti & Luchini, 2007) and a base flow sensitivity analysis (Hill, 1992; Marquet *et al.*, 2008*a*). These analyses require the direct global mode and the adjoint global mode to be calculated. Apart from one example in Chandler *et al.* (2012), which was included in order to demonstrate the technique, equivalent results for the low density jet have not yet been published.

In this numerical study, we perform a structural sensitivity analysis and a base flow sensitivity analysis on a low-density jet. We use the low Mach number formulation of the Navier–Stokes (NS) equations. This is well-adapted to studies of hydrodynamic instability in low-density jets and flames because it permits density variations due to temperature and species composition but excludes acoustic waves. This significantly reduces the computational effort. By overlapping the direct and adjoint global modes, we determine the wavemaker region. Then, by performing a base flow sensitivity analysis, we identify the regions of the flow in which the introduction of a thin axisymmetric control ring can change the frequency or growth rate of the global instability. We also determine the influence of heat transfer from the ring,

which has a particularly strong influence on the instability of a low-density jet. By examining the sizes of advection and production terms in the governing equations, we identify the physical mechanisms that are responsible for this influence.

4.2 Flow configuration

We study the axisymmetric motion of a low-density jet in a cylindrical domain that has radius R_{max} and length X_{max}. The jet fluid enters the domain at $x = 0$ and is aligned along the axis, $r = 0$. The fluid in the domain is described in terms of its velocity $\mathbf{u} = (u_x, u_r)^T$, density ρ, and temperature T. A difference in chemical species between the jet fluid and the surrounding fluid is described using the mixture fraction, Z, which has a value of $Z = 1$ for the jet species and $Z = 0$ for the surrounding fluid. The reacting LMN equations, with $Da = 0$, are used to describe the fluid motion.

The flow variables are nondimensionalized by the jet diameter, the jet axial velocity at inlet, and the ambient density. The nondimensional temperature is defined as $T = (T^* - T_0)/(T_1 - T_0)$, where T^* is the dimensional temperature, T_1 is the maximum temperature, and T_0 is the ambient temperature. The ratio of the ambient density to the jet density defines the density ratio parameter, S_1, and the ratio of the maximum temperature to the ambient temperature defines the temperature ratio parameter, S_2. The Reynolds number, Re, is defined in terms of the jet diameter, jet axial velocity at inlet and jet density. The Prandtl number, Pr, and Schmidt number, Sc, describe the ratio of the diffusivity of temperature and mass, respectively, to the diffusivity of momentum and are assumed to be constant throughout the flow. In this study, we consider an isothermal helium jet exiting into atmospheric conditions. This flow has a density ratio of $S_1 = 7.0$. For an isothermal flow, S_2 can be set to any value other than 1.0. This is because, for an isothermal flow, it defines a nominal temperature to nondimensionalize the equations of motion. We set $S_2 = 2.0$ for simplicity and set $Pr = Sc = 1.0$, in line with

Lesshafft *et al.* (2006).

The governing equations (see §2.5) are expressed in terms of the state vector $\mathbf{q} \equiv (m_x,\, m_r,\, Z,\, T)^T$, as in chapter 2. We use a grid with 181×1449 points for a domain measuring 8.0×36.0 in the radial and axial directions respectively, which has been shown to produce results that are sufficiently well-resolved (Chandler *et al.*, 2012).

Along the lateral boundary, at $r = R_{max}$, we use a viscous traction free boundary condition for the momentum and set $T = 0$ and $Z = 0$. At the outlet boundary, at $x = X_{max}$, we use a convective boundary condition for the momentum, temperature and species. These boundary conditions model flow into a semi-infinite domain in the downstream and radial directions. The pressure-projection scheme used in the code uses a discrete cosine transform to set boundary conditions for the pressure at the inlet and outlet boundaries. For this study, we use a half-wave cosine transform, which sets $dp/dx = 0$ at the inlet and outlet boundaries. Along the lateral boundary, we set $p = 0$. At the inlet to the domain, we impose velocity and mixture fraction profiles formed from Michalke's profile number two (Michalke, 1984), with a shear-layer thickness parameter $D/2\theta_0 = 14.0$. This signifies that the momentum thickness of the shear layer is 14 times smaller than the jet radius, which corresponds to a thinner shear-layer than the ones considered in Chandler *et al*'s original study, which had $D/2\theta_0 = 12.5$ (Chandler *et al.*, 2012). We also add a co-flow velocity of 1% of the jet velocity around the jet to improve numerical stability. This helps to convect numerical errors out of the computational domain.

This study is performed near the threshold of global instability, at which point a linear global stability analysis is most valid. For this set of parameters and inlet profile, we find that this is at $Re = 470$. In comparison, Hallberg & Strykowski (2006) (Figure 5) report the onset of global instability in a helium jet of similar shear-layer thickness at approximately $550 \leq Re \leq 750$. We attribute the difference between our linear global stability analysis and

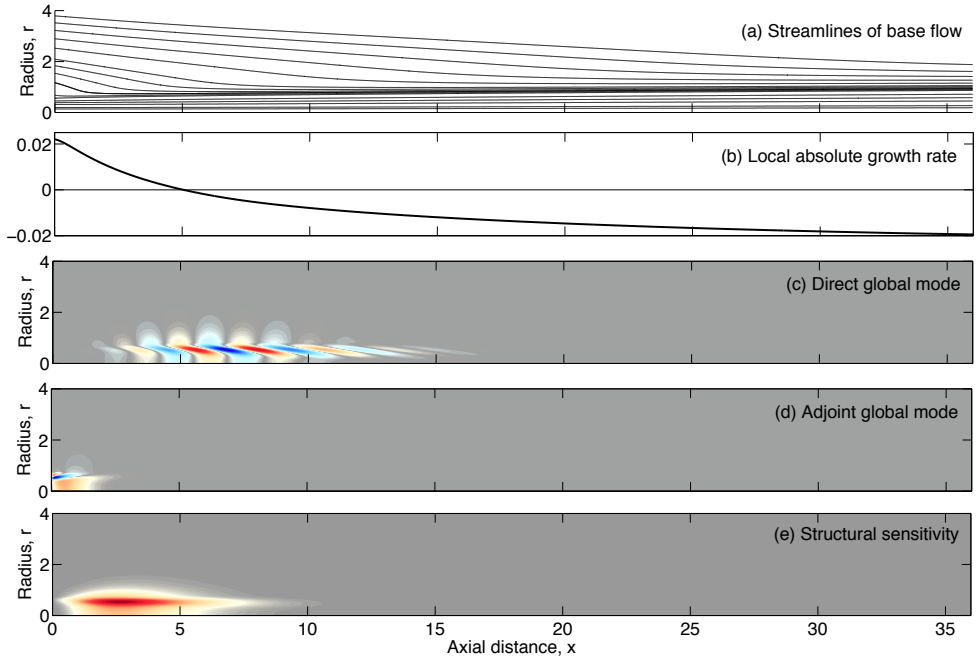

Figure 4.1: (a) Streamlines of the base flow and (b) the local absolute growth rate of an isothermal helium jet at $Re = 470$. (c) The direct global mode and (d) the adjoint global mode, shown as the real part of the axial momentum of the least stable mode. (e) The structural sensitivity.

their experimental observations to the effect of variable transport properties and the differences in the jet velocity and density profiles. Both of these have been found to have a significant effect on the onset of absolute instability in low-density jets. (Coenen & Sevilla, 2012; Lesshafft & Marquet, 2010)

4.3 Global stability and structural sensitivity

We obtain a steady axisymmetric base flow, $\bar{\mathbf{q}}(\mathbf{x}, \mathbf{r})$, such that $\mathcal{N}(\bar{\mathbf{q}}) = 0$, using selective frequency damping (SFD) (Akervik *et al.*, 2006). The streamlines of this base flow are shown in figure 1(a). The entrainment of the ambient fluid into the jet is significant and we will show later in the chapter that it can have a strong effect on the stability of the flow. The local absolute growth rate is shown in figure 1(b).

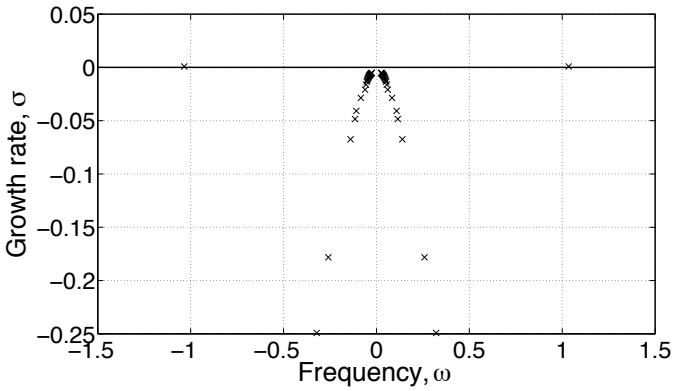

Figure 4.2: Eigenvalue spectrum for $m = 0$ for the base flow shown in figure 4.1(a). The 25 least stable modes are shown.

The evolution of small perturbations $\mathbf{q}'$ around this steady base flow is governed by the linearized LMN equations. We consider axisymmetric perturbations ($m = 0$) and obtain the direct and adjoint global modes by solving the associated eigenvalue problems using the numerical scheme described in Chapter 3.

Figure 4.2 shows the eigenvalues corresponding to the 25 least stable modes. At this Reynolds number, we find one mode that is marginally unstable, and a branch of low-frequency stable modes. These stable modes arise from the continuous spectrum in the local analysis and correspond to free-stream vortical modes - similar to those observed by Garnaud (2012) in a uniform-density jet.

The direct global mode, $\hat{\mathbf{q}}(x, r)$, corresponding to the marginally unstable mode is shown in figure 4.1(c). Its corresponding adjoint global mode, $\hat{\mathbf{q}}^+(x, r)$, is shown in figure 4.1(d) and the structural sensitivity, defined here as the Frobenius norm of the tensor $S_{ij} = \hat{\mathbf{m}}_i(\hat{\mathbf{m}}_j^+)^*$, is in figure 4.1(e).

The absolute growth rate decays monotonically from the entrance plane and the flow is absolutely unstable for $0 \leq x < 5.0$. The structural sensi-

tivity, however, is maximal in the shear layer, at $x = 2.66$. The structural sensitivity identifies the region of the flow that is most sensitive to internal feedback mechanisms - where the direct global mode optimally excites itself. (Giannetti & Luchini, 2007). This region can be referred to as the core of the instability, or the wavemaker region, because it is most influential in determining the natural (uncontrolled) dynamics of the flow. In the context of passive control, it is useful to identify this region as it provides information about the origin of the global instability. This region does not, however, necessarily correspond to the region where an external control force has most influence on the growth rate and frequency of the unstable mode. This is because a control force also changes the baseflow and this change in the baseflow is not accounted for in the structural sensitivity.

4.4 Sensitivity to a control force

We now consider the effect of a small control force on the marginally unstable eigenvalue. We model the control force by adding source terms to the right-hand side of the nonlinear LMN equations, following the approach in Chapter 2. The source term in the species equation is set to zero. The sensitivity of the eigenvalue to a small steady force is obtained from the adjoint base flow, $\bar{\mathbf{q}}^+ = \left(\bar{m}_x^+, \bar{m}_r^+, \bar{Z}^+, \bar{T}^+\right)^T$.

Figure 4.3 shows the adjoint base flow fields for the marginally unstable global mode of the isothermal helium jet at $Re = 470$. The real part of the adjoint base flow fields determines the sensitivity of the growth rate to steady forcing, which determines whether the unstable mode is promoted or suppressed. The imaginary part determines the sensitivity of the frequency to steady forcing. This is of interest from an experimental point of view, because changes in frequency are easier to measure than changes in growth rate.

The sensitivities exhibit an oscillatory pattern. The global mode arises due to contributions from feedback throughout the wavemaker region. These contributions interact constructively and destructively to give, in aggregate,

a global mode frequency and growth rate. If the steady force (to the non-linear NS equations) is applied at one point in the wavemaker region, then the effect on the global mode will depend on the amplitude and the phase of the feedback from this point, relative to the aggregate feedback from the other points. The phase relationship of the feedback oscillates in space, so the effect of a small change in the feedback at a point also oscillates in space.

The adjoint base flow temperature describes the sensitivity to heat input. The flow is most sensitive to heat input just outside the helium jet, up to around 2 jet diameters from the injection plane. In this region, the figure 2(a) (bottom left) shows that adding heat makes the flow more stable. Physically this is because heat addition reduces the density of the outer fluid. This agrees with the predictions of Srinivasan *et al.* (2010), who used a local stability analysis to predict that heating in the ambient fluid near the jet nozzle can eliminate absolute instability. By comparing the bottom-left frame in figure 4.3(a) with the streamlines in figure 4.1(a), it is clear that contours of maximum influence approximately follow the streamlines. It appears therefore that the change induced by the heat source has most effect when it is advected onto the region around $(x, r) = (2, 0.5)$, which is the centre of the wavemaker region as shown in figure 4.1(d). Consequently, the sensitivities in the regions outside the jet depend quite sensitively on the streamlines here and therefore on the degree of co-flow. The result that is most contrary to expectations is that heating the jet core around two diameters downstream has a stabilizing effect. In order to verify this, we carried out checks (detailed in §4.8) and found that heating the jet core two diameters downstream reduced the growth rate of the linear global mode, as predicted by the sensitivity analysis.

Unsurprisingly, radial momentum forcing has little influence, except in the shear layer at the jet exit plane (figure 4.3 centre). Axial momentum forcing has most influence just outside the jet, around the wavemaker region. In this region, figure 4.3(b) (top-right) shows that adding a force in the positive x-direction decreases the global mode frequency. The information in

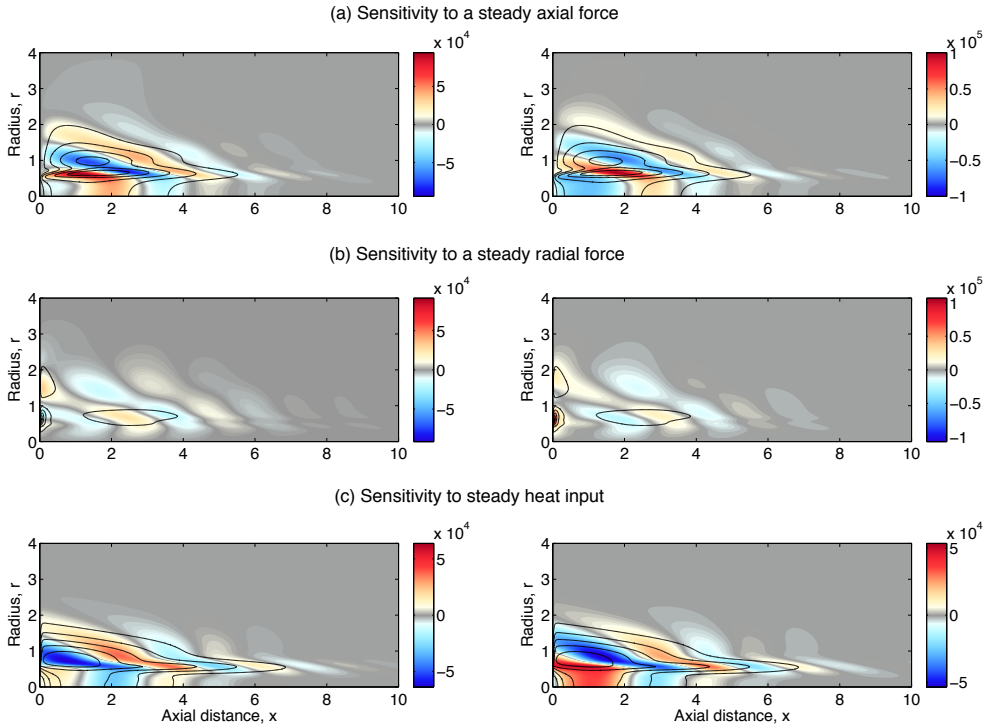

Figure 4.3: The sensitivity of the marginally unstable eigenvalue of a helium jet at Re=470 to steady forcing, $\nabla_{\bar{\mathbf{F}}}\lambda$. The colours show the sensitivity of the growth rate, $\nabla\sigma$ (left), and frequency, $\nabla\omega$ (right) to a (a) steady axial body force, $\bar{F}_x$ (b) steady radial body force, $\bar{F}_r$, and (c) steady heat input, $\bar{\psi}_T$. The contour lines show the absolute value of $\nabla\lambda$ for each row.

these figures is most instructive when it is combined in order to calculate the influence of a physical object, two of which we consider in the next section.

4.5 Passive control using an axisymmetric control ring

4.5.1 The effect of an adiabatic control ring

We now assume that the control force is provided by a thin ring at the same temperature as the fluid, which we call an adiabatic ring. The ring is at (x_c, r_c), centred on the jet axis, and provides a force on the flow that

is equal and opposite to the drag force on the ring. The ring is thin, so the nondimensional steady and unsteady components of this force can be modelled by those on a cylinder:

$$\bar{\mathbf{F}}(x,r) = -\alpha\bar{\rho}|\bar{\mathbf{u}}|\bar{\mathbf{u}}\delta^2(x-x_c, r-r_c), \tag{4.1a}$$

$$\mathbf{f}'(x,r,t) = \hat{\mathbf{f}}(x,r)e^{\lambda t}, \tag{4.1b}$$

$$\text{where} \quad \hat{\mathbf{f}}(x,r) = -\left(\alpha\hat{\rho}|\bar{\mathbf{u}}|\bar{\mathbf{u}} + \alpha\bar{\rho}|\bar{\mathbf{u}}|\hat{\mathbf{u}} + \alpha\bar{\rho}\frac{\bar{\mathbf{u}}\cdot\hat{\mathbf{u}}}{|\bar{\mathbf{u}}|}\bar{\mathbf{u}}\right)\delta^2(x-x_c, r-r_c) \tag{4.1c}$$

.

The coefficient α equals $d_w C_D$, where C_D is the drag coefficient and d_w is the wire diameter nondimensionalized by the jet diameter. We set $C_D = 1.5$, based on numerical drag calculations by Sheard *et al.* (2005). We set $d_w = 0.1$, which corresponds to a maximum local Reynolds number around 50, because this is below the Reynolds number at which the ring causes its own self-excited oscillations (Sheard *et al.*, 2005). Therefore, the linearized drag force oscillates only at the frequency of the global mode, λ.

The changes in the eigenvalue due to the steady and unsteady components of the drag force are $\delta\lambda_{\bar{\mathbf{F}}} = \langle\bar{\mathbf{m}}^+, \bar{\mathbf{F}}\rangle$ and $\delta\lambda_{\mathbf{f}'} = \langle\hat{\mathbf{m}}^+, \hat{\mathbf{f}}\rangle$. These are summed to obtain the total change in the eigenvalue, $\delta\lambda_{drag}$. Figure 4.4 shows the change in the growth rate and frequency (scaled by $C_D d_w$) as a function of the location of the control ring. This shows where the control ring has most influence. The drag from the ring increases as the flow velocity at the ring increases, so the ring has little effect where the base flow is slow, even if the eigenmode is quite sensitive to momentum forcing there. This is why figure 4.4 (sensitivity to a control ring) has highest amplitudes in the jet region ($0 < r < 0.5$) despite the fact that figure 4.3 (sensitivity to steady forcing) has highest amplitudes outside the jet region.

The ring has maximum influence when placed at $(x_c, r_c) = (1.54, 0.43)$, at which point it is stabilizing. Furthermore, it decreases the oscillation frequency when placed at $0 < x < 2.0$ and increases the frequency when placed

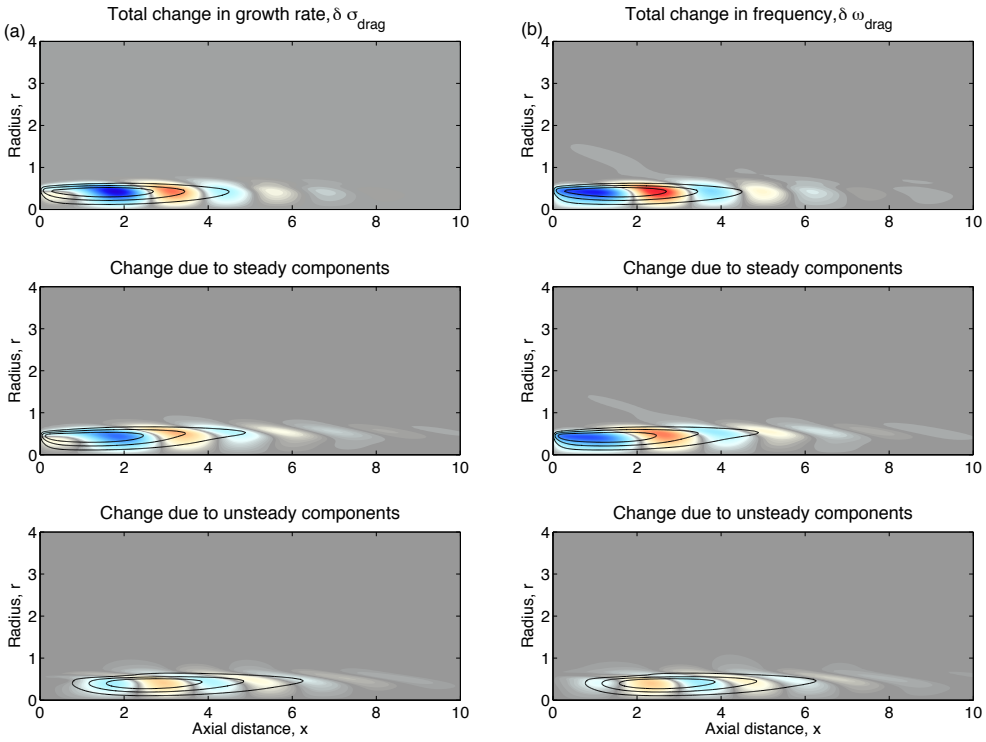

Figure 4.4: The predicted change (scaled by $C_D d_w$) in the marginally unstable eigenvalue of a helium jet due to the drag on a thin axisymmetric control ring, $\delta\lambda_{drag}$. The colours show the real (left) and imaginary (right) parts of the total change in the eigenvalue, $\delta\lambda_{drag}$ (top), the change due to the steady component of the drag force, $\delta\lambda_{\bar{\mathbf{F}}}$ (middle), and the change due to the unsteady component of the drag force, $\delta\lambda_{\mathbf{f}'}$ (bottom). The contours show the absolute value of $\delta\lambda$ for each row. The shading on all the plots is equal and goes from -0.0043 (blue) to 0.0043 (red).

at $2.0 < x < 3.2$. These features could be tested in experiments, during which it will be easier to measure changes in the frequency than changes in the growth rate. It is interesting to note that the steady component of the drag force influences the eigenvalue around 3 times more than the unsteady component.

4.5.2 The effect of a heated control ring

We now consider the additional influence of heat transfer from a hot ring. Chandler (2010) calculated the steady and unsteady components of the heat transfer to be:

$$\bar{\psi}_T(x,r) = c_\psi d_w^\eta |\bar{\mathbf{m}}|^\eta (T_w - \bar{T})\delta^2(x - x_c, r - r_c), \tag{4.2a}$$

$$\psi'_T(x,r,t) = \hat{\psi}_T(x,r)e^{\lambda t}, \tag{4.2b}$$

$$\text{where} \quad \hat{\psi}_T(x,r) = c_\psi d_w^\eta |\bar{\mathbf{m}}|^\eta \left((T_w - \bar{T})\eta \frac{\mathbf{m}' \cdot \bar{\mathbf{m}}}{|\bar{\mathbf{m}}|^2} - T' \right) \delta^2(x - x_c, r - r_c). \tag{4.2c}$$

T_w is the nondimensional wire temperature and c_ψ and η, which are functions of the Nusselt and Reynolds numbers, are taken to be $c_\psi = 58.3$ and $\eta = 0.33$ following Chandler (2010). We consider a small increase in the ring temperature, $T_w = 0.01$.

The changes in the eigenvalue due to the steady and unsteady components of the heat transfer are $\delta\lambda_{\bar{T}} = \langle \bar{T}^+, \bar{\psi}_T \rangle$ and $\delta\lambda_{T'} = \langle \hat{T}^+, \hat{\psi} \rangle$. These are summed with the changes due to the drag, $(\delta\lambda_{drag})$ to obtain the total change in the eigenvalue, $\delta\lambda_{hotring}$. Figure 4.5 shows these total changes as a function of the location of the hot ring. When it is hot, the wire has more influence in the low speed regions outside the jet than when it is adiabatic, as shown by the fact that figure 4.5 is more similar to figure 4.3(bottom) than figure 4.4 is to figure 4.3(top). This is because the heat transfer depends much less on the local velocity than the drag force does (the exponent of velocity is $\eta = 0.33$ in equation (4.2a) but 2 in equation (4.1a)). The hot ring stabilizes

the flow when placed just outside the shear layer, around $0.5 < x < 2.0$, because it reduces the density there. It also has a strong effect when placed at a larger radius. This is because the density reduction caused by the heat transfer is advected along the streamlines to the jet. This advection depends strongly on the streamlines and therefore on the degree of co-flow.

4.6 A physical interpretation of the control in terms of the modification of the base flow

In order to examine the physical mechanisms that cause the eigenvalue to change, we study the effects of a drag force and heat source in more detail. We only analyse the steady components because they contribute much more than the unsteady components. Firstly, we consider the effect of a drag force at $(x_c, r_c) = (1.0, 0.5)$, which is in the shear layer. Secondly, we consider the effect of a heat source at $(x_c, r_c) = (0.5, 0.25)$, which is in the jet core. In each case, we calculate the change in the base flow, $\delta\bar{q} = (\delta\bar{m}_x, \delta\bar{m}_r, \delta\bar{Z}, \delta\bar{T}, \delta\bar{\rho})^T$, caused by the steady force. Then we use the sensitivity to base flow modifications (equations (2.43) and (2.44)) to work out the contributions of the change in axial momentum, radial momentum, mixture fraction and density profiles to the change in the eigenvalue. The total change in the eigenvalue is given by the sum of these contributions

$$\begin{aligned} \delta\lambda_{tot} &= \delta\lambda_{\bar{m}_x} + \delta\lambda_{\bar{m}_r} + \delta\lambda_{\bar{Z}} + \delta\lambda_{\bar{T}} + \delta\lambda_{\bar{\rho}} && (4.3) \\ &= \langle \bar{f}_x^+, \delta\bar{m}_x \rangle + \langle \bar{f}_r^+, \delta\bar{m}_r \rangle + \langle \bar{\psi}_Z^+, \delta\bar{Z} \rangle + \langle \bar{\psi}_T^+, \delta\bar{T} \rangle + \langle \bar{\varrho}^+, \delta\bar{\rho} \rangle . && (4.4) \end{aligned}$$

We then split these contributions into production terms and advection terms, as in previous studies on incompressible and compressible flows (Marquet *et al.*, 2008*a*; Meliga *et al.*, 2010). The stability of the flow is determined by a competition between the production of disturbances at a point and their advection away from that point. An increase in production or a decrease in advection are destabilizing, while a decrease in production or an increase in

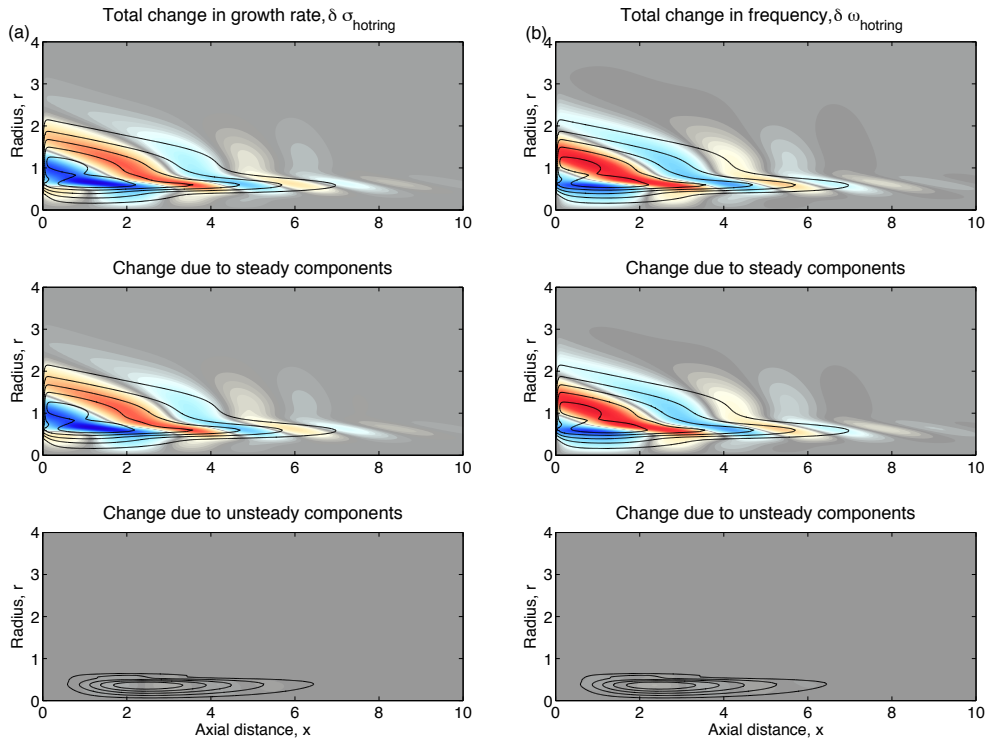

Figure 4.5: The predicted change in the marginally unstable eigenvalue of a helium jet, $\delta\lambda_{hotring}$, due to the drag and heat transfer from a thin hot ring with $d_w = 0.1$ and $T_w = 0.01$. The colours show the real (left) and imaginary (right) parts of the total change in the eigenvalue, $\delta\lambda_{hotring}$ (top), the change due to the steady components of the drag and heat transfer, $\delta\lambda_{\bar{\mathbf{F}}} + \delta\lambda_{\bar{T}}$ (middle), and the change due to the unsteady components of the drag and heat transfer, $\delta\lambda_{\mathbf{f}'} + \delta\lambda_{T'}$ (bottom). The contours show the absolute value of $\delta\lambda$ for each row. The shading on all the plots is equal and goes from -0.0068 (blue) to 0.0068 (red).

advection are stabilizing. To identify these terms in the LMN equations, we express the direct linear equations in terms of the velocity, rather than the momentum. The advective terms can then be identified easily and re-expressed in terms of the momentum. The sensitivity of the advective terms in the linearized LMN equations to base flow modifications are:

$$\begin{aligned}
\bar{f}^+_{i,Adv} &\equiv -\hat{m}^+_j \frac{\partial}{\partial x_i}\left(\frac{\hat{m}^*_j}{\bar{\rho}}\right) + \frac{\hat{m}^+_i \bar{m}_j}{\bar{\rho}} \frac{\partial}{\partial x_j}\left(\frac{\hat{\rho}^*}{\bar{\rho}}\right) + \frac{\hat{m}^+_j \bar{m}_j}{\bar{\rho}} \frac{\partial}{\partial x_i}\left(\frac{\hat{\rho}^*}{\bar{\rho}}\right) \cdots \\
&\cdots - \left(\frac{\hat{T}^+}{\bar{\rho}} + \bar{K}_1 \hat{p}^+\right) \frac{\partial \hat{T}^*}{\partial x_i} - \left(\frac{\hat{Z}^+}{\bar{\rho}} + \bar{K}_2 \hat{p}^+\right) \frac{\partial \hat{Z}^*}{\partial x_i} \cdots \\
&\cdots - \frac{\hat{p}^+}{\bar{\rho}} \frac{\partial}{\partial x_i}\left(\frac{\hat{\rho}^*}{\bar{\rho}}\right) - \frac{\hat{\rho}^*}{\bar{\rho}^2}\left(\hat{Z}^+ \frac{\partial \bar{Z}}{\partial x_i} + \hat{T}^+ \frac{\partial \bar{T}}{\partial x_i}\right), \qquad (4.5)
\end{aligned}$$

$$\bar{\psi}^+_{Z,Adv} \equiv \bar{m}_j \frac{\partial}{\partial x_j}\left(\frac{\hat{\rho}^* \hat{Z}^+}{\bar{\rho}^2}\right) - (S_2 - 1)(S_1 - 1)\hat{p}^+ \bar{m}_j \frac{\partial \hat{T}^*}{\partial x_j}, \qquad (4.6)$$

$$\bar{\psi}^+_{T,Adv} \equiv \bar{m}_j \frac{\partial}{\partial x_j}\left(\frac{\hat{\rho}^* \hat{T}^+}{\bar{\rho}^2}\right) - (S_2 - 1)(S_1 - 1)\hat{p}^+ \bar{m}_j \frac{\partial \hat{Z}^*}{\partial x_j}, \qquad (4.7)$$

$$\begin{aligned}
\bar{\varrho}^+_{Adv} &\equiv -\frac{\hat{m}^*_i \bar{m}_j}{\bar{\rho}^2} \frac{\partial \hat{m}^+_i}{\partial x_j} - \frac{\hat{m}^+_i \bar{m}_i \bar{m}_j}{\bar{\rho}^2} \frac{\partial}{\partial x_j}\left(\frac{\hat{\rho}^*}{\bar{\rho}}\right) + \frac{\bar{m}_i \bar{m}_j \hat{\rho}^*}{\bar{\rho}^2} \frac{\partial}{\partial x_j}\left(\frac{\hat{m}^+_i}{\bar{\rho}}\right) \cdots \\
&\cdots + \frac{\hat{m}^+_i \bar{m}_j \hat{\rho}^*}{\bar{\rho}^2} \frac{\partial \bar{m}_i}{\partial x_j} + \frac{\hat{p}^+ \bar{m}_j}{\bar{\rho}^2} \frac{\partial}{\partial x_j}\left(\frac{\hat{\rho}^*}{\bar{\rho}}\right) - \frac{\hat{\rho}^* \bar{m}_j}{\bar{\rho}^2} \frac{\partial}{\partial x_j}\left(\frac{\hat{p}^+}{\bar{\rho}}\right) \cdots \\
&\cdots + \frac{\hat{T}^+}{\bar{\rho}^2}\left(\bar{m}_j \frac{\partial \hat{T}^*}{\partial x_j} + \frac{2\hat{\rho}^* \bar{m}_j}{\bar{\rho}^2} \frac{\partial \bar{T}}{\partial x_j}\right) + \frac{\hat{Z}^+}{\bar{\rho}^2}\left(\bar{m}_j \frac{\partial \hat{Z}^*}{\partial x_j} + \frac{2\hat{\rho}^* \bar{m}_j}{\bar{\rho}^2} \frac{\partial \bar{Z}}{\partial x_j}\right) \qquad (4.8)
\end{aligned}$$

The contributions of the advection terms to the change in the eigenvalue are

$$\delta\lambda_{Adv} = \langle \bar{f}^+_{x,Adv}, \delta\bar{m}_x \rangle + \langle \bar{f}^+_{r,Adv}, \delta\bar{m}_r \rangle + \langle \bar{\psi}^+_{Z,Adv}, \delta\bar{Z} \rangle + \bar{\psi}^+_{T,Adv}, \delta\bar{T} \rangle + \langle \bar{\varrho}^+_{Adv}, \delta\bar{\rho} \rangle \qquad (4.9)$$

The sensitivity of the production terms to base flow modifications is the difference between the total sensitivity and the sensitivity of the advection terms, $\bar{\mathbf{g}}^+_{Prod} = \bar{\mathbf{g}}^+ - \bar{\mathbf{g}}^+_{Adv}$. In the following sections, these are compared in order to determine the mechanisms that most change the eigenvalue.

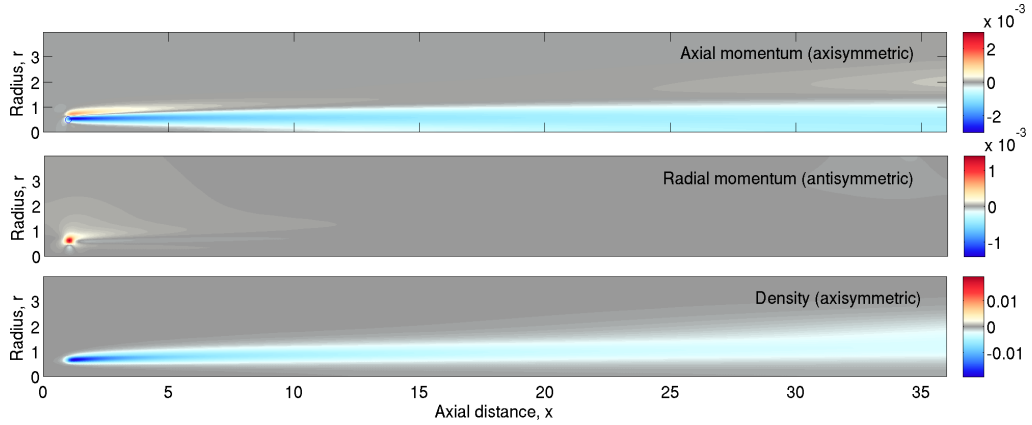

Figure 4.6: The change in the steady base flow caused by a steady drag force $\bar{f}_x = -0.01e^{-100\left((x-1.0)^2+(r-0.5)^2\right)}$.

$\times 10^2$	Advection	Production	Total
$\delta\lambda_{\bar{m}_x}$	2.46-0.85i	-3.69+0.51i	-1.23-0.34i
$\delta\lambda_{\bar{m}_r}$	0.72-0.62i	-0.20+0.51i	0.52-0.11i
$\delta\lambda_{\bar{Z}}$	-0.11+0.21i	0.07-1.00i	-0.03-0.79i
$\delta\lambda_{\bar{\rho}}$	-4.28+0.63i	2.47-1.57i	-1.81-0.93i
$\delta\lambda_{tot}$	-1.21-0.62i	-1.35-1.55i	-2.56-2.17i

Table 4.1: The contributions to the change in the eigenvalue ($\times 10^2$) due to a steady drag force $\bar{f}_x = -0.01e^{-100\left((x-1.0)^2+(r-0.5)^2\right)}$.

4.6.1 The effect of a drag force in the shear layer

We start by considering the mechanisms through which the drag from the ring affects the growth rate and frequency of the global mode. The radial velocity in the jet is much smaller than the axial velocity so, when the ring is placed in the jet, the axial component of the drag force is several orders of magnitude larger than the radial component. Therefore we consider only the axial component. We add a small force $\bar{f}_x = Ae^{-100\left((x-x_c)^2+(r-r_c)^2\right)}$ to the nonlinear axial momentum equation, with $A = -0.01$ and $(x_c, r_c) = (1.0, 0.5)$, and obtain a new steady base flow. Figure 4.4 shows that this drag force will reduce the growth rate of the global mode. This change in the eigenvalue is caused by a change in the steady base flow. This change in the steady base flow is shown in figure 4.6. The force in the negative x-direction reduces the axial momentum in the jet, causing the low-density jet to diverge. This increases the mixture fraction in the fluid surrounding the jet and therefore reduces the density there.

Table 4.1 shows the contributions of each component to the change in the eigenvalue, from which physical conclusions can be drawn. For example, the drag force causes the x-momentum in the jet to decrease, the effect of which is measured by $\delta\lambda_{\bar{m}_x}$. On the one hand, this tends to decrease $\mathrm{Re}(\lambda)$ through the production terms because the shear is weaker. On the other hand, this tends to increase $\mathrm{Re}(\lambda)$ through the advection terms because the perturbations are advected downstream less quickly. Table 4.1 shows that the former outweighs the latter, so the net effect of the decreased jet velocity is stabilizing. As another example, the low density jet expands more rapidly, which reduces the density in the surrounding flow, making it more similar to that of the jet. On the one hand, this tends to increase $\mathrm{Re}(\lambda)$ through the production terms. On the other hand, this tends to decrease $\mathrm{Re}(\lambda)$ through the advection terms because the outer flow, which is slow, has less influence on the perturbation advection speed when its density reduces. The latter outweighs the former so the net effect of the lower density outside the jet is stabilizing. Although this is unlikely to be a general result for all drag

$\times 10^3$	Advection	Production	Total
$\delta\lambda_{\bar{m}_x}$	-1.00-1.23i	1.83+3.01i	0.83-4.23i
$\delta\lambda_{\bar{m}_r}$	1.93+0.18i	-1.39-0.32i	0.54-0.15i
$\delta\lambda_{\bar{Z}}$	-0.26-0.01i	2.21-0.05i	1.95-0.06i
$\delta\lambda_{\bar{T}}$	0.10+0.09i	-0.10+0.31i	0.00+0.40i
$\delta\lambda_{\bar{\rho}}$	-11.3-6.15i	10.6+2.10i	-0.64-4.04i
$\delta\lambda_{tot}$	-10.5-7.12i	13.2+5.05i	2.68-8.08i

Table 4.2: The contributions to the change in the eigenvalue ($\times 10^3$) due to a steady heat source $\bar{\psi}_T = 0.01e^{-100\left((x-0.5)^2+(r-0.25)^2\right)}$.

forces, this demonstrates how this technique can shed light on the physical mechanisms behind the influence of a given drag force at a given position.

4.6.2 The effect of a heat source in the jet core

We now consider how a heat source in the jet core affects the growth rate and frequency of the global mode. We add a Gaussian source term $\bar{\psi}_T(x,r) = 0.01e^{-100\left((x-0.5)^2+(r-0.25)^2\right)}$ to the energy equation. Figure 4.3 shows that this heat source will increase the growth rate of the global mode. The sensitivity of the base flow at this location is less than at the location where the drag force was applied in the previous section. The change in the eigenvalue will thus be less than the change caused by the drag force in the previous section. The change in the steady base flow caused by this heat source is shown in figure 4.7.

Table 4.2 shows the contributions of each component to the change in the eigenvalue. Unsurprisingly, the advection and production terms are influenced mostly by the change in the density profile ($\delta\lambda_{\bar{\rho}}$), through the same mechanisms as before. This time, however, the increase in Re(λ) due to the production terms is almost exactly balanced by the decrease in Re(λ) due to the advection terms. Again, this is unlikely to be a general result for all heat sources, but it shows how the technique can be used to investigate the physical mechanisms behind the influence of a heat source at a given position.

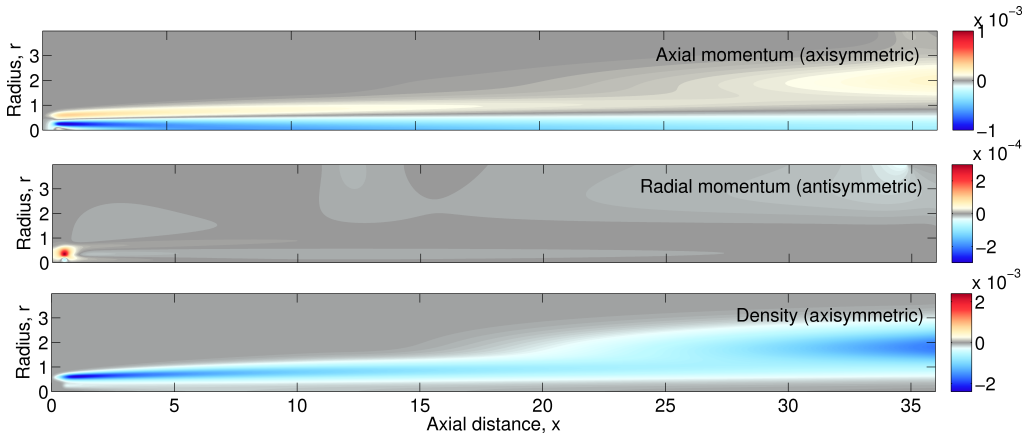

Figure 4.7: The change in the steady base flow caused by a steady heat source $\bar{\psi}_T = 0.01e^{-100\left((x-0.5)^2+(r-0.25)^2\right)}$.

4.7 Summary

In this chapter we have performed a structural sensitivity analysis and a base flow sensitivity analysis of the stability of a low-density jet. We have used direct numerical simulations of the direct and adjoint low Mach number Navier–Stokes equations: in nonlinear form to find the steady base flow, and linear form to simulate the evolution of infinitesimal perturbations. With an Arnoldi algorithm, we have calculated the direct and adjoint global modes for the structural sensitivity analysis and have combined this with a Lagrangian approach for the base flow sensitivity analysis. We have produced maps of the regions of the flow that are most sensitive to localized closed loop feedback, and localized open loop steady forcing. This forcing can take the form of a body force, a mass source, and a heat source.

We have found that the maximum of the structural sensitivity, which is sometimes known as the wavemaker region, lies in the shear layer 2.66 jet diameters downstream of the exit plane. This flow is locally absolutely unstable from the exit plane to 5 jet diameters downstream and has maximum absolute growth rate at the exit plane. In a local analysis of this flow (Monkewitz *et al.*, 1993), the wavemaker region would be taken to be at the exit plane, highlighting a significant difference between the local and global

approaches. Our global analysis shows that the most sensitive location for open loop steady forcing is the area around the shear layer, around 2 jet diameters downstream of the exit plane. This forcing can change the growth rate and frequency of the primary global mode. We find that the influence of steady forcing and heat injection is advected by the flow outside the jet. As a word of caution, this means that these results depend on the streamlines around the jet, which are very sensitive to the degree of co-flow.

We have used these maps to calculate the influence of a ring placed in the flow. When the ring is at the same temperature as the flow, it influences the flow only through its drag. In this case, the influence of the steady component of the drag force far outweighs the influence of the unsteady component. Depending on its axial position, the ring changes the growth rate or frequency of the primary global mode, in a manner that should be possible to measure experimentally. This result depends very little on the streamlines outside the jet because the velocity is small there, so there is little drag. By examining the relative magnitudes of the advection and production terms in the governing equations when the ring is placed at a point where it stabilizes the flow, we find that the changes induced in the axial momentum and mean density fields have most influence on the eigenvalue. We propose mechanisms in this particular case but note that these mechanisms will depend on the ring's position.

When the ring is hotter than the flow, it also influences the flow through heat input. Again, the influence of the steady component far outweighs the influence of the unsteady component. The hot ring has most influence when placed in the outer edge of the shear layer. It is also influential when placed outside the jet because the expanded gas is advected towards the jet. In the slow-moving outer flow, heat transfer from the ring is more influential than drag from the ring because heat transfer depends less strongly on the local velocity than the drag does. Again, this should be possible to measure experimentally, although when the ring is placed outside the jet, its predicted influence depends significantly on the streamlines, which may be difficult to

replicate in an experiment. For the hot ring, as for the adiabatic ring, we find that the changes induced in the axial momentum and mean density fields have the most influence on the eigenvalue.

This study provides a basis for hypotheses that can be tested through an experimental study of the passive control of a low density jet with an adiabatic ring and a hot ring. In these experiments, changes in the frequency will probably be easier to measure than changes in the growth rate, so it is pleasing to see in figures 3 and 4 that a ring should affect the frequency as much as the growth rate. This study is also a stepping stone for the theoretical study of hydrodynamic stability of jet diffusion flames, for which extensive experimental work has already been done in our research group by Li & Juniper (2012).

4.8 Appendix

In this section, we validate our sensitivity maps and check whether the predicted changes in the eigenvalue are the same as those found by numerical simulation.

First, we validate the sensitivity to arbitrary base flow modfications. We add a Gaussian of the form $\delta\bar{m}_x = -Ae^{-100\left((x-1.5)^2+(r-0.25)^2\right)}$ to the base flow axial momentum and calculate the new eigenvalue using our direct eigenvalue solver. We compare the normalized change in the eigenvalue $\delta\lambda_{act}/A$ to the predicted change in the eigenvalue $\delta\lambda_{pred}/A = \langle\bar{f}_x^+, \delta\bar{m}_x\rangle/A$. The results for $A = 0.005, 0.01, 0.05$ are shown in Table 4.3 and show good agreement between the predicted and actual eigenvalues. We notice, however, that even for a small base flow modification, there is a small discrepancy in the frequency. We attribute this to the first-order temporal accuracy of the direct and adjoint timesteppers (Chandler *et al.*, 2012).

Next, we validate the sensitivity to steady forcing. First, we consider the effect of a momentum source term described by $\bar{f}_x = -0.01e^{-100\left((x-1.0)^2+(r-0.5)^2\right)}$.

$\delta\lambda_{pred}$	$A = 0.005$	$A = 0.01$	$A = 0.05$
0.5506-0.4252i	0.5549-0.4358i	0.5543-0.4352i	0.5555-0.4499i

Table 4.3: Comparison between the predicted and actual change in the eigenvalue due to an arbitrary base flow modification of the form $\delta\bar{m}_x = -Ae^{-100\left((x-1.5)^2+(r-0.25)^2\right)}$.

Steady force	$\delta\lambda_{pred,SF}$	$\delta\lambda_{pred,BFM}$	$\delta\lambda_{act}$
$\bar{f}_x = -0.01e^{-100\left((x-1.0)^2+(r-0.5)^2\right)}$	-0.0252-0.0222i	-0.0256-0.0218i	-0.0204-0.0053i
$\bar{\psi}_T = 0.005e^{-100\left((x-0.5)^2+(r-0.25)^2\right)}$	0.0011-0.0046i	0.0013-0.0041i	0.0006-0.0022i
$\bar{\psi}_T = 0.005e^{-100\left((x-2.0)^2+(r-0.25)^2\right)}$	-0.0050-0.0011i	-0.0039-0.0010i	-0.0022-0.0004i

Table 4.4: Comparison between the predicted and actual change in the eigenvalue due to a steady force. We compare the actual change in the eigenvalue ($\delta\lambda_{act}$) with the change predicted using the sensitivity to steady forcing ($\delta\lambda_{pred,SF}$) and the change predicted using the sensitivity to base flow modifications with the forced base flow ($\delta\lambda_{pred,BFM}$)

The change in the eigenvalue due to this steady forcing can be calculated in three ways. Firstly, we predict the change in the eigenvalue using the sensitivity to steady forcing framework, $\delta\lambda_{pred,SF} = \langle\bar{m}_x^+, \delta\bar{f}_x\rangle$. Secondly, we add the forcing term to the RHS of the NS equations and obtain a new steady base flow, $\bar{q} + \delta\bar{q}$. The change in the eigenvalue can then be predicted using the sensitivity to base flow modifications, $\delta\lambda_{pred,BFM} = \langle\bar{\mathbf{g}}^+, \delta\bar{q}\rangle$. Thirdly, the new eigenvalue can be calculated using the direct eigenvalue solver on the new steady base flow. In the linear approximation, all three methods should give the same answer. We also test two heat sources described by $\bar{\psi}_T = 0.01e^{-100\left((x-0.5)^2+(r-0.25)^2\right)}$ and $\bar{\psi}_T = 0.01e^{-100\left((x-2.0)^2+(r-0.25)^2\right)}$. The results are shown in Table 4.4. The predicted change in the eigenvalue using the sensitivity to steady forcing and base flow modifications agree reasonably well. The actual change in the eigenvalue calculated using the direct eigenvalue solver is less than the predictions.

To investigate this further, we test the effect of a drag force $\bar{f}_x = \cdots$

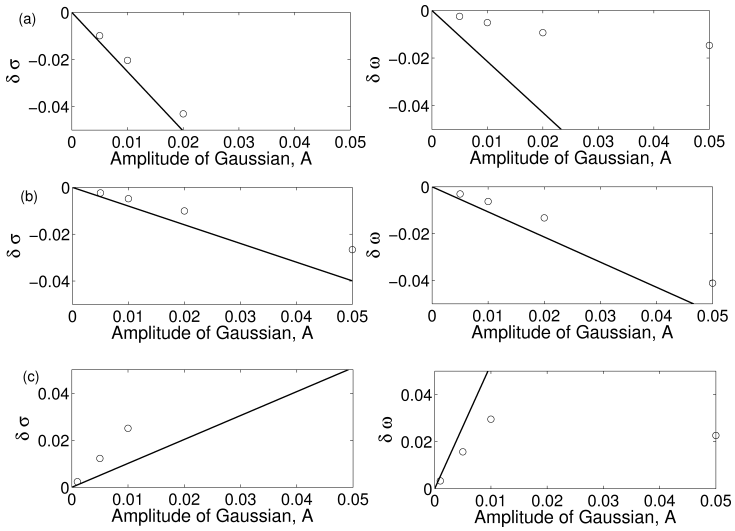

Figure 4.8: Comparison of predicted and actual change in growth rate and frequency due to a drag force $\bar{f}_x = -Ae^{-100\left((x-x_c)^2+(r-r_c)^2\right)}$ for varying A, at three locations, (x_c, r_c): (a) $L1 \equiv (1.0, 0.5)$ (top), (b) $L2 \equiv (1.5, 0.25)$ (middle), and (c) $L3 \equiv (1.87, 0.67)$(bottom). The solid line shows the predicted change using the sensitivity to steady forcing ($\delta\lambda_{pred,SF}$), and the circles show the actual change in the eigenvalue ($\delta\lambda_{act}$), calculated using the the direct eigenvalue solver on the modified steady base flow.

$-Ae^{-100\left((x-x_c)^2+(r-r_c)^2\right)}$ for a range of amplitudes A at three different locations, $L1 \equiv (1.0, 0.5)$, $L2 \equiv (1.5, 0.25)$ and $L3 \equiv (1.87, 0.67)$. We compare the predicted change using the sensitivity to steady forcing with the actual change calculated using the direct eigenvalue solver. The results are shown in figure 4.8. At all the locations, we find that the sensitivity to steady forcing predicts the sign of the change correctly, but the magnitude of the change is not predicted well for increasing amplitudes. At $L1$, we find that the agreement in the growth rate is good but the agreement in the frequency is poor. This is because $L1$ lies in a region where the real part of $\bar{\mathbf{m}}_x^+$ has a large magnitude and its imaginary part is changing sign. At $L3$, we find that the agreement in the frequency is good but the agreement in the growth rate is poor. This is because $L3$ lies in a region where the imaginary part of $\bar{\mathbf{m}}_x^+$ has a large magnitude and its real part is changing sign. At $L2$, the phase of $\bar{\mathbf{m}}_x^+$ is almost $\pi/4$, and we find that the agreement in both the growth rate and frequency is similar. In general, the results show that the sensitivity to steady forcing is somewhat inaccurate in predicting the magnitude of the change in the eigenvalue. One cause of this discrepancy may be the continuous adjoint formulation, which is not a perfect adjoint to the direct equations.

5

Spiral vortex breakdown: its physical origin and control

This chapter is devoted to studying the structural sensitivity and passive control of spiral vortex breakdown in a uniform-density swirling flow. The flow profile used has been studied extensively in previous studies. This allows the techniques described in Chapters 2 and 3 to be validated for a swirling flow.

The global stability and structural sensitivity results for $m = -1$ in this chapter have been published as a journal article in the Journal of Fluid Mechanics (Qadri *et al.*, 2013), co-authored with Dhiren Mistry and Matthew Juniper . The local stability analysis was done by Dhiren Mistry and Matthew Juniper. The sensitivity to a control force for $m = -1$ has been presented at the UKACC Conference 2012 (Qadri & Juniper, 2012), co-authored with Matthew Juniper.

5.1 Introduction

If a jet of fluid rotates with sufficient azimuthal velocity (swirl), a stagnation point and a recirculation bubble form within it, around one or two jet

diameters downstream from the start of the jet. In this thesis, the transition from the flow without a breakdown bubble to the flow with a breakdown bubble is labelled *axisymmetric* vortex breakdown. Furthermore, in some conditions the steady flow around this vortex breakdown bubble is unstable to helical or double-helical perturbations. In this study, the development of these helical or double-helical perturbations on top of the vortex breakdown bubble is labelled *spiral* vortex breakdown.

Vortex breakdown was first observed in the flow over a gothic wing at high angles of attack by Peckham & Atkinson (1957). The spiral mode was first identified by Lambourne & Bryer (1961) in the flow over delta wings. Since then, several different forms of vortex breakdown have been observed in a variety of experimental settings such as tubes, nozzles and combustion chambers. Investigators often observed the axisymmetric and spiral modes of breakdown to occur almost simultaneously. Some saw spiral breakdown before axisymmetric breakdown, while others saw axisymmetric breakdown before spiral breakdown. This led to disagreements over the nature of vortex breakdown (see reviews by Escudier, 1988; Hall, 1972; Leibovich, 1978; Lucca-Negro & O'Doherty, 2001).

Two main explanations have been proposed for vortex breakdown: hydrodynamic instability (Ludwieg, 1960) and a supercritical to subcritical transition (Benjamin, 1962). Experimental evidence reviewed by Escudier (1988) indicates that the flow upstream of the breakdown bubble is marginally stable or completely stable. Together with the fact that the onset of vortex breakdown is sudden, this suggests that hydrodynamic instability is not responsible for causing axisymmetric vortex breakdown. Benjamin (1962) compared vortex breakdown to the hydraulic jump seen in channel flows. He proposed the idea of vortex breakdown being a transition from a super-critical flow configuration to a sub-critical flow configuration and derived a criterion for vortex breakdown.

Numerical studies allow vortex breakdown to be studied in a more con-

trolled manner. Grabowski & Berger (1976) observed axisymmetric breakdown bubbles in their steady incompressible simulations and tried, unsuccessfully, to apply Benjamin's criticality criterion to these flows. Over the next 20 years, increased computing power led to a large number of numerical studies in which vortex breakdown was simulated in a variety of domains (Spall & Snyder, 1999). More recently, Ruith, Chen, Meiburg & Maxworthy (2003) carried out both steady axisymmetric and unsteady three-dimensional direct numerical simulations of vortex breakdown using the inlet flow profile defined by Grabowski & Berger (1976), which is labelled the *Grabowski* profile. They used constant inlet conditions and open lateral boundary conditions. They showed that Benjamin's criticality criterion works when applied locally to the flow profiles upstream of breakdown. Following this, Vyazmina, Nichols, Chomaz & Schmid (2009) studied the bifurcation sequence of axisymmetric vortex breakdown using the Grabowski inlet profile. Apart from noting that axisymmetric vortex breakdown is a robust transition phenomenon from one steady state to another, we do not investigate it further here.

Ruith *et al.* (2003) considered the local absolute/convective stability (Huerre & Monkewitz, 1990) of the flow field created by the axisymmetric vortex breakdown. By comparing the flow profiles to those of a Batchelor vortex, they concluded that spiral breakdown is caused by a sufficiently large pocket of absolute instability in the wake of the axisymmetric breakdown bubble. They also obtained eigenfunctions corresponding to a helical (with azimuthal wavenumber $m = -1$) and double helical breakdown mode ($m = -2$). The minus sign indicates that the spiral winds in the opposite direction to the swirl.

Gallaire, Ruith, Meiburg, Chomaz & Huerre (2006) performed a local stability analysis of the flow fields obtained by Ruith *et al.* (2003) using linear direct numerical simulations (lDNS). For a particular swirl parameter, they found two regions of absolute instability, one centred on the bubble and one centred on the wake that develops behind it. By using the frequency selection criterion of Pier, Huerre & Chomaz (2001) and by comparing the spatial

growth rate obtained from the local analysis with amplitudes extracted from Ruith's DNS results, they interpreted spiral vortex breakdown as a nonlinear global mode that arises from the region of absolute instability in the wake of the bubble. In a similar study, Herrada & Fernandez-Feria (2006) used DNS and a local stability analysis to investigate the spiral modes of vortex breakdown in a swirling flow in a pipe using the Batchelor vortex profile. In contrast to Gallaire *et al.* (2006), they found that the helical mode arises due to a region of local absolute instability in the bubble.

Meliga & Gallaire (2011) performed a linear global stability analysis around the vortex breakdown bubble and its wake using the Grabowski profile. They confirmed that spiral vortex breakdown is caused by an unstable eigenmode. The growth rate and frequency from their global stability analysis agreed well with the growth rate seen in Ruith's DNS. Recently, these researchers have extended their analysis to consider weakly nonlinear mechanisms that are responsible for competition between the helical and double helical breakdown modes in the Grabowski family of flows (Meliga, Gallaire & Chomaz, 2012*a*).

In this chapter, we investigate spiral vortex breakdown in laminar, incompressible flows by performing linear global stability analyses around the vortex breakdown bubble and its wake. In contrast to Meliga & Gallaire (2011) and Meliga *et al.* (2012*a*), our aim is to determine the regions that are most influential in causing spiral breakdown as observed in the simulations of Ruith *et al.* (2003) and to identify the physical mechanisms that are responsible for causing it.

For this purpose, we use the linear direct and adjoint global modes to obtain the structural sensitivity of the flow (Giannetti & Luchini, 2007; Hill, 1992). This provides a two-dimensional map of the wavemaker region of the flow, showing the regions of the flow in which force-momentum feedback has most influence on the frequency and growth rate of the mode. We also perform a local stability analysis, which allows us to work out which regions

of the flow are absolutely unstable and extract local spatial growth rates of perturbations, given the frequency of the global mode. This is a useful diagnostic tool, particularly in identifying the wavefront of the nonlinear global mode. We compare our results with those of Ruith *et al.* (2003) and Gallaire *et al.* (2006) and, although we agree with Gallaire *et al.* (2006) that the nonlinear behaviour is governed by the wake, we discover that the linear behaviour is governed by the bubble for moderate swirls.

This study is at $Re = 200$ and the primary motivation is scientific. There are important industrial motivations, however. Vortex breakdown occurs in wingtip vortices behind aircraft, in vacuum cleaners, and in gas turbine combustion chambers. In the case of combustion chambers, hydrodynamic instabilities in the flow can lock into acoustic resonances within the combustion chamber, causing high amplitude thermoacoustic instabilities, which can be catastropic. This fundamental study of spiral vortex breakdown will reveal the regions of the flow that are responsible for these hydrodynamic instabilities and could help designers to control them, either actively or passively.

5.2 Flow configuration

We study the motion of a fluid of uniform density in a cylindrical domain of length X_{max} and radius R_{max}. On Ω_{in}, we impose the density and velocity profiles used by Grabowski & Berger (1976) and subsequently by Ruith *et al.* (2003). This Grabowski profile has uniform density, ρ_1, uniform temperature, T_1, and uniform axial velocity, U_1, beyond a characteristic radius R. Using these quantities as reference scales, the nondimensional base flow inlet profile

is

$$\begin{aligned}
\bar{\rho}(0,r) &= 1, && (5.1a)\\
\bar{T}(0,r) &= 0, && (5.1b)\\
\bar{u}_x(0, 0 \le r \le 1) &= \alpha + (1-\alpha)\left(6 - 8r + 3r^2\right) r^2, && (5.1c)\\
\bar{u}_x(0, r > 1) &= 1, && (5.1d)\\
\bar{u}_r(0,r) &= 0, && (5.1e)\\
\bar{u}_\theta(0, 0 \le r \le 1) &= r\left(2 - r^2\right) Sw, && (5.1f)\\
\bar{u}_\theta(0, r > 1) &= Sw/r, && (5.1g)
\end{aligned}$$

where Sw is a nondimensional swirl parameter and α is a nondimensional coflow parameter. In this study, which is at $Re = 200$, we keep $\alpha = 1$, which corresponds to a uniform axial velocity. In the past, the use of constant inlet conditions for simulating vortex breakdown has been criticized. However, Ruith *et al.* (2003) showed that this is a safe assumption as long as the inlet is super-critical, which is true for all the inlet profiles that we consider.

On the lateral and outlet boundaries, we impose boundary conditions that model flow into a semi-infinite domain in the downstream and radial directions.

The steady axisymmetric base flow is obtained by marching the equations forward in time, while constraining the flow variables to be axisymmetric at each timestep. This works because the base flow is stable to axisymmetric perturbations.

5.3 Validation

Figure 5.1 shows the steady base flow at $Sw = 1.0$. There is an axisymmetric breakdown bubble around $x = 2$, which creates a wake downstream. The streamline pattern and the size and location of the bubble match that obtained in previous axisymmetric simulations (Grabowski & Berger, 1976;

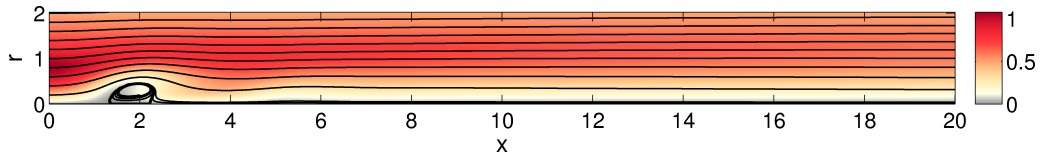

Figure 5.1: Nondimensional base flow for $Sw = 1.0$, calculated with mesh M_1. The streamlines represent the axial and radial velocities. The shading (colour online) represents the azimuthal velocity.

Meliga & Gallaire, 2011; Ruith *et al.*, 2003). For this reference case, we calculate the base flow and linear global stability on three different meshes in order to assess the reliability and convergence of the results. The linear global stability analysis predicts one unstable eigenmode for $m = -1$ and no unstable eigenmodes for $m \neq -1$. Table 5.1 compares the unstable global mode frequency obtained using these meshes with results from Ruith *et al.* (2003), Gallaire *et al.* (2006) and Meliga & Gallaire (2011). The eigenvalue depends very weakly on the grid resolution and spatial domain size and we conclude that mesh M_1 is sufficient for this study.

Ruith *et al.* (2003) performed fully three-dimensional nonlinear DNS. They perturbed the axisymmetric steady state solution with white noise and then extracted the linear growth rate and frequency from the initial rate of increase of the kinetic energy per unit mass. Our eigenvalue is within 1.3% of theirs. Gallaire *et al.* (2006) carried out a local stability analysis on the same axisymmetric steady state solution and used the frequency selection criterion of Pier *et al.* (2001) to predict the frequency of the nonlinear global mode. This is not expected to be exactly the same as the linear global mode but, nonetheless, is also close to our calculations. Meliga & Gallaire (2011) used a finite-element solver to obtain the base flow and global mode in a domain that was twice as long (axially) as that used in this study and by Ruith *et al.* (2003). As the domain length increases, the convective non-normality of the linearized N–S operator also increases. This makes the eigenvalues more sensitive to perturbations and this could be the reason for the slight discrepancy between our results and theirs.

	X_{max}	R_{max}	S_x	S_r	Growth rate σ	Frequency ω
M_1	20.0	8.0	513	127	0.035214	1.165476
M_2	20.0	8.0	257	127	0.035177	1.165453
M_3	25.4	10.4	257	127	0.034348	1.162470
NL DNS	20.0	10.0	193	61	0.0359	1.18
Local NL	-	-	-	-	-	1.22
L global	40.0	6.0	-	-	0.0335	1.17

Table 5.1: Domain size (X_{max}, R_{max}) and number of gridpoints (S_x, S_r) of the three meshes ($M_1 - M_3$) used in this study, and those used by Ruith *et al.* (2003) (nonlinear (NL) DNS), Gallaire *et al.* (2006) (local nonlinear (NL) analysis) and Meliga & Gallaire (2011) (linear global stability). Growth rate, σ, and frequency, ω, of the unstable $m = -1$ mode in each study.

Table 5.2 compares the linear growth rates obtained from mesh M_1 with those in table 1 of Meliga & Gallaire (2011) and those in figure 28 of Ruith *et al.* (2003), for three swirls and two azimuthal wavenumbers, m. As discussed earlier, the difference between Meliga's growth rates and ours can be attributed to the difference in domain lengths. Ruith *et al.*'s extraction of the linear growth rate from the rate of growth of white noise works well near the point of linear stability, which is at $Sw = 0.915$, because only the $m = -1$ mode is unstable and this mode grows relatively slowly. It becomes less accurate as the swirl increases, however, because the $m = -2$ mode also becomes unstable. The evolution therefore depends on how the initial white noise projects onto each of the modes and it is harder to distinguish between the growth rates of each individual mode. This could explain why Ruith *et al.*'s growth rates at $Sw = 1.2$ and $Sw = 1.3$ are slightly different to ours. We conclude that the agreement is as good as can be expected.

In the absence of truncation errors, the adjoint eigenvalues would be the complex conjugates of the direct eigenvalues. In this study, the adjoint equations are derived algebraically from the direct equations and then discretized, which means that the truncation errors of the adjoint algorithm differ from those of the direct algorithm. We must check, therefore, that the adjoint

Swirl	1.0	1.2	1.2	1.3	1.3
m	-1	-1	-2	-1	-2
σ from M_1	0.0352	0.114	0.0249	0.123	0.0693
σ from Ruith *et al.*	0.0359	0.106	0.0331	0.110	0.0674
σ from Meliga & Gallaire	0.0335	0.118	0.0264	0.125	0.0729

Table 5.2: Comparison of most unstable linear growth rates from a global stability analysis with growth rates observed in 3D DNS. The growth rates have been obtained from figure 28 of Ruith *et al.* (2003) and table 1 of Meliga & Gallaire (2011) .

	Growth rate σ	Frequency ω	Abs. discrepancy	Rel. discrepancy (%)
M_1	0.037663	-1.165434	0.002449	0.210064
M_2	0.037048	-1.165592	0.001876	0.160908
M_3	0.038603	-1.161601	0.004343	0.373424

Table 5.3: The most unstable adjoint eigenvalue for $m = -1$ and the discrepancy with respect to the complex conjugate of the direct eigenvalue, for meshes $M_1 - M_3$. The discrepancy is abs$(\lambda_{adj} - \lambda^*_{dir})$ where $\lambda \equiv \sigma + \mathrm{i}\omega$.

eigenvalues are close to the complex conjugate of the direct eigenvalues. Table 5.3 shows the adjoint eigenvalues and the discrepancy with the direct eigenvalues for the three meshes. This discrepancy is due to the first order time accuracy of the numerical scheme and decreases as the timestep decreases (Chandler *et al.*, 2012). The discrepancy for mesh M_1 is 0.2%, which is sufficiently small for us to be confident that the adjoint eigenmodes are close to correct.

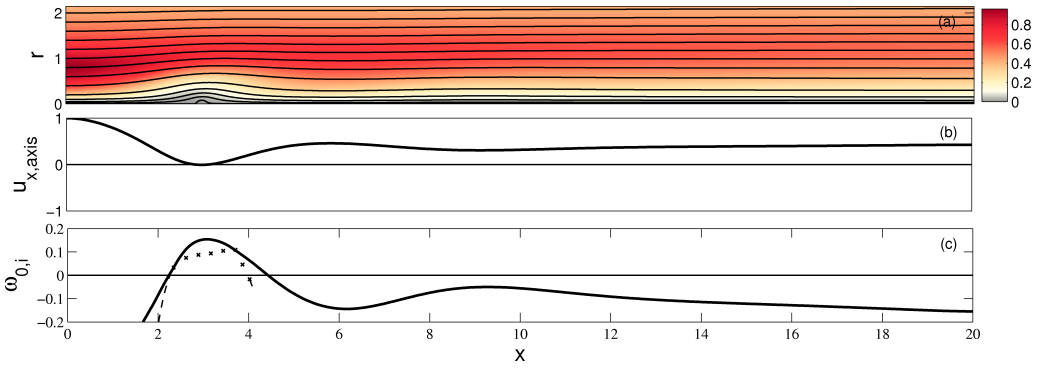

Figure 5.2: (a) Baseflow at $Sw = 0.8944$ and $Re = 200$, (b) axial velocity along the axis, $r = 0$, (c) absolute growth rate of the dominant saddle point (solid line) and the next saddle point (shown by a dashed line where it is a valid pinch point and by crosses where it is not).

5.4 Global stability and structural sensitivity

5.4.1 Helical mode, $m = -1$

5.4.1.1 Onset of instability

In this study, we increase the swirl from $Sw = 0.8$, which is stable and before the onset of vortex breakdown. At $Sw = 0.8944$, a stagnation point forms on the centreline, which is the first sign of an axisymmetric breakdown bubble; figure 5.2. This agrees with the results of Ruith *et al.* (2003). The complex absolute growth rate, ω_{0i}, is obtained as a function of streamwise distance, x, using the local analysis. This reveals that a region of absolute instability (which also exists for lower values of swirl) is centred around the bubble. The flow is globally stable, however, for all azimuthal wavenumbers, showing that this region of absolute instability is not large enough or strong enough to cause a global instability.

As the swirl is increased, an unstable mode ($\sigma > 0$) first appears at $Sw = 0.915$ with $m = -1$. Figure 5.3 shows the eigenvalue spectrum for this flow configuration. Figure 5.4 shows the base flow at this swirl together with the absolute growth rate, the unstable direct mode, the corresponding

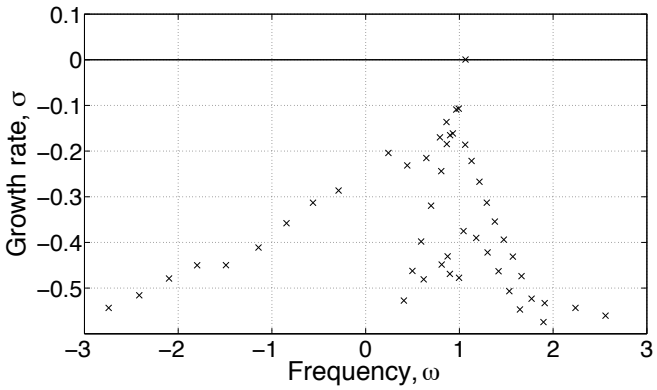

Figure 5.3: Eigenvalue spectrum for $|m| = 1$ for the base flow at $Sw = 0.915$ and $Re = 200$. The 50 least stable modes are shown. Modes with $\omega < 0$ correspond to $m = +1$, while modes with $\omega > 0$ correspond to $m = -1$.

adjoint mode, and the structural sensitivity map. For the direct and adjoint modes, the upper frame shows contours of the positive (solid) and negative (dotted) real parts of the azimuthal vorticity. (The imaginary parts have a similar structure but are a quarter wavelength out of phase.) The lower frame shows the kinetic energy, $E_k(x) = \int_0^{R_{max}} |\mathbf{u}|^2 r dr$ as a function of streamwise distance, and the contributions from the axial, radial, and azimuthal components. This is a convenient measure of the amplitude of the global mode.

At $Sw = 0.915$, the region of absolute instability around the breakdown bubble is sufficiently large to cause a global instability. The direct global mode starts to grow in the bubble region and is amplified further in the wake region, reaching a maximum around $x = 12$. It is worth noting that the wake region is convectively unstable, but not absolutely unstable. The adjoint global mode represents the receptivity of the direct mode to external forcing, or equivalently, the initial condition that most optimally excites the direct mode (Chomaz, 2005). It is localized between the inlet and the upstream edge of the bubble. The spatial separation of the direct and adjoint global modes is characteristic of flows with convective non-normality (Chomaz, 2005). For both the direct and adjoint global modes, the three velocity components have roughly the same order of magnitude, indicating

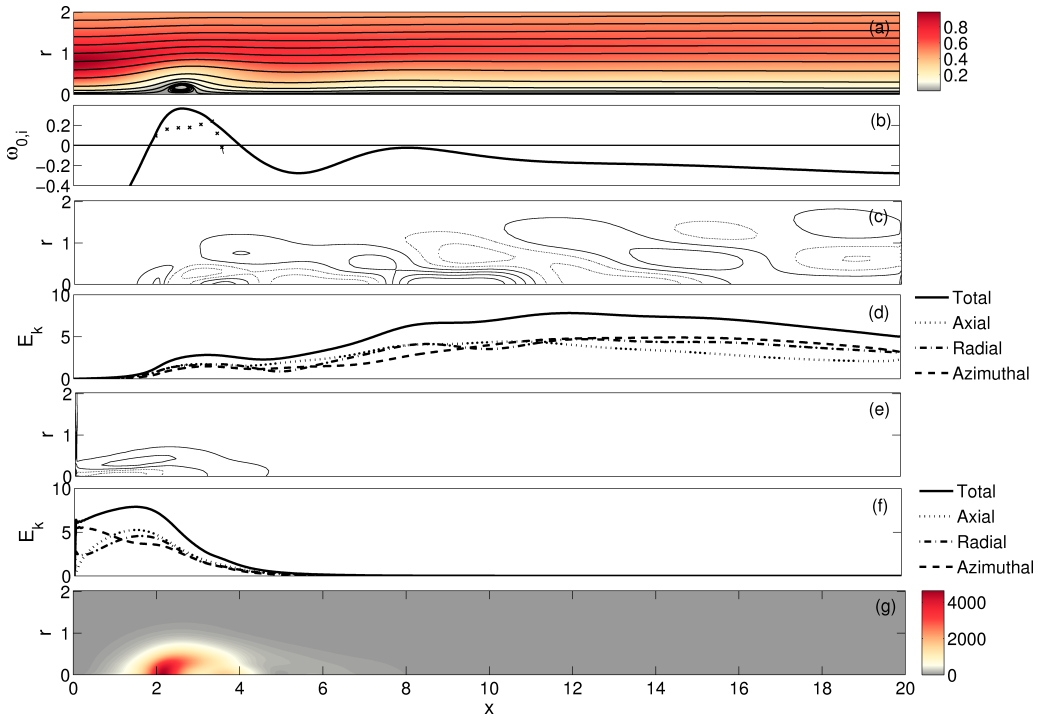

Figure 5.4: (a) Base flow at $Sw = 0.915$ and $Re = 200$; (b) absolute growth rate for $m = -1$; (c) azimuthal vorticity contours of the most unstable direct global mode (solid lines are positive values and dotted lines are negative values); (d) kinetic energy of this direct global mode, separated into the different velocity components; (e) azimuthal vorticity contours of the most unstable adjoint global mode; (f) kinetic energy of this adjoint global mode, separated into the different velocity components; (g) structural sensitivity map as defined by (2.24).

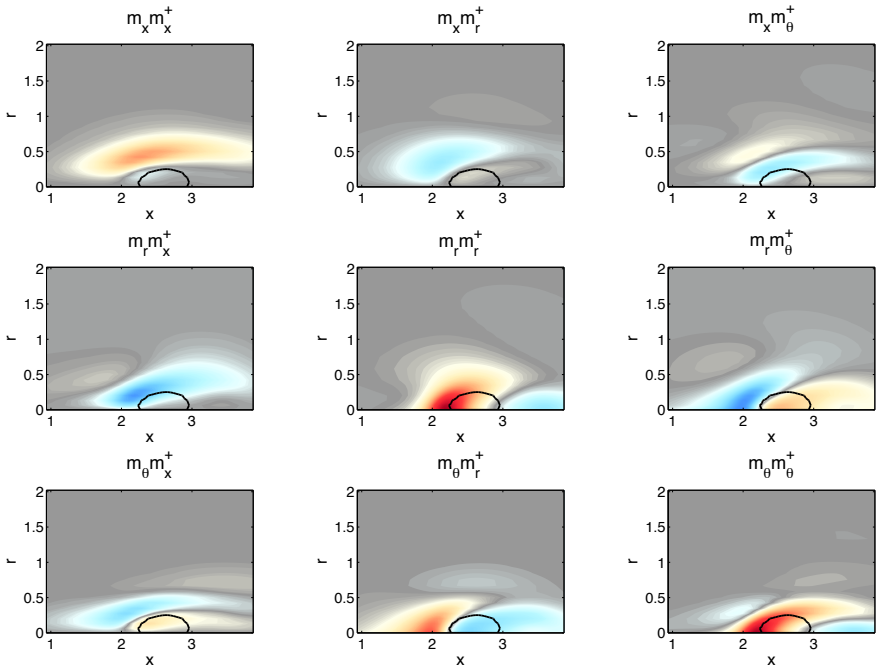

Figure 5.5: The real part (growth rate) of the components of the sensitivity tensor $S_{ij} = \hat{\mathbf{m}}_i(\hat{\mathbf{m}}_j^+)^*$ for the $m = -1$ mode at $Sw = 0.915$. The shading on all the plots scales from -2256 (blue) to 2256 (red). The thick black line shows the breakdown bubble.

that component-wise non-normality is not influential. If it were influential, one would expect different velocity components to dominate in the direct and adjoint global modes. The structural sensitivity map shows that the wavemaker region, as defined in (2.24), is located just upstream of the breakdown bubble, in the region of absolute instability.

5.4.1.2 Mechanisms of instability

In order to understand the physical mechanism by which a small perturbation to the linear operator affects the global mode, we consider the real and imaginary parts of the nine components of the structural sensitivity tensor, shown in Figures 5.5 and 5.6. The nine components quantify the sensitivity of the eigenvalue to changes in the feedback between the three components of the

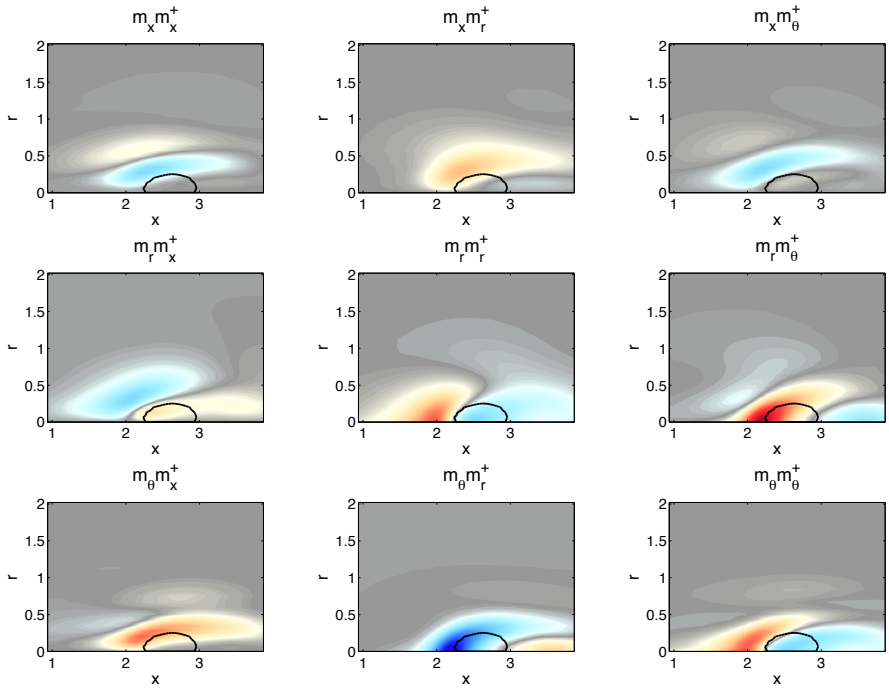

Figure 5.6: The imaginary part (frequency) of the components of the sensitivity tensor $S_{ij} = \hat{\mathbf{m}}_i(\hat{\mathbf{m}}_j^+)^*$ for the $m = -1$ mode at $Sw = 0.915$. The shading on all the plots scales from -2256 (blue) to 2256 (red). The thick black line shows the breakdown bubble.

perturbation momentum vector and the three components of the linearized momentum equations. The real part describes the sensitivity of the growth rate, while the imaginary part describes the sensitivity of the frequency. For example, the figure in the top right corner shows the effect of changing the amount of feedback from the streamwise momentum (m_x) to the azimuthal momentum equation (m_θ).

It can be seen that these sensitivities are in spatial quadrature: the imaginary component is large where the real component is zero, and vice-versa. These oscillatory sensitivity patterns are characteristic of convective flows and are caused by constructive or destructive interference (Tammisola, 2012). The global mode arises due to contributions from feedback throughout the wavemaker region. These contributions interact constructively and destructively to give, in aggregate, a global mode frequency and growth rate. If the feedback at one point in this wavemaker region changes, then the effect on the global mode will depend on the amplitude and the phase of the feedback from this point, relative to the aggregate feedback from the other points. The phase relationship of the feedback varies in space, so the effect of a small change in the feedback at a point also varies in space.

The phase information is interesting, but a clearer picture of the influences of feedback between the components is given by the absolute value of the structural sensitivity. This is shown in figure 5.7. In order to understand the physical mechanisms that may be responsible for causing the global instability, it is worth comparing this with the nine components of the rate-of-strain tensor of the base flow, $\epsilon_{ij} = \frac{1}{2}\left[\nabla\bar{\mathbf{u}} + (\nabla\bar{\mathbf{u}})^T\right]$, which are shown in figure 5.8. The three frames along the leading diagonal show the axial, radial and azimuthal strain, while the off-diagonal frames show the shear. We will start by considering four features. Firstly, at the entry plane, there is strong shear in the $r-\theta$ component at the edge of the vortex core. Secondly, just outside the edge of the bubble (at $r = 0.5$), there is very strong shear in the $x-r$ component and weak shear in the $r-\theta$ component. Thirdly, the frames in the left column of figure 5.7, which correspond to the influences on

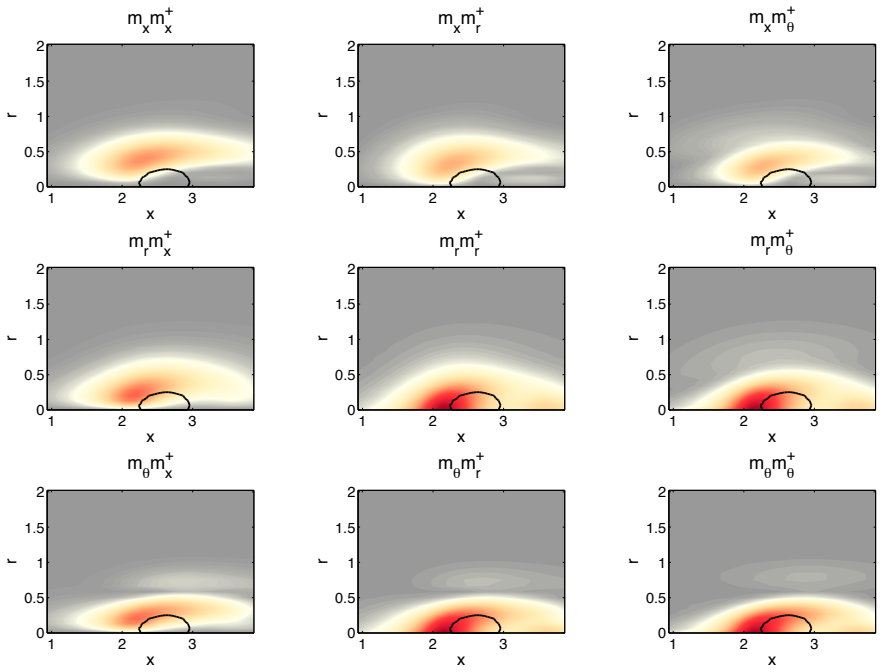

Figure 5.7: The absolute value of the components of the sensitivity tensor $S_{ij} = \hat{\mathbf{m}}_i(\hat{\mathbf{m}}_j^+)^*$ for the $m = -1$ mode of the flow at $Sw = 0.915$. The shading on all the plots scales from 0 (grey) to 2317 (red). The thick black line shows the breakdown bubble.

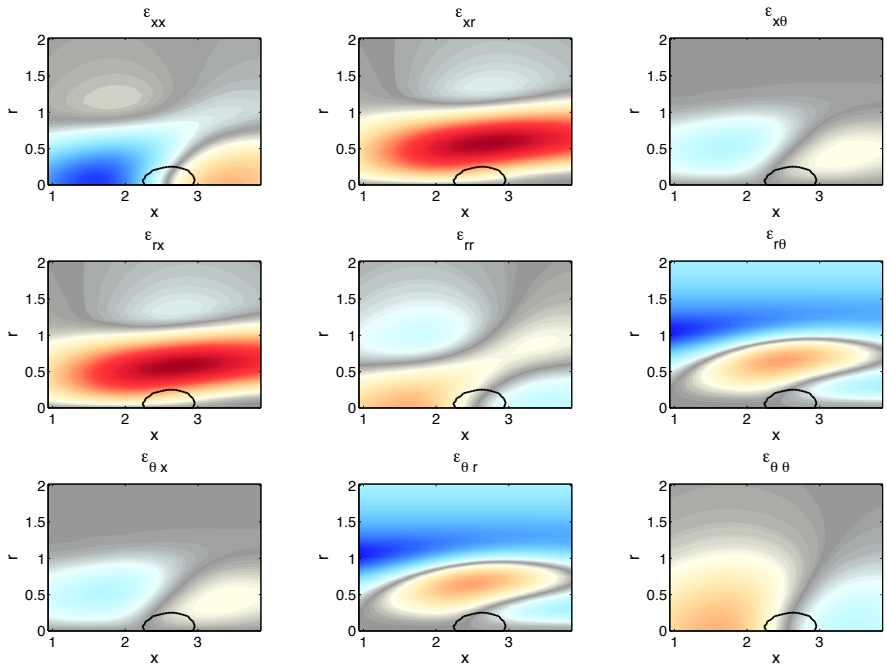

Figure 5.8: The components of the rate-of-strain tensor $\epsilon_{ij} = \frac{1}{2}\left[\nabla\bar{\mathbf{u}} + (\nabla\bar{\mathbf{u}})^T\right]$ for the base flow at $Sw = 0.915$. The shading on all the plots scales from -1.6 (blue) to 1.6 (red). The thick black line shows the breakdown bubble.

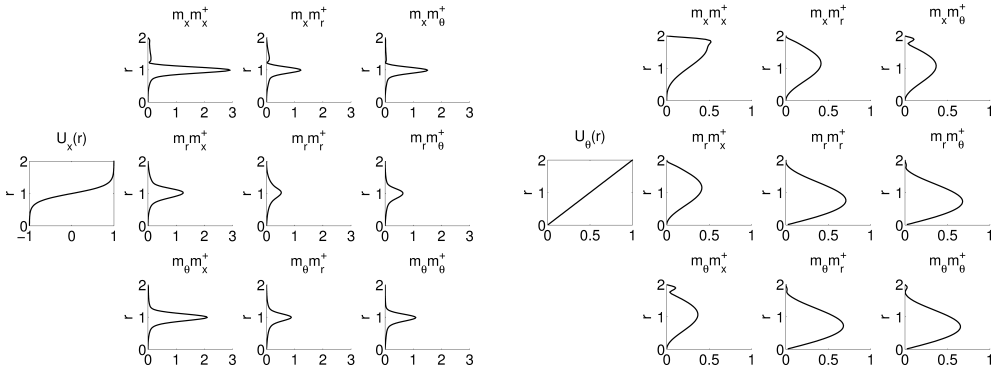

(a) Counterflow wake (b) Solid body rotation

Figure 5.9: The absolute value of the components of the sensitivity tensor $S_{ij} = \hat{\mathbf{m}}_i(\hat{\mathbf{m}}_j^+)^*$ for the $m = -1$ mode of (a) a parallel counterflow non-swirling wake, and (b) a vortex with solid body rotation. The single figures on the left in each subfigure show (a) the axial velocity profile of the wake base flow, and (b) the azimuthal velocity profile of the vortex base flow.

the axial momentum equation, have high amplitudes in the region in which there is strong shear in the $x-r$ component. Fourthly, the frames in the top row of figure 5.7 , which correspond to the influence of the axial momentum, have moderate amplitudes in this region.

This can be compared with figure 5.9, which shows the nine components of the structural sensitivity tensor for the $m = -1$ mode in two parallel flows. The nine components have the same meaning that they have for the two-dimensional case in figures 5.5, 5.6 and 5.7: they quantify the sensitivity of the eigenvalue to changes in the feedback between the three components of the perturbation momentum vector and the three components of the perturbation momentum equations. The only differences are that the flow is parallel and that the perturbations are assumed to be of the form $\mathbf{u}\exp(\mathrm{i}kx)$ in the axial direction. This gives the local structural sensitivity. If the flow were non-parallel, this would be a cross-stream slice through the two-dimensional structural sensitivity.

The flow in figure 8(a) is a parallel non-swirling counterflow wake. This

flow has uniform velocity in the axial direction and zero velocity in the radial and azimuthal directions. Therefore, all shear is concentrated in the $x-r$ component and only the Kelvin-Helmholtz (KH) mechanism is active. The frames in the left column of figure 5.9(a) have high amplitudes in the region in which there is strong shear in the $x-r$ component and the frames in the top row have moderate amplitudes in this region. It is also worth noting that the $r-r$ and $r-\theta$ components have low amplitudes. The centre-top frame of figure 5.8 shows that the $x-r$ component of shear is strong just outside the recirculation bubble (at $r=0.5$). Figure 5.7 shows that the structural sensitivity is large in this region, particularly in the left column and top row. The comparison with figure 5.9(a) leads us to believe that the feedback in this region is caused by the KH mechanism.

The four bottom-right frames in figure 5.7 have high amplitudes around the upstream stagnation point of the recirculation bubble. From figure 5.8, we notice that this does not correspond to regions of large shear. Hence, this cannot be explained by a KH mechanism. To explain this, we consider the nine components of the sensitivity tensor for the $m=-1$ mode in a flow with solid body rotation but no axial shear, shown in figure 5.9(b). For this flow, the highest sensitivities are in the $r-r$, $r-\theta$, $\theta-r$ and $\theta-\theta$ components, and they all have very similar magnitudes. This is typical of feedback that arises from the conservation of angular momentum. Specific examples of such a mechanism include the fictitious Coriolis force (Batchelor, 1967, §7.6) and the generalized centrifugal instability mechanism proposed by Leibovich & Stewartson (1983), who derived a criterion for the temporal instability of a parallel Batchelor vortex in the limit of large azimuthal wavenumber, m, and large axial wavenumber, k. In these limits, the perturbation is only affected by the local flow. The perturbations in this paper, however, are far from the large m and k limit and are therefore not localized. Consequently, it is questionable whether they can be identified with the generalized centrifugal instability. Even if we ignore these concerns, we find, in this flow, that the criterion is only satisfied in regions of strong axial flow, where the perturbations have large group velocity. When deriving global properties from a local

analysis, only the waves with zero group velocity contribute. On this basis, it seems unlikely that the generalized centrifugal instability is responsible for the strong feedback upstream of the breakdown bubble. We conclude simply that a mechanism involving conservation of angular momentum is active in the region just upstream of the breakdown bubble.

We can now explain why the adjoint global mode is large in the region upstream of the recirculation bubble, near the centreline (figure 5.4e). Let us consider the effect of a small open loop perturbation in this region. In this region, the axial vorticity of the base flow is an order of magnitude larger than the radial and azimuthal vorticity of the base flow. The perturbation vorticity is superposed on this. As a perturbation passes through this region, the fluid is compressed in the axial direction and stretched in the radial and azimuthal directions. By conservation of angular momentum, the vorticity in the radial and azimuthal directions increases, while the vorticity in the axial direction decreases. This increases the amplitude of the perturbation vorticity. The amplified perturbation then passes through the 'KH' region, where it is amplified by the classic Kelvin-Helmholtz mechanism. This description agrees with observations from experiments on vortex breakdown in swirling jets by Oberleithner, Sieber, Nayeri, Paschereit, Petz, Hege, Noack & Wygnanski (2011). These researchers found the wavemaker to be upstream of the breakdown bubble and the surrounding flow field to behave as an amplifier of upstream disturbances.

In summary, the nine components of the structural sensitivity reveal that, at the point of instability, two mechanisms are active in the wavemaker region of the global mode. The first is due to conservation of angular momentum in regions of strong strain in the flow, particularly upstream of the breakdown bubble. This mechanism is most sensitive to feedback involving the radial and azimuthal components of the perturbation momentum. The second is a classic KH mechanism in regions of strong shear. This mechanism is most sensitive to feedback involving the axial component of the perturbation momentum. We find that the first mechanism has more influence than the

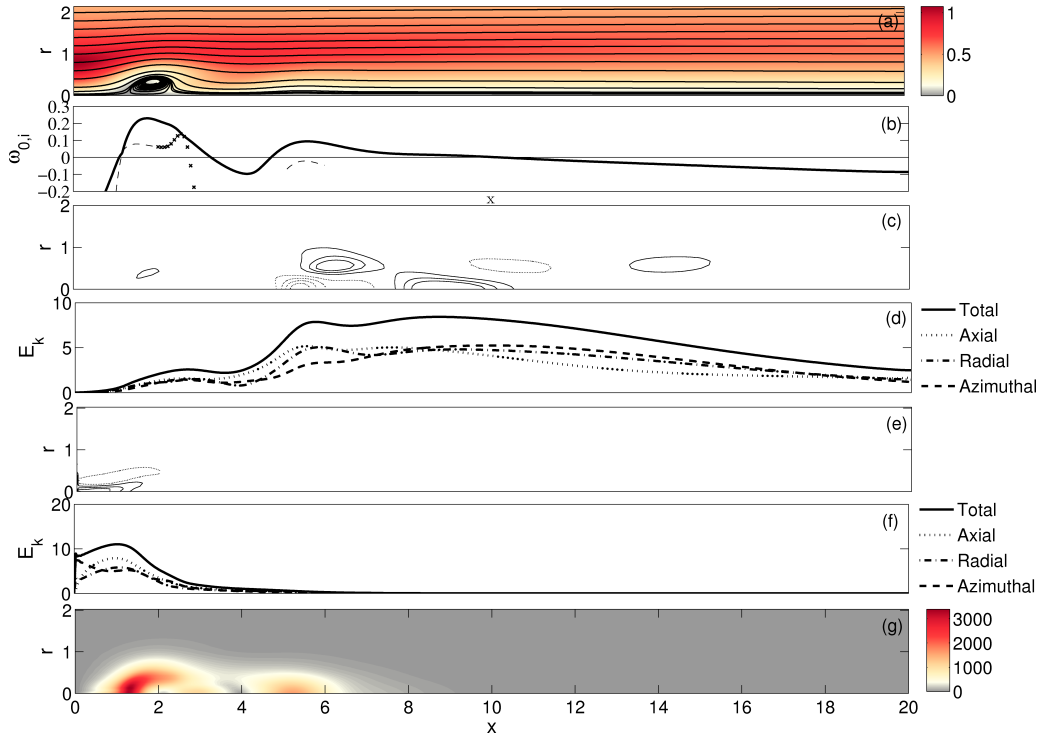

Figure 5.10: As for figure 5.4 but for $Sw = 1.0$. Frame (c) can be compared directly with Fig. 29(b) of Ruith *et al.* (2003) (but note that the vertical axis has been stretched in their figure)

second on the growth rate and frequency of spiral vortex breakdown.

5.4.1.3 Comparison with nonlinear behaviour

We now consider the reference case of $Sw = 1.0$ in light of the sensitivity analysis at $Sw = 0.915$. The main purpose of this section is to compare our linear global analysis with the nonlinear local analysis of Gallaire *et al.* (2006) and the weakly nonlinear global analysis of Meliga *et al.* (2012*a*). Figure 5.10 presents the results of the stability analysis for $Sw = 1.0$ in the same format as figure 5.4. The global mode shapes and spatial wavelengths agree very well with the DNS results in the linear regime shown in figure 29 of Ruith *et al.* (2003).

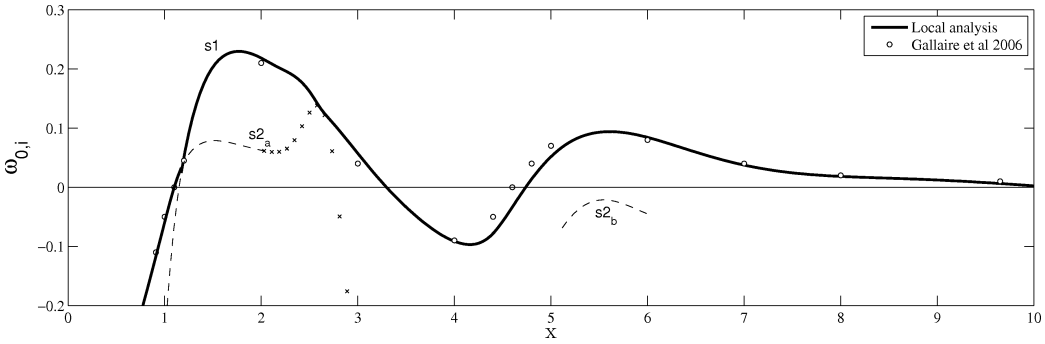

Figure 5.11: Local absolute growth rate, $\omega_{0,i}$, (thick line) as a function of streamwise distance for the $m = -1$ azimuthal wavenumber and $Sw = 1.0$. The thick line represents $\omega_{0,i}$ for the dominant saddle point ($s1$). The subdominant saddle points are shown by a dashed line where they are valid k^+/k^- pinch points and by crosses where they are not. The subdominant saddle points are located in regions of the flow in which there are two solutions of linear instability from the temporal analysis: the recirculation bubble (saddle $s2_a$) and the wake ($s2_b$). The streamwise domain of this flow extends to $x = 20$ but is not shown in this figure.

In agreement with Gallaire *et al.* (2006), figure 5.10(b) shows that the flow at $Sw = 1.0$ has two finite regions of absolute instability: a small region corresponding to the recirculation bubble and a large region corresponding to the wake. This is shown in more detail in figure 5.11, where our results are compared with results from figure 5 of Gallaire *et al.* (2006). Our results were obtained by locating saddle points of ω in the complex k-plane. Gallaire *et al.*'s results were obtained by extracting $\omega_{0\mathrm{i}}$ from linear DNS of locally-parallel flows created from the actual flow at 15 streamwise locations. The results are in very good agreement with each other, even capturing saddle switching around $x = 1$.

The structural sensitivity map in figure 5.10(g) shows that there is a region of high sensitivity around the upstream end of the bubble, and regions of lower sensitivity downstream in the wake. In order to understand how each of these regions affects the global mode, we consider the components of the sensitivity tensor.

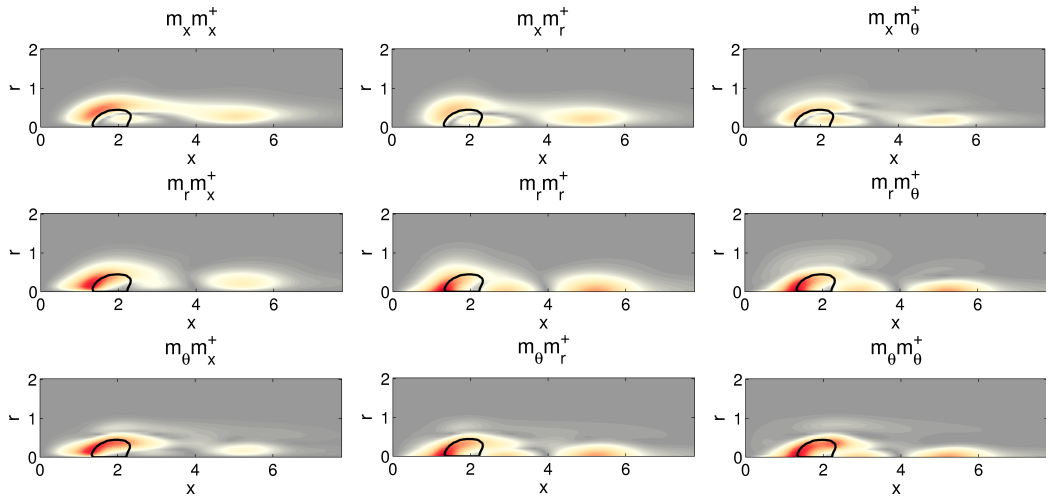

Figure 5.12: The absolute value of the components of the sensitivity tensor $S_{ij} = \hat{\mathbf{m}}_i(\hat{\mathbf{m}}_j^+)^*$ for the $m = -1$ mode at $Sw = 1.0$. The shading on all the plots scales from 0 (grey) to 1670 (red). The thick black line shows the breakdown bubble.

The real and imaginary parts (which are not shown here) are similar to figures 5.5 and 5.6 for $Sw = 0.915$ but show that the sensitive regions are not localized to just the bubble or just the wake in any component of the sensitivity tensor. This is evident in figure 5.12, which shows the absolute value of the sensitivity tensor at every point in the domain. In every plot, the regions around the bubble have greater sensitivity than the regions in the wake. Although both the bubble and the wake affect the instability, we deduce that the bubble is more influential than the wake in affecting both the growth rate and the frequency of the linear global mode.

In contrast to the linear results, Gallaire *et al.* (2006) concluded that the nonlinear global behaviour is governed by the wake and not by the bubble. They extracted the spatial growth rate of perturbation kinetic energy from Ruith's saturated nonlinear DNS. They compared this with the spatial growth rates at the two points where the flow transitions from convective to absolute instability, in accordance with the nonlinear mode selection crite-

rion of Pier *et al.* (2001). The spatial growth rate at the leading edge of the wake region matches that of the saddle point of the local analysis there. Our local analysis gives the same results as that of Gallaire *et al.* (2006).

In summary, as the results in Table 5.1 show, the frequency predicted by the nonlinear local analysis in the wake is very close to the limit-cycle frequency measured in Ruith's DNS. The frequency predicted by our linear global analysis is also close to this limit-cycle frequency. However, our sensitivity analysis finds that the bubble is more influential than the wake in determining this frequency. We have not yet been able to find a convincing explanation for this behaviour. One possibility is to consider the nonlinear modification of the baseflow due to the direct global mode. This would be largest in the wake, close to where the direct global mode reaches a maximum. In our flow, the linear wavemaker region is quite far upstream of this location. For small steps beyond the bifurcation point (at $Sw = 0.915$), we would expect the flow to be significantly modified in the wake (Chomaz, 2005), which Meliga *et al.* (2012*a*) found to be the case.

5.4.2 Double-helical mode, $m = -2$

At lower Reynolds number, Meliga & Gallaire (2011) have shown that the double-helical mode, with $m = -2$, becomes globally unstable before the $m = -1$ mode. In this section, we consider a flow with $Re = 60$.

5.4.2.1 Onset of instability

As the swirl is increased, an unstable mode first appears at $1.50 < Sw \leq 1.55$ with $m = -2$. Figure 5.13 shows the eigenvalue spectrum at $Sw = 1.55$. Figure 5.14 shows the base flow at this swirl together with the results of the stability analysis in the same format as previous figures. The vortex breakdown bubble is larger and extends further downstream than at lower swirl. The structural sensitivity map shows that the wavemaker lies near the 'neck' of the bubble, between $2.0 \leq x \leq 4.0$. The maximum value of the structural sensitivity is an order of magnitude lower than the maximum for $Sw = 1.0$

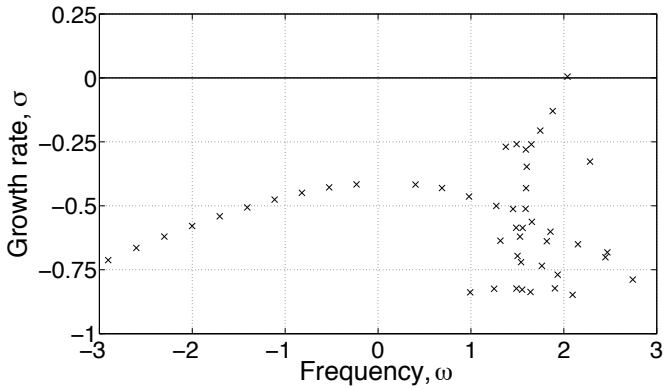

Figure 5.13: Eigenvalue spectrum for $|m| = 2$ for the base flow at $Sw = 1.55$ and $Re = 60$. The 50 least stable modes are shown. Modes with $\omega < 0$ correspond to $m = +2$, while modes with $\omega > 0$ correspond to $m = -2$.

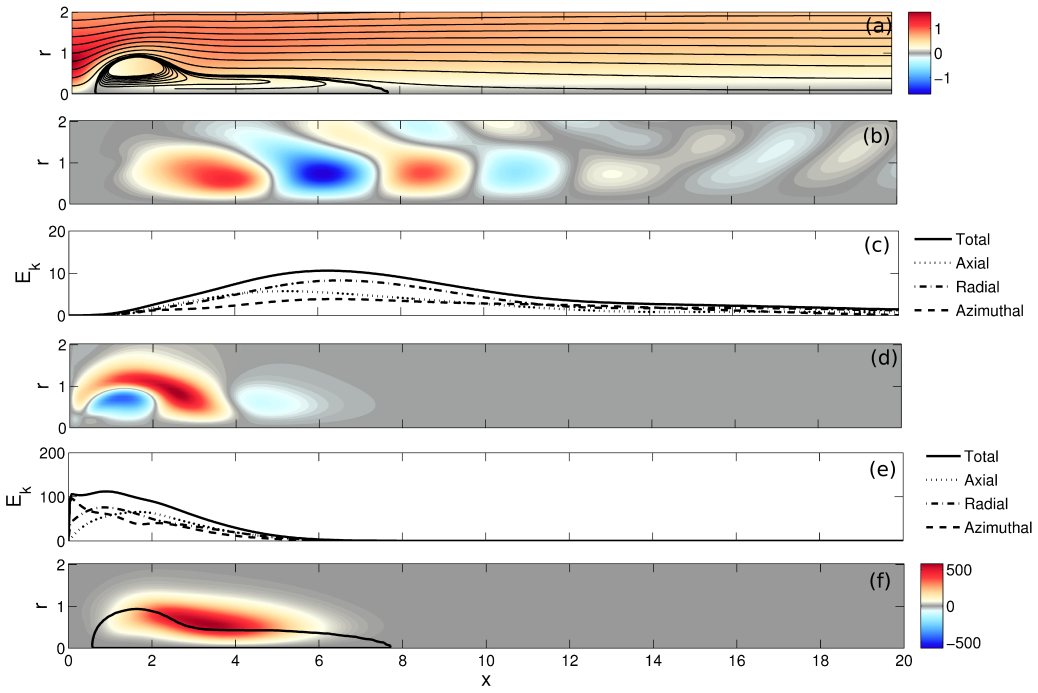

Figure 5.14: As for figure 5.4 but for $m = -2$ at $Sw = 1.55$ and $Re = 60$.

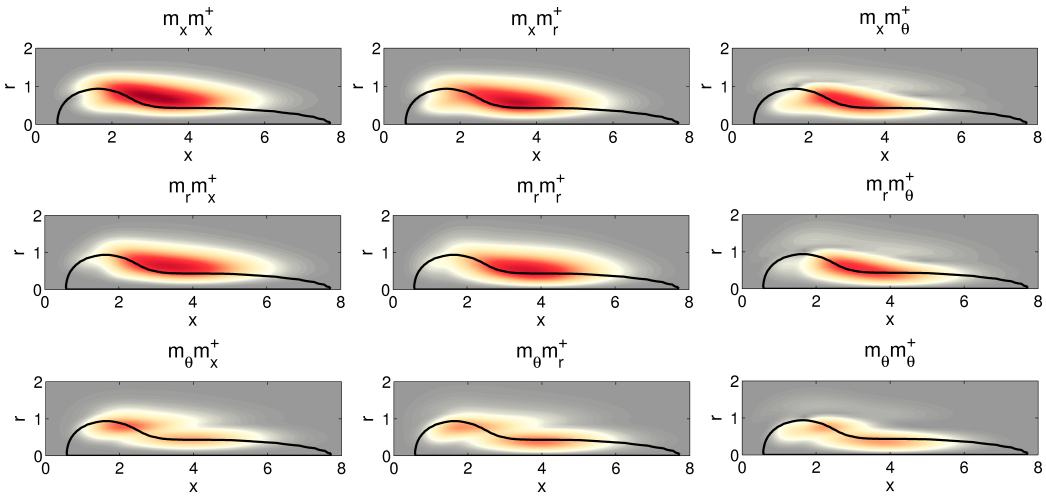

Figure 5.15: The absolute value of the components of the sensitivity tensor $S_{ij} = \hat{\mathbf{m}}_i(\hat{\mathbf{m}}_j^+)^*$ for the $m = -2$ mode at $Sw = 1.55$ and $Re = 60$. The shading on all the plots scales from 0 (grey) to 270 (red). The thick black line shows the breakdown bubble.

and $Sw = 0.915$ at $Re = 200$. This is because the Reynolds number is lower and the flow is more nonparallel. This means that the flow is less non-normal and less sensitive to perturbations of the linear operator.

5.4.2.2 Mechanisms of instability

To understand more about the physical mechanisms that are active in the wavemaker, we consider the components of the sensitivity tensor. Figure 5.15 shows the absolute value of the sensitivity tensor for the $m = -2$ mode. Large sensitivities are seen in the four frames in the top left-hand corner. These correspond to feedback between the axial and radial components of the momentum. The largest magnitude is for feedback of the axial momentum into the axial momentum equation. There is moderate sensitivity to feedback of the axial and radial momentum into the azimuthal momentum equation. The smallest magnitudes are seen in the frames in the bottom row. These correspond to feedback of the azimuthal momentum into the other components of momentum and also to itself. We conclude that the

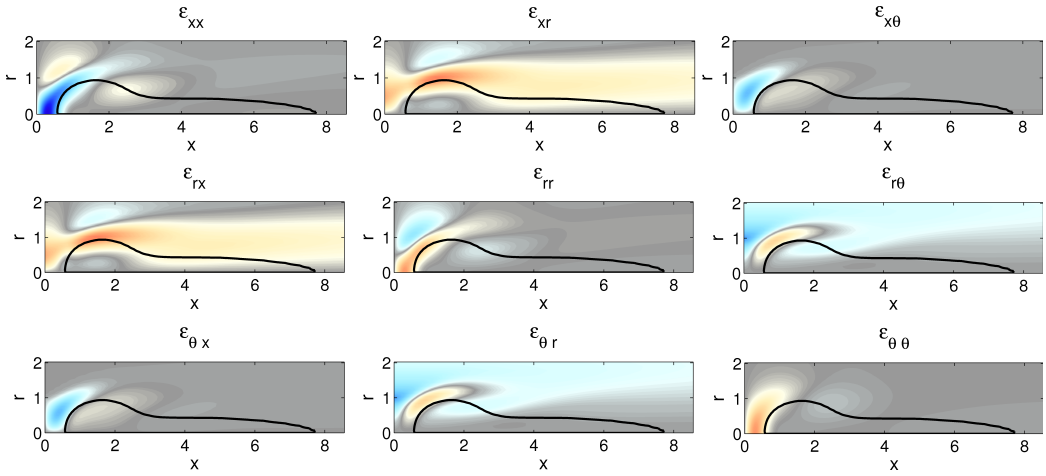

Figure 5.16: The components of the rate-of-strain tensor $S_{ij} = \frac{1}{2}\left[\nabla\bar{\mathbf{u}} + (\nabla\bar{\mathbf{u}})^T\right]$ for the base flow at $Sw = 1.55$ and $Re = 60$. The shading on all the plots scales from -5 (blue) to 5 (red). The thick black line shows the breakdown bubble.

feedback mechanisms that are most influential in causing double-helical vortex breakdown involve the axial and radial components of the perturbation momentum.

The strain rate tensor for the base flow is shown in figure 5.16. The strain is greatest in the region just upstream of the bubble, while the shear is largest near the inlet at $r = 1$ and around the head of the bubble, $x \leq 2.0$. Neither of the these correspond to regions where the sensitivity is high. The regions with high sensitivity correspond to a region of weak strain: the flow accelerates over the neck of the bubble (top left frame). The flow also has moderate shear in this region: in the $x - r$ and $r - \theta$ components at the edge of the bubble. This suggests that conservation of angular momentum and the K-H mechanism reinforce each other in this region.

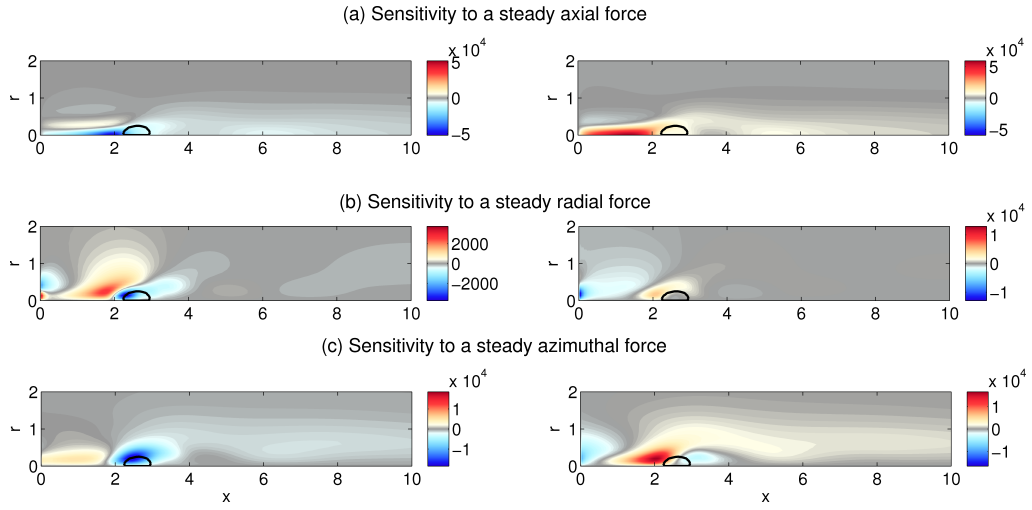

Figure 5.17: The sensitivity of the marginally unstable eigenvalue of the $m = -1$ mode at $Sw = 0.915$ and $Re = 200$ to steady forcing, $\nabla_{\bar{\mathbf{F}}}\lambda$. The colours show the sensitivity of the growth rate (left), and frequency (right).

5.5 Sensitivity to a control force

We now consider the effect of a small control force on the marginally unstable eigenvalue for the $m = -1$ mode at $Re = 200$ and for the $m = -2$ mode at $Re = 60$.

5.5.1 Helical mode, $m = -1$

Figure 5.17 shows the real and imaginary parts of the adjoint base flow momentum fields for the $m = -1$ mode at $Sw = 0.915$ and $Re = 200$. These represent the sensitivity of the growth rate and frequency of the helical mode of vortex breakdown to a steady body force. The eigenvalue is most sensitive to a steady axial force near the axis upstream of the breakdown bubble. In this region, a positive axial force (in the direction of the flow) makes the helical mode more stable, while positive radial and azimuthal forces have a weak destabilizing effect. This is due to conservation of angular momentum, which is the dominant mechanism responsible for destabilization of this mode. At the edge of the bubble around $r = 0.5$, positive radial and azimuthal forces have a strong stabilizing influence. Downstream of the bubble, positive axial

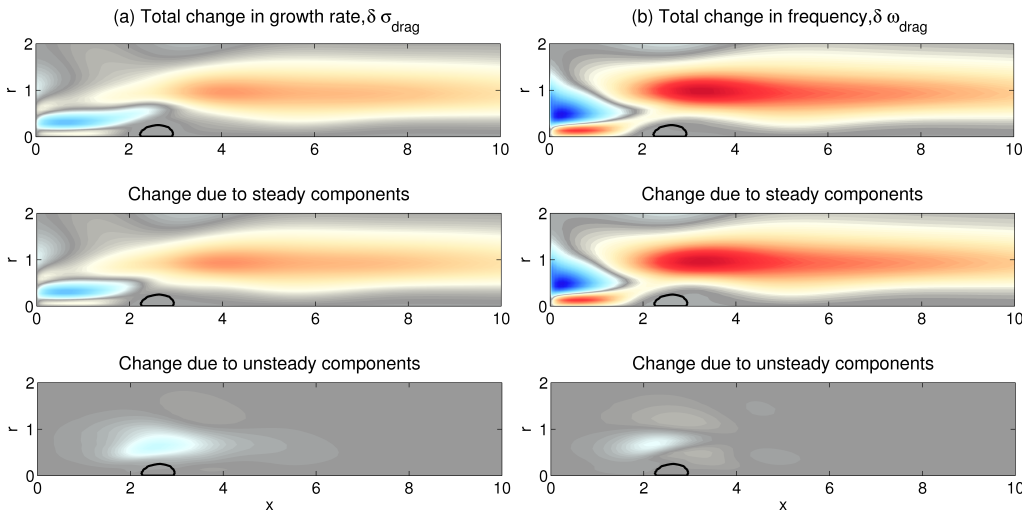

Figure 5.18: The predicted change (scaled by $C_D d_w$) in the marginally unstable eigenvalue of the $m = -1$ mode at $Sw = 0.915$ and $Re = 200$ due to the drag on a thin axisymmetric control ring, $\delta\lambda_{drag}$. The shading on all the plots is equal and goes from -0.0085 (blue) to 0.0085 (red).

and azimuthal forces have a weak stabilizing effect. Physically, this is because these forces increase the advection of perturbations downstream.

These sensitivity maps are now used to model the effect of the drag from a thin axisymmetric control ring on the marginally unstable eigenvalue. The drag from the control ring is modelled as described in §4.5.1. The predicted effect of the drag from the control ring on the growth rate and frequency is shown in figure 5.18. We find that the control ring causes a greater change in the frequency than in the growth rate. There is a narrow region upstream of the bubble where the control ring has a stabilizing effect. There is also a large region downstream of the bubble where the control ring has a destabilizing effect. Although this is a region of weak sensitivity (see figure 5.17), the base flow axial and azimuthal velocities are relatively high here and so, the axial and azimuthal components of the drag force from the ring are also relatively high. These lead to a relatively large predicted change in growth rate and frequency. It is also interesting to note that the effect of the steady components of the drag force is at least 3 times greater than the effect of the

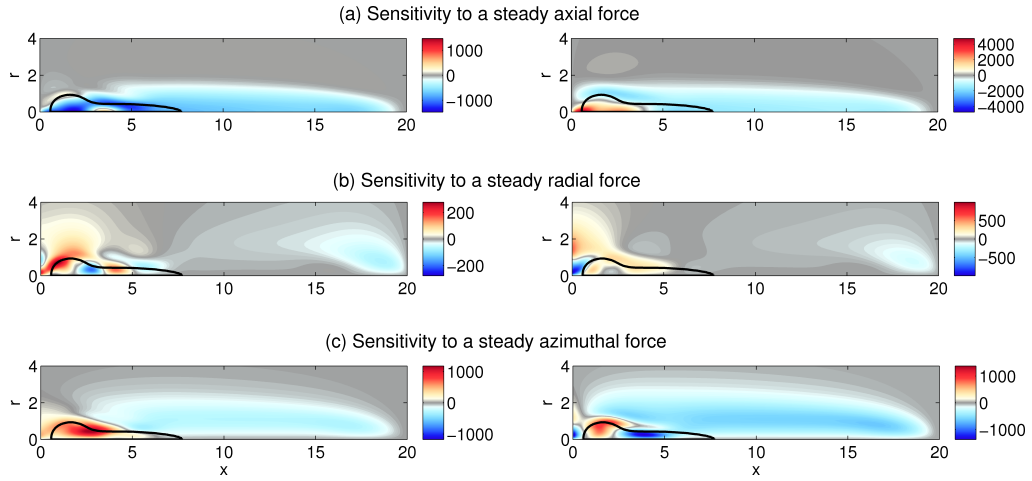

Figure 5.19: The sensitivity of the marginally unstable eigenvalue of the $m = -2$ mode at $Sw = 1.55$ and $Re = 60$ to steady forcing, $\nabla_{\bar{\mathbf{F}}}\lambda$. The colours show the sensitivity of the growth rate (left), and frequency (right).

unsteady components.

5.5.2 Double-helical mode, $m = -2$

Figure 5.19 show the real and imaginary parts of the adjoint base flow for the $m = -2$ mode at $Re = 60$ and $Sw = 1.55$. The sensitivity to steady forcing is around an order of magnitude smaller than the sensitivity seen in figure 5.17. However, large regions of the flow, including regions inside the vortex breakdown bubble, are moderately or highly sensitive to steady momentum sources. The largest sensitivity is seen in the top frame of figure 5.19(b): this represents the sensitivity of the frequency to a steady axial force. This sensitivity is maximum near the axis just upstream of the vortex breakdown bubble.

For practical purposes, it is clearer to plot the effect of the drag from a control ring on the growth rate and frequency. This is shown in figure 5.20. Many features are similar to those seen in figure 5.18 for the $m = -1$ mode. There is a narrow stabilizing region that extends from the inlet to the head of

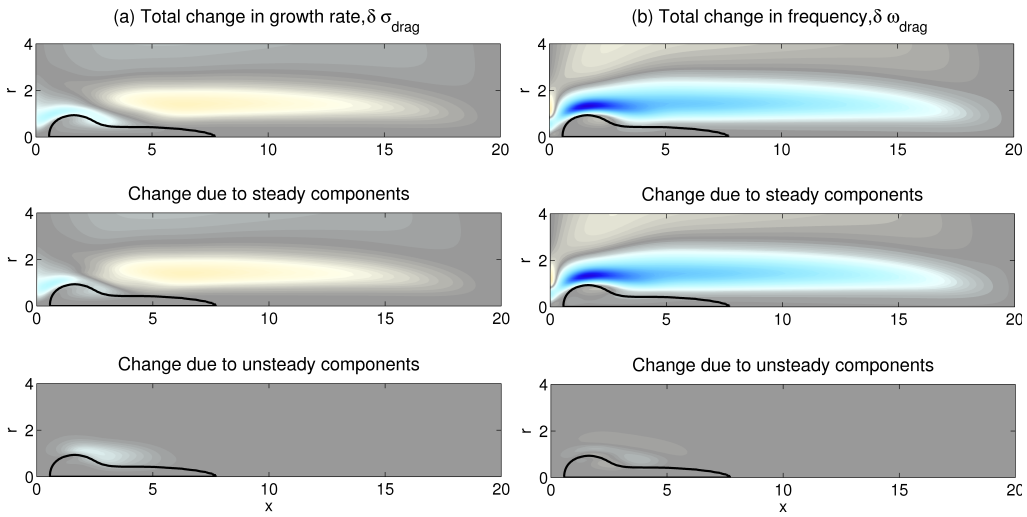

Figure 5.20: The predicted change (scaled by $C_D d_w$) in the marginally unstable eigenvalue of the $m = -2$ mode at $Sw = 1.55$ and $Re = 60$ due to the drag on a thin axisymmetric control ring, $\delta\lambda_{drag}$. The shading on all the plots is equal and goes from -0.0102 (blue) to 0.0102 (red).

the breakdown bubble, and a larger destabilizing region further downstream. The effect of the steady components of the drag force is once again dominant compared to the unsteady components. The main point to note from this analysis is that, despite the wavemaker being further downstream around the neck of the breakdown bubble, the global mode can be effectively controlled by placing a suitable controller near the inlet.

5.6 Summary

In this chapter, we have studied the linear global stability of the steady axisymmetric vortex breakdown bubble observed in the simulations of Ruith *et al.* (2003). We have confirmed that, at moderate swirls, spiral vortex breakdown is caused by an unstable eigenmode of azimuthal wavenumber $m = -1$, which we call the helical mode. At higher swirls, spiral vortex breakdown is caused by an unstable eigenmode of azimuthal wavenumber $m = -2$, which we call the double-helical mode. For both these cases, the adjoint of this direct global mode has also been calculated. By overlapping

the direct and the adjoint global modes, we have found the location of the wavemaker, which can be interpreted as the region responsible for causing spiral vortex breakdown (Giannetti & Luchini, 2007). By considering the nine components of the structural sensitivity tensor, we have identified the physical mechansisms that are responsible for causing spiral vortex breakdown. We have also used a local stability analysis to work out the regions of absolute instability in the flow. We have then used the adjoint base flow to identify the regions where a control force will have the most influence on the growth rate and frequency of the global mode. In particular, we have considered the case of a thin axisymmetric control ring, and identified regions where it could be placed to stabilize the helical and double-helical modes of vortex breakdown.

When the $m = -1$ mode first goes unstable, at $Sw = 0.915$, the wavemaker is located just upstream of the breakdown bubble, which is the only region of the flow that is absolutely unstable. The structural sensitivity tensor reveals that this mode is caused by two physical mechanisms. The first mechanism is most sensitive to feedback between the radial and azimuthal components of the perturbation momentum, corresponding to the region of strong strain just upstream of the breakdown bubble. We interpret this mechanism to be related to conservation of angular momentum. The second is the classic Kelvin-Helmholtz mechanism, which is most sensitive to feedback involving the axial component of the perturbation momentum. This corresponds to the regions of strong shear around the bubble. We find that the former mechanism is dominant.

We have also considered the case of $Sw = 1.0$, which has two regions of absolute instability, one in the bubble and one in the wake. Our linear analysis has found that the region around the bubble is more influential than the wake in determining the growth rate and frequency. Previously, Gallaire *et al.* (2006) had found that the nonlinear frequency for this case is determined by the wake and our local analysis agrees with theirs. The frequencies from our analysis and Gallaire's analysis are both close to the limit-cycle

frequency observed in Ruith *et al.*'s 3D DNS.

When the $m = -2$ mode goes unstable, at $Re = 60$ and $Sw = 1.55$, the wavemaker is located along the neck of the breakdown bubble, which is larger than at $Sw = 0.915$. The structural sensitivity tensor reveals that this mode is most sensitive to feedback between the axial and radial components of the perturbation momentum, corresponding to regions of weak strain and shear. This leads us to conclude that both conservation of angular momentum and the $K - H$ mechanism are equally dominant and reinforce one another in the wavemaker.

We have also considered the sensitivity of the $m = -1$ and $m = -2$ modes of spiral vortex breakdown to open loop steady forcing. For the $m = -1$ mode, we find that the region upstream of the breakdown bubble is highly sensitive to steady forcing whereas for the $m = -2$ mode, large regions of the flow are highly sensitive to steady forcing. Both modes are most sensitive to a steady axial force. We have used these maps to calculate the effect of a control ring placed in the flow. We find that both modes can be stabilized by placing a ring of suitable radius just downstream of the inlet.

The motivation for this work is to extend this analysis to devices such as fuel injectors. This implies that small changes to the injector will have a strong influence on the hydrodynamic stability of the flow, and that we can use these techniques to predict the influence of such changes.

6

Global stability and control of swirling jets

This chapter is devoted to studying the global stability, structural sensitivity and control of swirling jets, whose velocity profiles are more representative of the velocity profiles observed in experiments on swirling jets. The local stability analysis has been performed by Matthew Juniper.

6.1 Introduction

In the previous chapter, the Grabowski profile was used to study the global stability and structural sensitivity of the spiral modes of vortex breakdown in a uniform-density swirling flow. The Grabowski profile is a good model for swirling flow in tubes and ducts. However, it is not representative of the flow field near the exit plane of a swirling jet. Figure 6.1 shows velocity profiles measured in an experiment on swirling water jets by Billant *et al.* (1998). The azimuthal velocity reaches a maximum at around half jet radius and then decays to zero at the edge of the jet. This differs from the Grabowski profile, which features a $1/r$ decay rate for the azimuthal velocity and a larger azimuthal shear layer. The aim of this chapter is to study the linear global stability and structural sensitivity of swirling jets whose velocity profile is similar to the ones shown in figure 6.1.

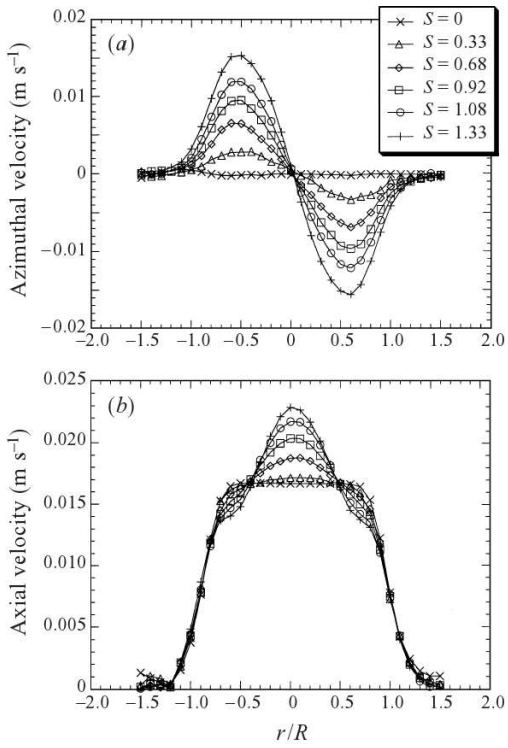

Figure 6.1: Taken from Billant *et al.* (1998). (a) Azimuthal and (b) axial velocity profiles obtained in experiments on swirling water jets, for various swirl paramters, near the exit plane.

The background for this chapter is the experimental study of Billant *et al.* (1998). These researchers studied the effect of increasing swirl on the dynamics of a swirling water jet exiting into a large tank of water, at Reynolds numbers $300 < Re < 1200$. In agreement with previous studies, they found that vortex breakdown set in above a critical value of swirl. Below this threshold, at moderate swirls, they observed that the swirling jet took the form of a double-helix. Above this threshold, they observed four distinct forms of vortex breakdown: an axisymmetric bubble, an axisymmetric conical sheet, and asymmetric forms of the bubble and cone states. They observed that the upstream end of the axisymmetric bubble was steady, but that the downstream end of the bubble led to an unsteady precessing spiral tail. In contrast, they

observed that the cone mode was inherently unsteady: its stagnation point oscillated along the jet axis and this was accompanied by a change in the angle of the conical sheet. These oscillations, however, were very slow, with periods of the order of a few hundred seconds. The asymmetric states only appeared at $Re \gtrapprox 800$ and due to the axisymmetric nature of the code, are not considered in this thesis.

The double-helical mode observed before vortex breakdown forms the motivation for section 6.3 of this chapter. Gallaire & Chomaz (2003) used a local linear stability analysis to study a velocity profile that was a good model for the velocities measured by Billant *et al.* (1998) near the exit plane in their experiments. Gallaire & Chomaz (2003) found that this velocity profile, which we label the *Billant* jet profile, was locally absolutely unstable to a mode of azimuthal wavenumber $m = -2$ and suggested that this accounted for the experimental observation of a double-helix before the onset of vortex breakdown. In a recent experimental investigation of swirling jets in water at $Re = 1000$, Liang & Maxworthy (2005) observed the same qualitative features as those observed by Billant *et al.* (1998). An important difference, however, was that Billant *et al.* (1998) observed a counter-rotating, co-winding double-helical mode while Liang & Maxworthy (2005) observed a counter-rotating counter-winding double-helical mode before vortex breakdown. Liang & Maxworthy (2005) attributed this to the differences in the velocity profiles between their experiments and those of Billant *et al.* (1998) - the relative location of the azimuthal and axial shear layers was different between these two studies. Liang & Maxworthy (2005) also studied spectra of the flow field to determine whether the double-helical mode that they observed before vortex breakdown was self-excited. The results were not conclusive but suggested that the double-helical mode was self-excited and globally unstable. In this chapter, the velocity profiles used by Gallaire & Chomaz (2003) are used to study the linear global stability of a uniform-density swirling jet before the onset of vortex breakdown. The aim is to confirm whether the double-helical mode observed in the experiments of Billant *et al.* (1998) is due to a linear global instability.

The bubble and cone states of vortex breakdown form the motivation for the second part of this chapter. In agreement with Billant *et al.* (1998), Liang & Maxworthy (2005) observed a counter-rotating $m = 1$ mode after the onset of vortex breakdown. They suggested that this mode was globally unstable and due to the existence of a region of local absolute instability in the wake of the breakdown bubble. These observations agree qualitatively with the simulations of vortex breakdown using the Grabowski profile by Ruith *et al.* (2003) and with the results of the previous chapter. In this chapter, the bubble and cone states obtained using the Billant jet profile are studied using the tools discussed in chapters 2 and 3. The sensitivity maps that are obtained are compared to those obtained in the previous chapter for the Grabowski profile. These would be expected to be of more interest for fuel injectors and experimental investigations of swirling jets.

6.2 Flow configuration

The linear global stability of a swirling jet is studied in a cylindrical domain of length X_{max} and radius R_{max}. On Ω_{in}, the velocity profiles used by Gallaire & Chomaz (2003) are imposed. The axial velocity is modelled using a top-hat profile that was originally proposed by Monkewitz & Sohn (1986). The azimuthal velocity is modelled using a profile that was first proposed by Carton & McWilliams (1989). The density profile is modelled using the same top-hat profile as that used for the axial velocity. The flow variables are nondimensionalized by the centreline jet axial velocity, the jet diameter, and the ambient density. The nondimensional base flow inlet profile is then

given by

$$\begin{aligned}
y(0,r) &= \frac{1}{1+(e^{4r^2\log(2)}-1)^N}, && (6.1a)\\
\bar{T}(0,r) &= y(0,r), && (6.1b)\\
\bar{\rho}(0,r) &= \frac{1}{(S_1-1)T(0,r)+1}, && (6.1c)\\
\bar{m}_x(0,r) &= \bar{\rho}(0,r)\left(u_c+(1-u_c)y(0,r)\right), && (6.1d)\\
\bar{m}_r(0,r) &= 0, && (6.1e)\\
\bar{m}_\theta(0,r) &= \bar{\rho}(0,r)\left(2qre^{-(2r/r_v)^\alpha}\right), && (6.1f)
\end{aligned}$$

where N models the thickness of the axial shear layer, S_1 is the ratio of the ambient-density to jet-density, u_c is a co-flow velocity, q is a swirl parameter, r_v models the vortex-core size and α models the thickness of the azimuthal shear layer. The Reynolds number, Re, is defined in terms of the jet diameter, jet axial velocity, and jet density.

Gallaire & Chomaz (2003) used a second axial velocity profile to model the overshoot observed by Billant *et al.* (1998) in their experimentally measured axial velocity profiles. However, Gallaire & Chomaz (2003) found that the linear stability analyses of these two model profiles were very similar and suggested that the basic profile captured most of the physics of the problem. In this chapter, therefore, only the basic profile (without the overshoot) is used.

The base flow inlet profile is defined such that it matches the experimental measurements of Billant *et al.* (1998). Gallaire & Chomaz (2003) found values of $N = 3$, $r_v = 0.9$ and $\alpha = 4$ to fit well with the experimental profiles and these values are used here too. The density ratio is set to $S_1 = 1.0$ and the temperature profile at the inlet is set to zero to model a uniform-density swirling jet. A small coflow velocity of $u_c = 0.01$ is used to improve numerical stability.

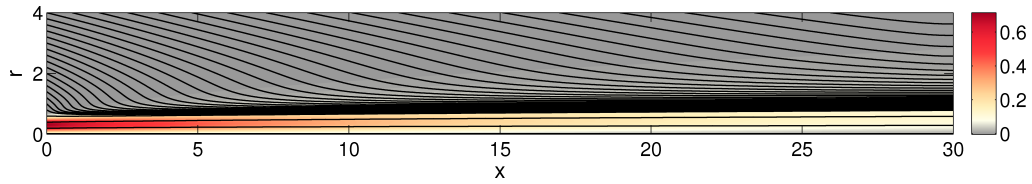

Figure 6.2: The steady base flow for a swirling jet with $Re = 667$ and $q = 1.48$. The streamlines show the axial and radial velocities and the colour shows the azimuthal velocity.

6.3 Before vortex breakdown

In this section, the linear global stability of a swirling jet before the onset of vortex breakdown is investigated. A grid measuring 127×513 is used for a domain with $X_{max} = 30$ and $R_{max} = 8$. The value of X_{max} is chosen to be approximately equal to that in the experiments of Billant *et al.* (1998). The value of R_{max} is larger than that used in the previous two chapters because the amount of fluid entrained into the jet is greater and the traction-free lateral boundary condition is not suitable for very large entrainment velocities. A steady axisymmetric base flow is obtained for $Re = 667$ and $q = 1.48$. This corresponds to the flow regime where Billant *et al.* (1998) observed a double-helical mode. The base flow is shown in figure 6.2.

6.3.1 Global stability

The growth of small perturbations of azimuthal wavenumber $m = 2$ on top of the steady base flow are considered. Instead of looking at just the most unstable linear eigenmode, for this case, it is more appropriate to look at the 50 most unstable eigenmodes. The eigenvalues are plotted in figure 6.3, together with the eigenvalues for a domain with $X_{max} = 15$. For both domain lengths, the eigenvalue solver finds a hoop of eigenvalues with a positive growth rate, which indicates global instability. Figure 6.4 shows the spatial structure of one of these unstable modes. The mode reaches maximum amplitude near the exit plane. This would suggest that the domain length is insufficient to capture the true location of maximum amplitude. However, the amplitude

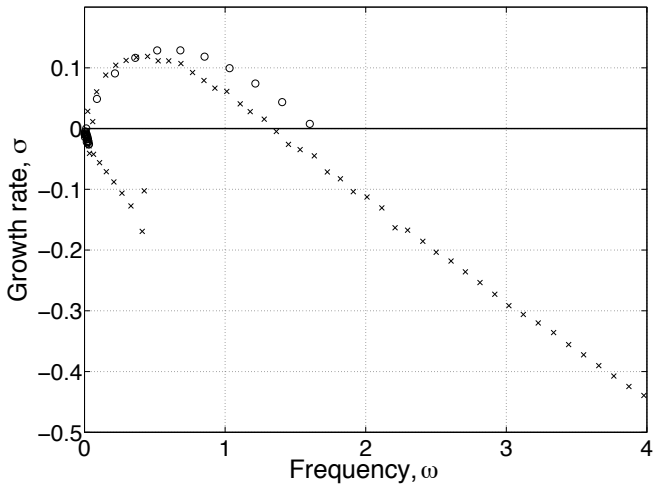

Figure 6.3: Eigenvalue spectrum for $m = 2$ for the base flow shown in figure 6.2 for a domain with $X_{max} = 30.0$ (crosses) and a domain with $X_{max} = 15.0$ (circles).

of the mode grows over 9 orders of magnitude between the inlet and outlet. This shows that the mode experiences large exponential growth in space. Such large growth has also been observed in several previous studies.

In a study on the uniform-density Batchelor vortex, Heaton *et al.* (2009) found that their eigenvalue solver, which was based on an incompressible version of the code developed by Nichols *et al.* (2007)), could not resolve modes which varied over 6 orders of magnitude. These unresolved modes appeared in the form of a hoop of eigenvalues and were not affected by using a finer mesh. They suggested that this was related to the non-normality of the linear operator and that this hoop was actually part of the 10^6 pseudo-spectrum of the linear operator. They found that decreasing the axial length of the domain reduced the convective non-normality and for a sufficiently small axial length, the true global mode could be obtained.

In a study on uniform-density non-swirling jets, which are known to be linearly globally stable, Garnaud *et al.* (2013) faced similar problems when

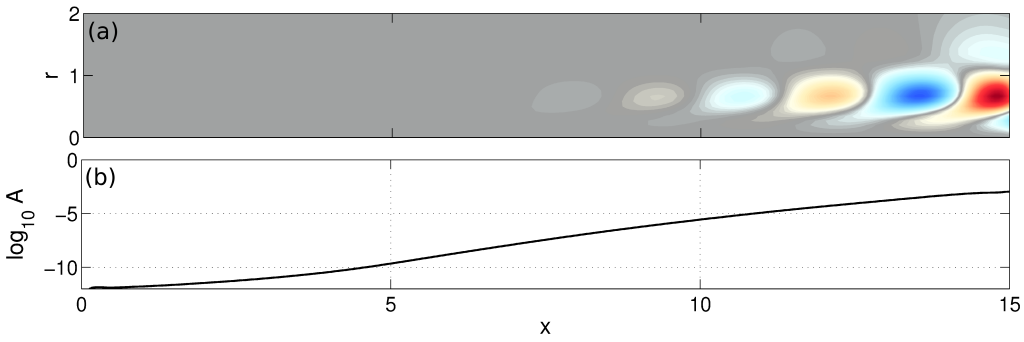

Figure 6.4: From top, (a) The real part of the axial momentum of the most unstable mode for $m = 2$ at $Re = 667$ and $q = 1.48$ in a domain with $X_{max} = 15.0$, and (b) the amplitude of the direct global mode, $A(x) = \sqrt{\int_0^{R_{max}} |\mathbf{u}|^2 r dr}$ through the domain.

obtaining the linear global eigenmodes for $m = 0$. The linear eigenmodes that were obtained all had maximum amplitude at or near the outlet boundary and were dependent on the axial length of the domain. Strong exponential growth in space was shown to be possible even in regions of the flow that are locally stable.

These indicate that the unstable modes in figure 6.3 are not the eigenmodes of the streamwise-unconfined flow and that these modes must be related to the flow being convectively unstable. In order to confirm this, the linear impulse response is calculated for perturbations with $m = 2$ developing on top of the base flow in figure 6.2. This is performed by imposing an initial condition of a Gaussian of unit magnitude at $(x, r) = (1.0, 0.5)$ in the axial velocity. The linearized equations are then marched forward in time using the direct time-stepping code described in chapter 3.

Figure 6.5(a) plots the amplitude of the wavepacket in the domain for $10 < t < 90$. Between $10 < t < 40$, the maximum amplitude of the wavepacket increases and the location of maximum amplitude moves downstream. The amplitude of the wavepacket at a point upstream of the maximum decreases with increasing time. This is typical of local convective

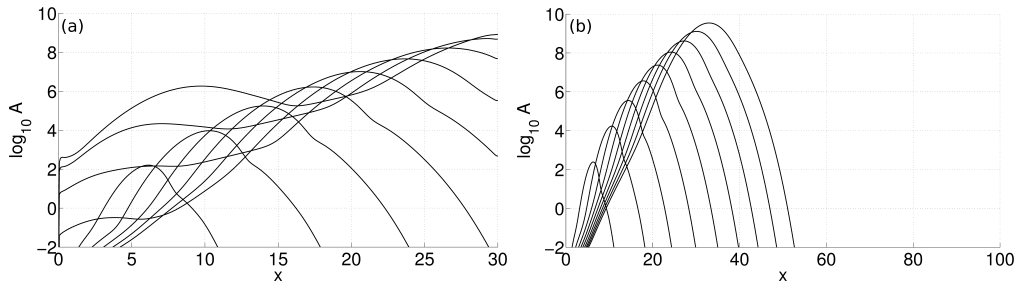

Figure 6.5: The linear impulse response for $m = 2$ of the Billant Jet before vortex breakdown at $Re = 667$ and $q = 1.48$ for a domain with (a) $X_{max} = 30.0$, and (b) $X_{max} = 100.0$. The amplitude of the wavepacket in the domain is shown for $10 \leq t \leq 100$. The impulse was localized at $(x_0, r_0) = (1.0, 0.5)$.

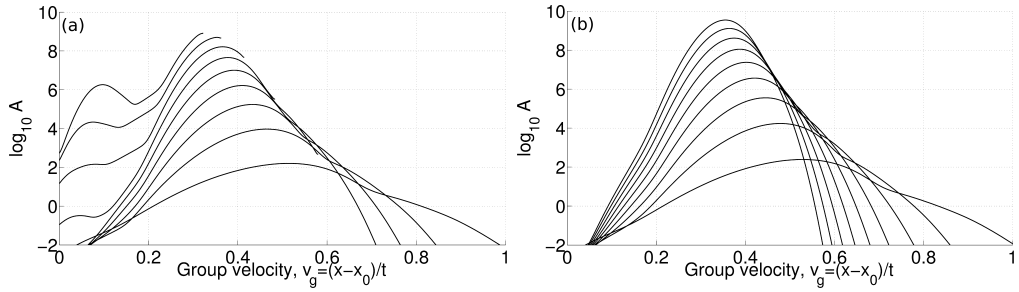

Figure 6.6: The linear impulse response for $m = 2$ of the Billant Jet before vortex breakdown at $Re = 667$ and $q = 1.48$. for a domain with (a) $X_{max} = 30.0$, and (b) $X_{max} = 100.0$. The amplitude of the wavepacket is plotted against the group velocity for $10 \leq t \leq 100$. The impulse was localized at $(x_0, r_0) = (1.0, 0.5)$.

instability. For $40 < t < 50$, the leading edge of the wavepacket has a significant amplitude when it reaches the outlet boundary. The convection velocity used in the boundary condition at the outlet is equal to the maximum axial base flow velocity. The perturbation velocities, however, are now significantly larger than this convection velocity and so, the outlet boundary perturbs the inlet through pressure feedback. This causes the amplitude in the upstream part of the domain to increase for $60 < t < 90$. This reflection can be avoided by obtaining the base flow for a longer domain. For example, figure 6.5(b) shows the impulse response for a grid with 253×2049 points for a domain with $X_{max} = 100.0$ and $R_{max} = 8.0$. The impulse response can now clearly be seen to be convective in nature.

Figure 6.6 plots the amplitude of the wavepacket against the group velocity of the wavepacket. With increasing time, a group velocity of around $0.30 < v_g < 0.35$ is seen to dominate the dynamics of the $m = 2$ mode. It is important to note that the amplitude of the wavepacket increases by almost 9 orders of magnitude during this time. Only waves of zero group velocity contribute towards global instability. For this case, the waves of zero group velocity decay and it is only the reflection of waves off the boundaries in the shorter domain that causes the zero group velocity waves to be amplified. It is also important to note that it is sufficient to run simulations only for $m = +2$. If a mode with $m = -2$ was more unstable, it would be seen in the linearized DNS, and the eigenvalue spectrum would show this mode as having negative frequency. Such a mode has not been found. The results in this section, therefore, show that both the $m = +2$ and $m = -2$ modes are linearly globally stable in an unconfined domain.

6.3.2 Local stability

Gallaire & Chomaz (2003) carried out a local stability analysis of the inlet profile and found that the $m = -2$ mode was absolutely unstable. They calculated the linear impulse response of a parallel base flow in a long domain

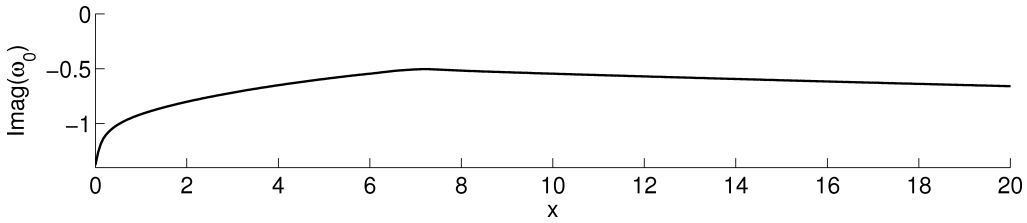

Figure 6.7: The local absolute growth rate, $\mathrm{Im}(\omega_0)$, for $m = -2$ for the base flow shown in figure 6.2 up to $x = 20.0$. The saddle swaps around $x = 7.0$.

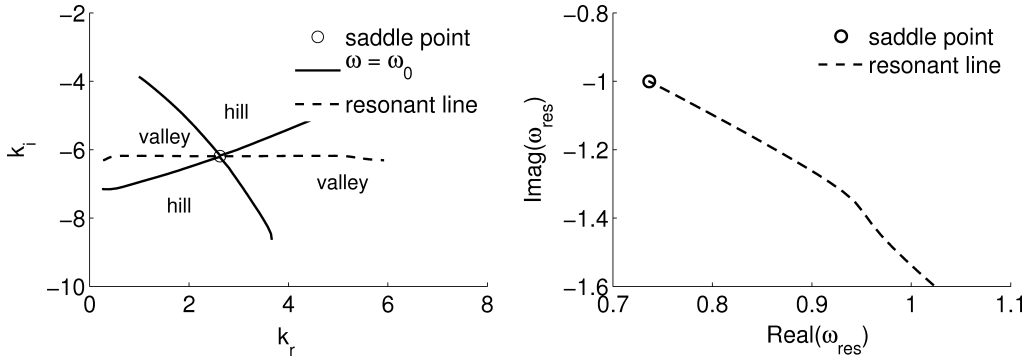

Figure 6.8: The saddle point and the resonant modes for $m = -2$ for the base flow shown in figure 6.2, near the inlet at $x = 0.5273$. The figure on the left shows the saddle point (circle), the local angular frequency, ω_0 (solid line), and resonant modes (dashed line) in the complex k-plane. The figure on the right shows the growth rate, $\mathrm{Im}(\omega_{res})$, and frequency, $\mathrm{Re}(\omega_{res})$, of the resonant modes relative to the saddle point. The saddle point is not absolutely unstable and the resonant modes (right) are never more unstable than the saddle point.

and tracked the leading and trailing edges of the wavepacket. The found that the trailing edge of the wavepacket had a negative group velocity and thus concluded that the profile was linearly absolutely unstable.

A local stability analysis is performed on the flow in figure 6.2 in order to confirm whether the flow is locally absolutely unstable anywhere. In contrast to Gallaire & Chomaz (2003), who calculated the linear impulse response, the local stability analysis presented here finds the saddle points of the local angular frequency, ω, in the complex k-plane. The local absolute growth rate is shown in figure 6.7 up to $x = 20.0$. In contrast to the results of Gallaire & Chomaz (2003), the local stability analysis performed here shows that that the flow is never absolutely unstable.

In a study on the local stability of a lifted diffusion flame, Nichols *et al.* (2009) showed that streamwise confinement can have a destabilizing effect, through beating between resonant modes. Figure 6.8(left) shows the saddle point for a streamwise location near the inlet at $x = 0.5273$. It is not absolutely unstable ($\omega_{0,i} = -1.00$). The dashed line is the resonant line (calculated in the same way as in (Nichols *et al.*, 2009)). It extends only into the valleys, and therefore, the resonant modes all have more negative growth rate than the saddle point (right frame). This confirms that resonant modes are not responsible for the unstable modes in figure 6.3.

Figure 6.9 shows the amplitude of the wave packet from the linear impulse response in figure 6.5(b) at the location of the impulse, $x = 1.0$, and just downstream of the inlet, $x = 0.05$, over time. The amplitude at the impulse location decreases rapidly, then increases slightly, then decreases again. Near the inlet, the amplitude increases and then decreases. The discrepancy between our results and those obtained by Gallaire & Chomaz (2003) could possibly be related to the increase observed at intermediate times. Figure 13 of their study shows the impulse response for $18 \leq t \leq 30$. In our nondimensionalization, this corresponds to $9 \leq t \leq 15$. In figure 6.9(b), the amplitude near the inlet does increase slightly. For longer times, though, the amplitude

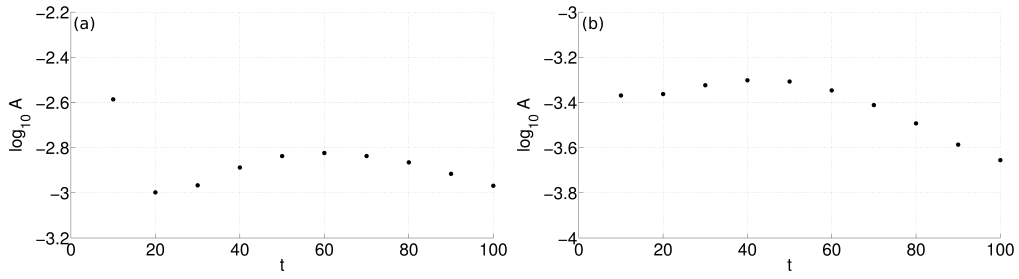

Figure 6.9: The amplitude of the wavepacket for $m = 2$ of the Billant Jet before vortex breakdown at $Re = 667$ and $q = 1.48$. at (a) $x = 1.0$, and (b) $x = 0.05$. The amplitude of the wavepacket is plotted against time for $10 \leq t \leq 100$. The impulse was localized at $(x_0, r_0) = (1.0, 0.5)$.

decreases.

The results in this section show that the double-helical mode observed before vortex breakdown is not due to linear global instability or local absolute instability. The large convective growth suggests that transient growth, related to the highly non-normal linear operator, may be responsible for this mode. This would agree with observations by Billant *et al.* (1998) that this mode is highly sensitive to the experimental set up and the flow conditions. Transient growth calculations for this flow, however, are out of the scope of this thesis, but can be pursued in future work.

6.4 Bubble state

At higher values of the inlet swirl parameter, q, a stagnation point forms along the jet centreline, leading to an axisymmetric bubble in the jet. A grid with 255×257 points for a domain measuring 20.0×20.0 in the radial and axial directions is used. A steady base flow is obtained for $Re = 437$ and $q = 2.10$ by time-stepping the axisymmetric equations of motion. The streamlines of this steady base flow are shown in figure 6.10(a).

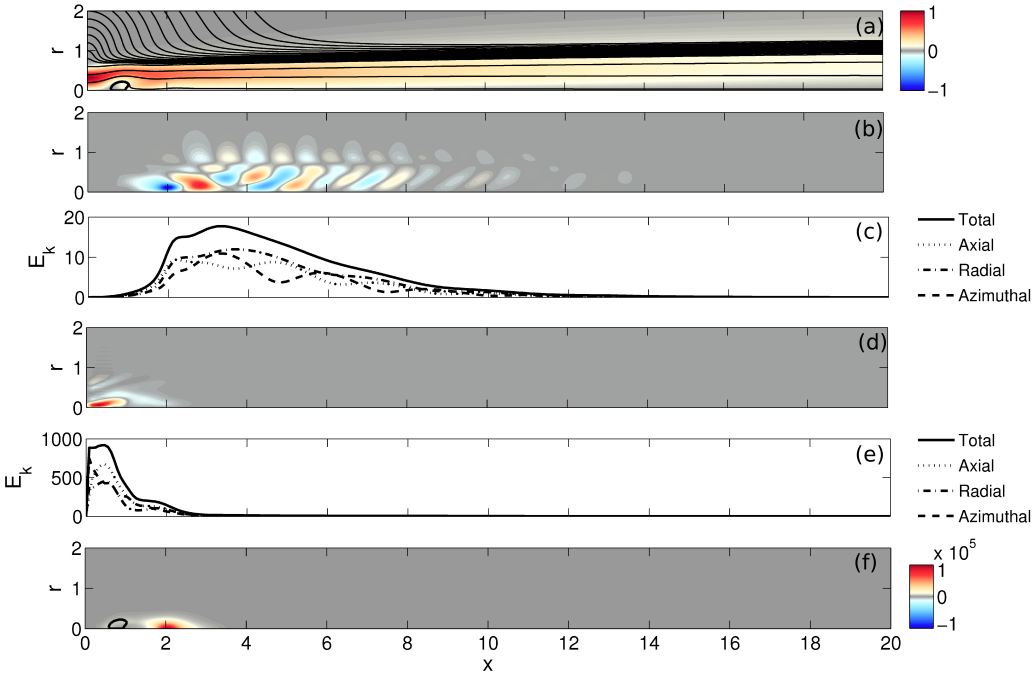

Figure 6.10: (a) The steady base flow, and, for $m = -1$, the unstable (b)-(c) direct, (d)-(e) adjoint global modes, and (f) structural sensitivity for the bubble state in a Billant jet at $Re = 437$ and $q = 2.10$.

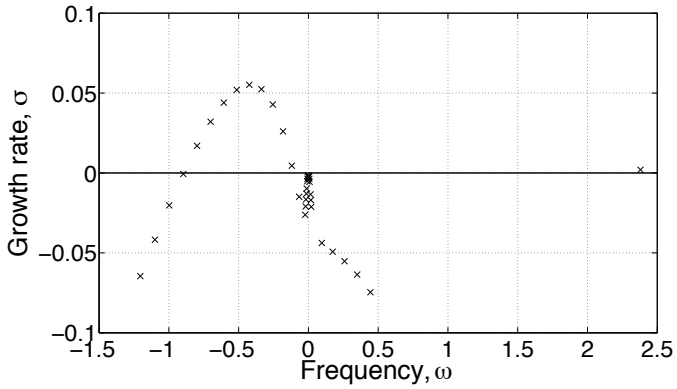

Figure 6.11: Eigenvalue spectrum for $|m| = 1$ for the bubble state in a Billant jet at $Re = 437$ and $q = 2.10$. The 36 least stable modes are shown. Modes with $\omega < 0$ correspond to $m = +1$, while modes with $\omega > 0$ correspond to $m = -1$.

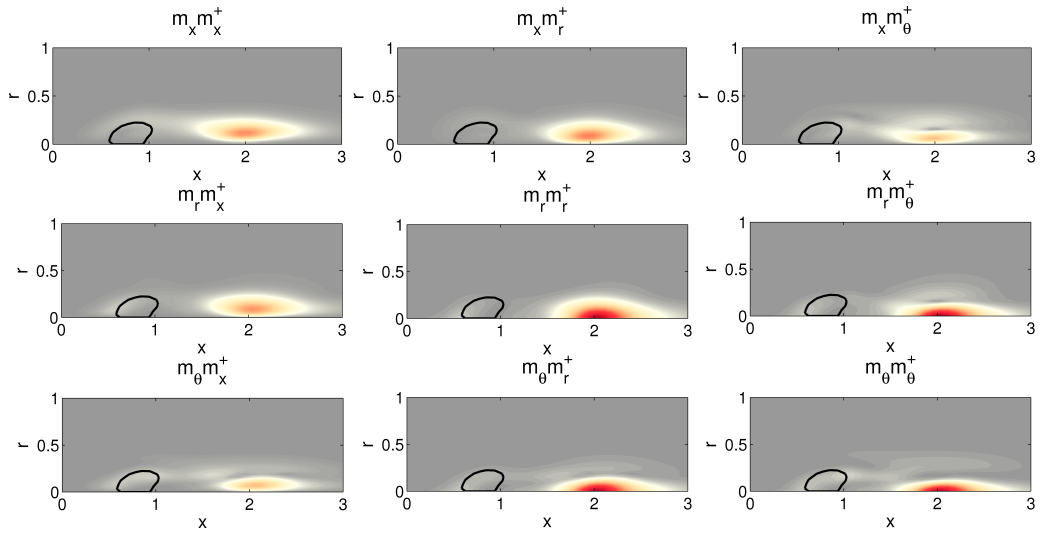

Figure 6.12: The components of the structural sensitivity tensor for the unstable $m = -1$ mode of a Billant jet at $Re = 437$ and $q = 2.10$.

6.4.1 Global stability and structural sensitivity

The evolution of small perturbations of wavenumber $m = -1$ around this steady base flow are considered. Figure 6.11 shows the eigenvalue spectrum that is obtained for this flow configuration. A hoop of unstable modes with negative imaginary parts is found, similar to that observed in the previous section. These modes corresponded to modes of wavenumber $m = +1$, have maximum amplitude at the outlet, and grow exponentially over several orders of magnitude between the inlet and outlet. These modes are convectively unstable modes, dependent on the position of the outlet boundary.

One unstable mode is also found corresponding to $m = -1$. This mode is a true physical global mode of the unconfined flow. This is confirmed by using a numerical sponge layer between $x = 15.0$ and the outlet at $x = 20.0$. This sponge layer reduces the amplitude of perturbations smoothly down to zero at the outlet. A Dirichlet boundary condition can then be used at the outlet instead of a convective boundary condition. Using this procedure, only one mode with $m = -1$ is found that is marginally unstable. The validity

of this mode is checked by varying the damping ratio of the sponge and checking that there is no change in the eigenvalue. This has an eigenvalue of $\lambda = 0.002 + 2.38\mathrm{i}$. The real part of the axial momentum of this global mode is shown in figure 6.10(b), and the amplitude of the global mode is plotted in figure 6.10 (c). The mode reaches maximum amplitude around 3.5 jet diameters downstream of the exit plane, and has large amplitudes inside the jet region and small amplitudes outside it. The corresponding adjoint global mode is shown in figure 6.10(d). The adjoint mode has maximum amplitude upstream of the bubble, near the jet centreline. The structural sensitivity has largest magnitude in the wake of the bubble, around 2 jet diameters downstream of the exit plane. This region corresponds to a local minimum of the centreline axial velocity. This is a sign that a second bubble may form here, downstream of the primary bubble, at higher values of q and Re. The structural sensitivity tensor, shown in figure 6.12, shows that, just as for the $m = -1$ mode in the Grabowski profile, feedback between the radial and azimuthal components of perturbation momentum are the most influential in determining the stability of this mode. This corresponds to conservation of angular momentum in the wake of the bubble.

6.4.2 Sensitivity to a control force

The sensitivity of the eigenvalue to steady forcing is shown in figure 6.13. As expected, a steady force in the wavemaker region, around $x = 2.0$, has a strong effect on both the growth rate and frequency of the global mode. The eigenvalue is most sensitive to a steady axial force. Upstream of the bubble, this has a stronger effect on the frequency than on the growth rate. Around the wavemaker region, both the growth rate and frequency are equally affected. The alternating regions of sensitivity downstream of the bubble correspond to alternating regions of acceleration and deceleration around the local minimum of the axial velocity. It is interesting to note that the sensitivity maps are not related to the streamline pattern around the jet, in contrast to the low-density jet considered in chapter 4.

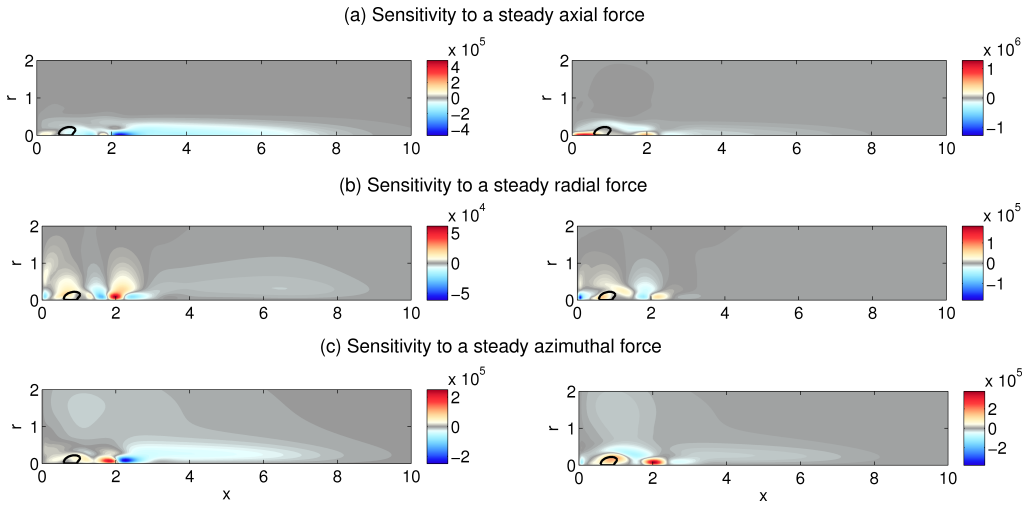

Figure 6.13: The sensitivity of the marginally unstable eigenvalue of the $m = -1$ mode of the bubble state at $q = 2.10$ and $Re = 437$ to steady forcing, $\nabla_{\bar{\mathbf{F}}}\lambda$. The colours show the sensitivity of the growth rate (left), and frequency (right).

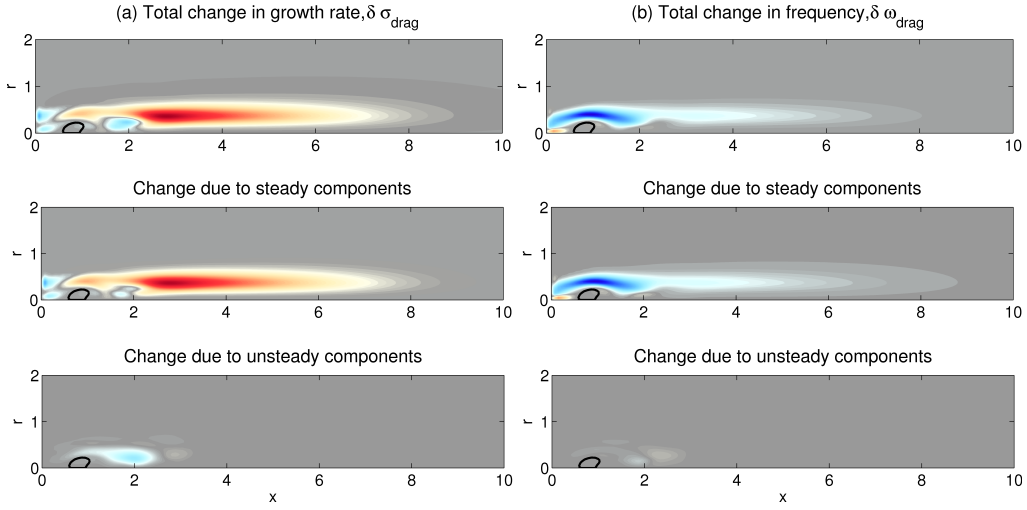

Figure 6.14: The predicted change (scaled by $C_D d_w$) in the marginally unstable eigenvalue of the $m = -1$ mode of the bubble state at $q = 2.10$ and $Re = 437$ due to the drag on a thin axisymmetric control ring, $\delta\lambda_{drag}$. The shading on the plots is equal and goes, for (a) the change in growth rate (left), from -0.0164 (blue) to 0.0164 (red), and for (b) the change in frequency (right), from -0.0545 (blue) to 0.0545 (red).

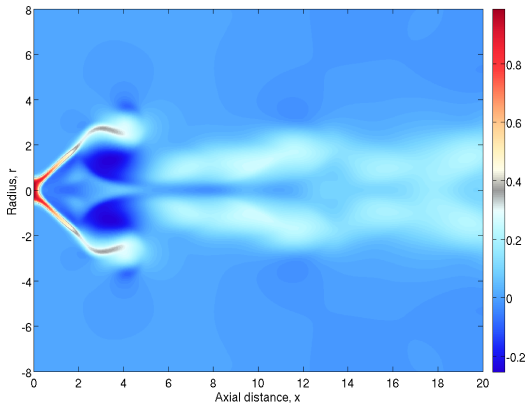

Figure 6.15: A snapshot of the cone state of vortex breakdown in a Billant jet at $Re = 500$ and $q = 2.30$. The colours show the axial momentum of the flow.

These sensitivity maps are used to model the effect of the drag a thin axisymmetric control ring on the unstable eigenvalue, as in section 4.5.1. The predicted change in the growth rate and frequency are shown in figure 6.14. This figure is qualitatively similar to figure 5.18 for the Grabowski profile. There is a region near the inlet where the control ring will have a stabilizing effect.

6.5 Cone state

The bubble state was only found to exist for a small range of parameters. For small increases in q and similar proportional increases in Re, a cone state of vortex breakdown is observed. This cone state is shown in figure 6.15, which is a snapshot of the axial momentum field at $Re = 500$ and $q = 2.30$. This state is axisymmetrically unsteady and a steady axisymmetric base flow could not be obtained by simply time-stepping the axisymmetric equations of motion. Instead, selective frequency damping (SFD) was used to filter out the unsteady temporal fluctuations in the velocity and obtain a steady axisymmetric base flow. A grid with 255×257 points is used for a domain measuring 20.0×20.0 jet diameters in the radial and axial directions

respectively. The steady base flow is shown in figure 6.16(a) and has two breakdown bubbles. It should be emphasized that this steady base flow is an artificial state and will not exist in practice. Ideally, we would like to carry out our analysis around the cone state, but for this thesis, we content ourselves with considering this steady base flow.

6.5.1 Global stability and structural sensitivity

The eigenvalue spectrum, shown in figure 6.17, is similar to that obtained for the bubble state. As for the bubble state, a sponge layer is used at the outlet to damp out the hoop of convective $m = +1$ modes. It is important to point out that the steady base flow was not found to be linearly globally unstable to $m = 0$, even though SFD had to be used to obtain the steady base flow. This suggests that the cone state does not arise out of linear instability of the bubble state.

The most unstable global mode has an eigenvalue of $\lambda = 0.151 + 2.37\mathrm{i}$. The results of the global stability analysis are shown in figure 6.16. The direct and adjoint global modes are very similar to the ones seen for the bubble state. The wavemaker region is just upstream of the 2nd breakdown bubble. The maximum structural sensitivity is greater than that observed for the bubble state, which suggests that the linear operator is more non-normal for this flow than for the flow in figure 6.10.

6.5.2 Sensitivity to a control force

The sensitivity of the eigenvalue to steady forcing is shown in figure 6.18. The eigenvalue is most sensitive to a steady axial force in the region upstream of both breakdown bubbles in the steady base flow. For practical purposes, the region upstream of the first breakdown bubble is of most interest. In this region, both the growth rate and frquency can be controlled effectively. For example, figure ref shows the effect of the drag from a control ring on the eigenvalue. The stabilizing regions are strongest near the second recircula-

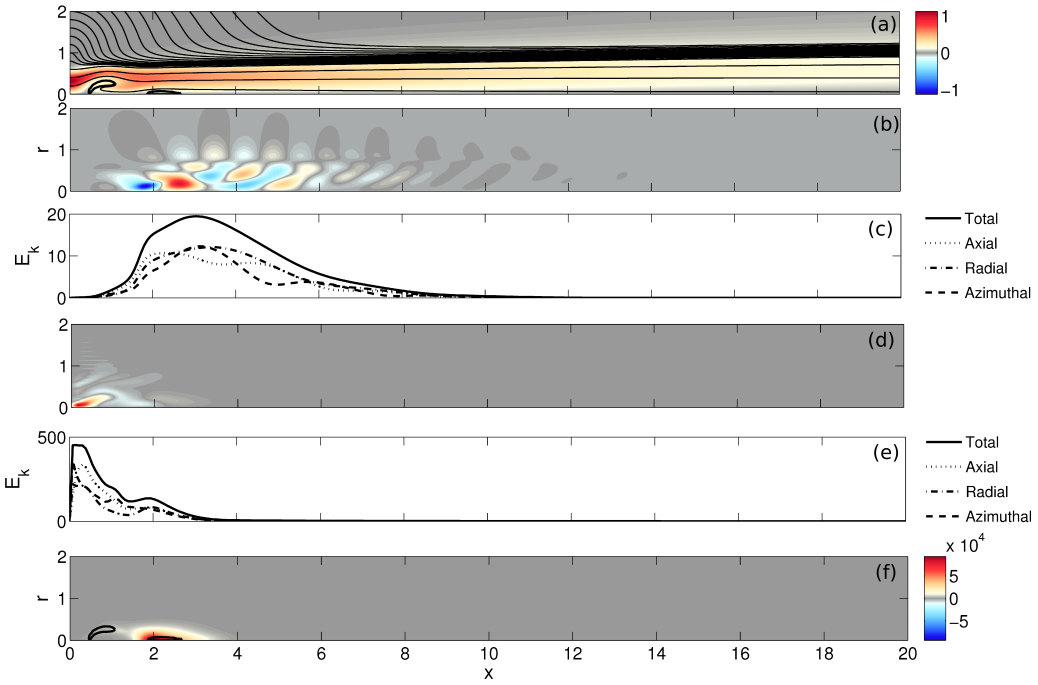

Figure 6.16: (a) The steady base flow, and, for $m = -1$, the (b)-(c) direct, and (d)-(e) adjoint global modes, and (f) structural sensitivity for the cone state in a Billant jet at $Re = 500$ and $q = 2.30$.

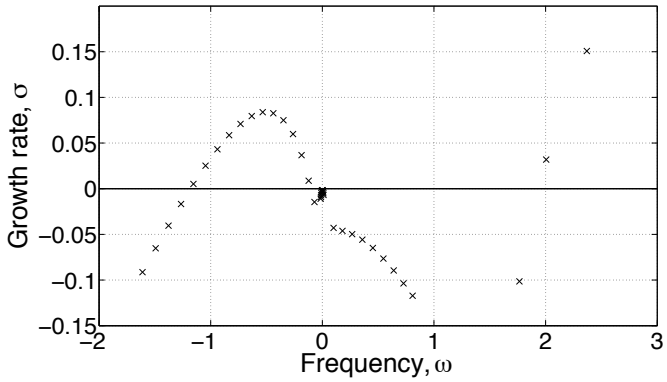

Figure 6.17: Eigenvalue spectrum for $|m| = 1$ for the cone state in a Billant jet at $Re = 500$ and $q = 2.30$. The 40 least stable modes are shown. Modes with $\omega < 0$ correspond to $m = +1$, while modes with $\omega > 0$ correspond to $m = -1$.

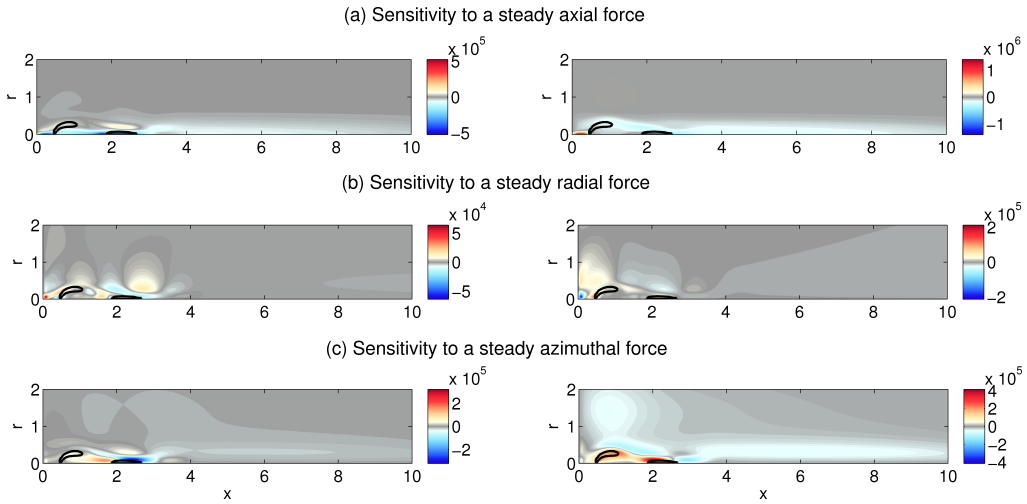

Figure 6.18: The sensitivity of the marginally unstable eigenvalue of the $m = -1$ mode of the cone state at $q = 2.30$ and $Re = 500$ to steady forcing, $\nabla_{\bar{\mathbf{F}}}\lambda$. The colours show the sensitivity of the growth rate (left), and frequency (right).

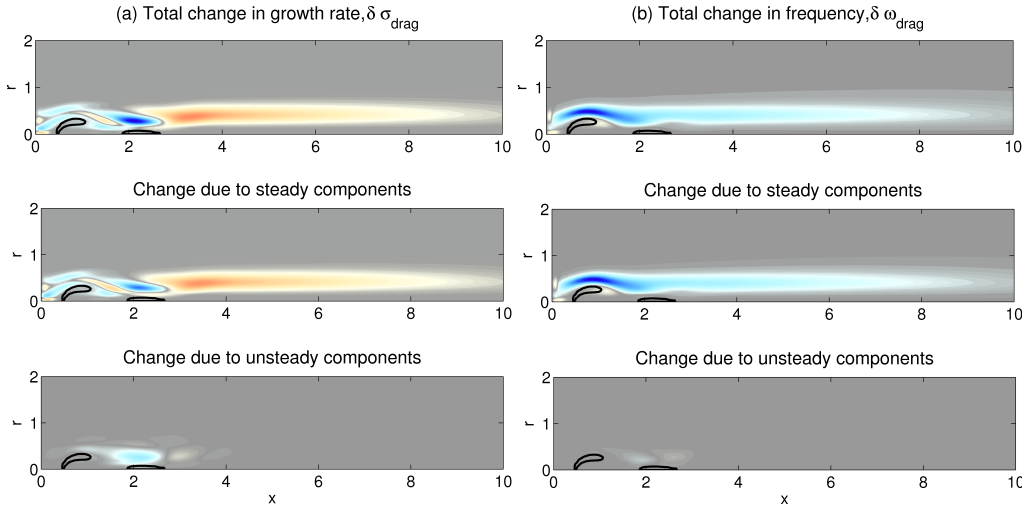

Figure 6.19: The predicted change (scaled by $C_D d_w$) in the marginally unstable eigenvalue of the $m = -1$ mode of the cone state at $q = 2.30$ and $Re = 500$ due to the drag on a thin axisymmetric control ring, $\delta\lambda_{drag}$. The shading on the plots is equal and goes, for (a) the change in growth rate (left), from -0.0188 (blue) to 0.0188 (red), and for (b) the change in frequency (right), from -0.1065 (blue) to 0.1065 (red).

tion bubble, but moderately stabilizing regions are also present upstream of the first recirculation bubble.

6.6 The effect of variable-density and heat addition

In many applications, the swirling jet may have a different density to that of the surrounding fluid. This section considers the effect of this difference in density on the sensitivity maps for the $m = -1$ mode of instability.

The governing equations are discretized on a grid with 255×257 points for a domain measuring 20.0×15.0 in the radial and axial directions respectively. A steady base flow is obtained using SFD, setting $S_1 = 2.0$, $Re = 400$ and $q = 2.20$. The density ratio is similar to the density ratio of methane in air. The base flow and linear global stability results are almost identical to the results in figure 6.10. The wavemaker is located in the wake of the breakdown bubble.

The sensitivity to steady forcing and heat addition is shown in figure 6.20. The sensitivity to momentum forcing (a-c) is similar to that for the uniform-density jet in figure 6.13. The sensitivity to heat addition (d) shows that heat addition upstream of the breakdown bubble, near the inlet, is stabilizing. The stabilizing effect of the drag from a thin control ring near the inlet can, therefore, be enhanced by heating the wire.

6.7 Summary

This chapter has looked at the global stability and control of swirling jets whose velocity profiles match experimental measurements of velocities near the exit plane of a swirling jet Billant *et al.* (1998). At swirl levels below the

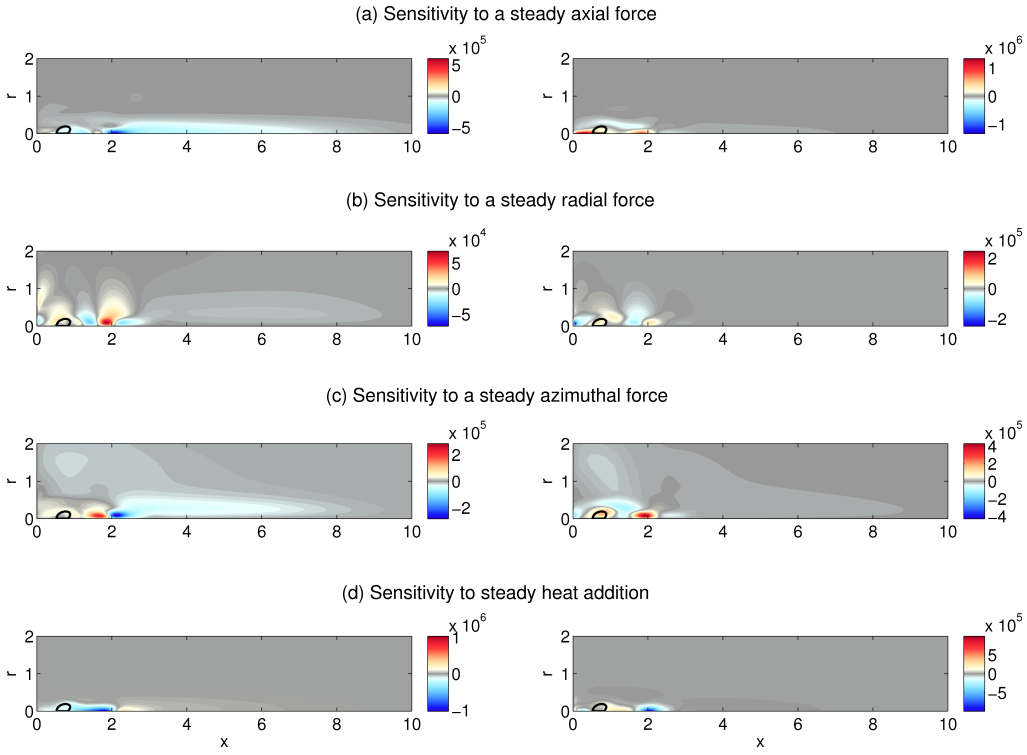

Figure 6.20: The sensitivity of the marginally unstable eigenvalue of the $m = -1$ mode of the bubble state in a low-density Billant jet, with $S_1 = 2.0$ at $q = 2.20$ and $Re = 400$ to steady forcing, $\nabla_{\bar{\mathbf{F}}}\lambda$. The colours show the sensitivity of the growth rate (left), and frequency (right).

onset of vortex breakdown, experiments by Billant *et al.* (1998) and Liang & Maxworthy (2005) have shown that the swirling jet takes the form of a double-helix, which has $m = 2$. A previous study by Gallaire & Chomaz (2003) found that this swirling jet profile was absolutely unstable for $m = -2$ and suggested that the double-helical mode observed in the experiments was a global mode. This hypothesis has been tested in this chapter using a linear global stability analysis around a steady base flow. Several unstable modes with $m = 2$ are found, but these modes reach maximum amplitude near the outlet boundary and show large convective growth. The linear impulse response for $m = 2$ shows the wavepacket convecting downstream. The energy at the site of the impulse grows for a short period of time, but then decays. A local stability analysis has also been performed around a steady base flow, revealing that, in contrast to the results of Gallaire & Chomaz (2003), the flow is not absolutely unstable anywhere for $m = 2$ or $m = -2$. These results show that the $m = 2$ mode is linearly globally stable and locally convectively unstable everywhere. The large convective growth and strong non-normality suggest that transient growth may explain the experimental observations.

At swirl levels above the onset of vortex breakdown, two states of vortex breakdown are observed. In the first state, a steady axisymmetric bubble forms in the flow. In the second state, an unsteady axisymmetric cone forms in the flow. Both these states of vortex breakdown have been observed by Billant *et al.* (1998). A steady base flow is obtained for both these states. The steady base flow for the cone state has two recirculation bubbles. These steady base flows are linearly globally unstable for $m = -1$, similar to the Grabowski profile in the previous chapter. In the bubble state, in contrast to the previous chapter, the wavemaker is located in the wake of the breakdown bubble. In the cone state, the wavemaker is located just upstream of the second recirculation bubble.

The sensitivity of the growth rate and frequency of the global modes in the bubble state and cone state to a control force has also been considered. The growth rate and frequency are most sensitive to a steady axial force

in the region upstream of the breakdown bubble. The sensitivity maps are qualitatively similar to those obtained for the Grabowski profile in chapter 5 and do not depend on the streamline pattern around the jet. These maps have been used to predict the influence of the drag from a thin axisymmetric control ring on the growth rate and frequency of the global mode. For both the bubble state and the cone state, the ring has most influence when placed in the wavemaker region and influences the frequency more than the growth rate. For both these states, however, there are regions near the inlet where the ring is moderately stabilizing. This stabilizing effect is enhanced in a low-density swirling jet by heating the ring.

7

Global stability and control of a lifted jet diffusion flame

This chapter revisits the lifted jet diffusion flame that was originally considered by Chandler (2010). A linear global stability analysis is used to study the origin of the modes of instability, and their possible control. The results of this linear global stability analysis are used to explain the nonlinear behaviour observed in these flames. The local stability analysis and resonant mode calculations have been performed by Matthew Juniper.

7.1 Introduction

A diffusion flame is a type of flame that forms when the fuel and oxidizer are not mixed before ignition. The fuel and oxidizer mix by diffusion and the reaction rate is greatest where the fuel and oxidizer are in stoichiometric proportion. In this thesis, the case considered is that of a jet of fuel exiting into a supply of oxidizer and being ignited. In this configuration, when the flow rate of fuel is too large, the flame lifts off the jet nozzle and stabilizes at some distance downstream of the jet exit plane. The region between the exit plane and the flame base is referred to as the premixing zone.

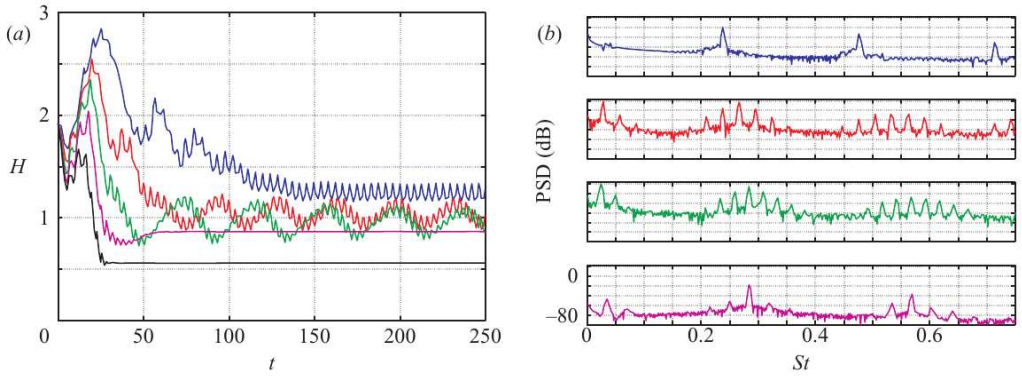

Figure 7.1: Taken from Nichols & Schmid (2008) (a) Time histories of the lift-off height, H, for five reacting simulations with $Da = 3, 4, 5, 6, 7 \times 10^5$ represented by blue, red, green, magenta, and black, respectively. (b) PSD vs Stouhal number for four of the signals displayed in (a).

Downstream of the premixing zone, the flame changes the density profile of the jet. If the jet of fuel exits upwards, buoyancy leads to changes in the velocity profile. In particular, the velocity profile gains additional inflexion points. These can lead to global instability through the Kelvin-Helmholtz mechanism. In this thesis, however, the effects of buoyancy are neglected.

Nichols & Schmid (2008) carried out direct numerical simulations of non-buoyant flames in reacting low-density jets. By varying the Damkohler number, Da, flames with different lift-off heights were obtained. Flames with sufficiently large lift-off heights were found to be unstable - the flame base oscillated around a mean axial position and the stoichiometric surface developed folds. For a range of Damkohler numbers, the axial location of the flame base was monitored over time, and an FFT of this time trace was used to obtain spectra for flames with different mean lift-off heights. The results (shown in figure 7.1 for reference) show that increasing the Damkohler number reduces the flame lift-off height. Flames with smaller lift-off heights (higher Da) have less sharp spectral peaks than flames with larger lift-off heights (lower Da). For the unstable flames at $Da = 400,000$ and $Da = 500,000$, and the marginally unstable flame at $Da = 600,000$ there is a peak at around $0.25 < St < 0.30$ (with harmonics) and another peak at around

$0.0 < St < 0.05$. For sufficiently small lift-off heights ($Da = 700,000$), the flame is steady and no oscillations are observed. Nichols & Schmid (2008) performed a local stability analysis around steady solutions for these lifted flames and showed that the premixing region upstream of the flame base is locally absolutely unstable and that reducing the lift-off height shortens the region of absolute instability. Since the flame with smallest lift-off height is stable, they concluded that the flame itself cannot support self-sustained oscillations and that flame oscillations for the unstable cases must be caused by the absolutely unstable premixing zone.

Chandler (2010) performed a linear global stability analysis around the marginally stable case ($Da = 600,000$) in Nichols *et. al.*'s simulations and found an unstable mode whose frequency was within 10% of the spectral peak at $St = 0.284$ observed in the nonlinear simulations. Chandler (2010) found that the structural sensitivity of this mode is maximum in the shear-layer in the premixing zone. This confirmed the hypothesis of Nichols & Schmid (2008) that the strong spectral peak observed at $St = 0.284$ in their simulations was due to global instability caused by the non-reacting low-density jet upstream of the flame base.

In a a subsequent study, Nichols *et al.* (2009) used a local stability analysis to show that the flame base imposes streamwise confinement on the jet in the premixing zone. They showed that this streamwise confinement can lead to low-frequency resonant modes being set up and suggested that the nonlinear interaction of those resonant modes with the jet mode of instability could cause the spectral peaks at $0 < St < 0.05$ observed in the nonlinear simulations.

In this chapter, a linear global stability analysis is used to show that the spectral peaks at $0 < St < 0.05$ are caused by an unstable global mode and not by resonant modes. This is supported by a local stability analysis that calculates the resonant modes and shows that the predicted frequencies of the resonant modes do not match the frequencies observed in the nonlinear

simulations. The structural sensitivity of the unstable global mode is found to be maximum in the flame, suggesting that, in contrast to Nichols *et al*'s conclusion, the flame itself does support self-sustained oscillations.

Finally, the sensitivity of both the global modes to steady forcing is obtained. This provides information about how the growth rates and frequencies of these modes may be controlled.

7.2 Flow configuration

An axisymmetric jet of fuel exits into a large cylindrical domain, of length X_{max} and radius R_{max}, that is filled with oxidizer. The flow variables are nondimensionalized by the jet diameter, jet axial velocity and ambient density. The nondimensional flow parameters are set to match exactly the cases studied in the nonlinear simulations of Nichols & Schmid (2008). The ratio of the ambient density to jet density at the inlet defines the density ratio parameter, $S_1 = 7.0$. The Reynolds number, $Re = 1000$, is defined in terms of the jet diameter, jet axial velocity and jet density. The Prandtl number, $Pr = 0.7$, and Schmidt number, $Sc = 0.7$, describe the ratio of the diffusivity of temperature and mass, respectively to the diffusivity of momentum.

The ratio of the adiabatic flame temperature to the ambient temperature defines the temperature ratio parameter $S_2 = 6.0$. The reaction chemistry is described by the mass stoichiometric ratio, $s = 2$, the equilibrium constant, $\kappa = 0.01$, the heat release parameter, $\alpha = 0.833$, and the Zeldovich number $\beta = 3$. As noted by Nichols & Schmid (2008), this choice of parameters produces flames that are thicker than those found in nature. This is acceptable as these flames are sufficiently thin in comparison to the wavelength of the hydrodynamic instabilities that are being investigated. This is particularly relevant if the wavemaker region is in the flame, as it is for mode B (figure 7.6). In this case, it is important that the thickness of the flame relative to the thickness of the wavemaker region is checked *a posteriori*.

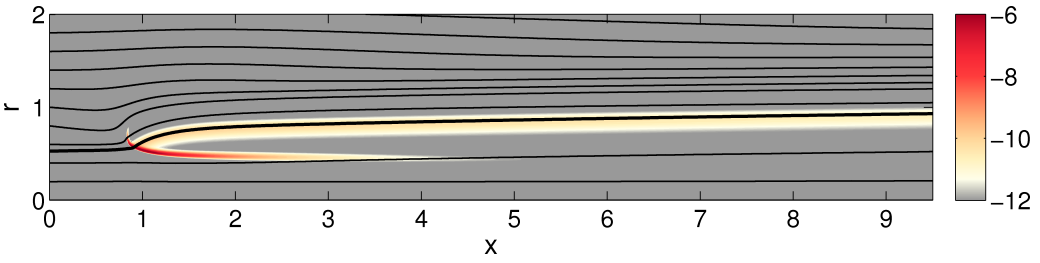

Figure 7.2: The steady baseflow for a lifted diffusion flame at $Re = 1000$ and $Da = 600,000$. The streamlines show the axial and radial velocity and the colour shows contours of reaction rate, $\log(\bar{\omega})$. The thick black line shows the stoichiometric surface, which corresponds to a contour of $\bar{Z} = 0.333$.

The equations are discretized on a grid with 511×1025 points for a domain measuring 10.0×10.0 jet diameters in the radial and axial directions respectively. At the inlet, the velocity and mixture fraction profiles used by Nichols & Schmid (2008) are imposed. These top-hat profiles are formed from Michalke's profile number two, with a small coflow of oxidizer surrounding the jet. The coflow velocity is 1% of the jet velocity. The temperature profile at the inlet is set to be uniform but a Gaussian-shaped impulse at $(x, r) = (2.0, 0.5)$ is applied to ignite the fuel-oxidizer mixture in order to obtain the base flow.

A steady base flow was obtained for a Damkohler number $Da = 600,000$ by Chandler (2010) using SFD. This steady lifted diffusion flame is shown in figure 7.2. This matches the flame found in Nichols & Schmid (2008).

7.3 Global stability and structural sensitivity

The global stability of this steady base flow is studied for perturbations with $m = 0$. Figure 7.3 shows the eigenvalue spectrum obtained. Two families of modes are found that go unstable - a high-frequency branch and a low-frequency branch. The most unstable mode in each of these families are

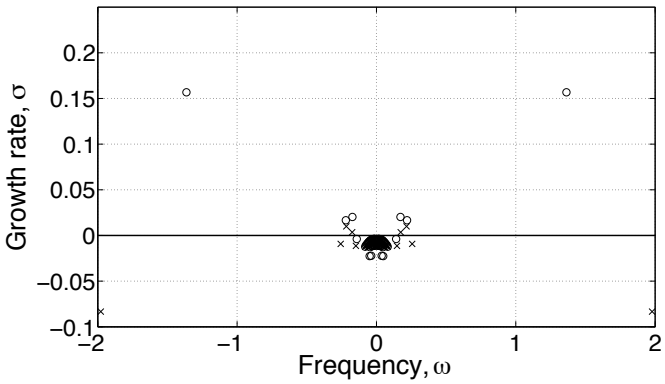

Figure 7.3: Eigenvalue spectrum for $m = 0$ for the flame shown in figure 7.2 at $Da = 600,000$ (crosses), and the same flame calculated at $Da = 500,000$ (circles). The 50 least stable modes are shown.

shown in figures 7.4 and 7.5.

The first of these modes, labelled mode A, has an eigenvalue of $\lambda = -0.0833 + 1.978\text{i}$ at $Da = 600,000$ and was first identified by Chandler (2010). It becomes globally unstable for $500,000 < Da < 600,000$. The real parts of the direct and adjoint global modes for mode A are shown in figure 7.4. The direct mode shape is most dominant downstream of the flame base, and grows radially towards the axis of the jet. The adjoint mode shape, however, is most dominant in the premixing zone between the inlet and the flame base. The Strouhal number is $St = \text{Im}(\lambda)/2\pi = 0.315$, which is within approximately 10% of the nonlinear Strouhal number ($St = 0.284$) observed by Nichols & Schmid (2008) in their nonlinear simulations. This Strouhal number is very close to the Strouhal number corresponding to the global instability of the non-reacting low-density jet in Chapter 4.

The second of these modes, labelled mode B, has an eigenvalue of $\lambda = 0.0098 + 0.216\text{i}$. The real parts of the direct and adjoint global modes for mode B are shown in figure 7.5. In contrast to mode A, the direct mode shape of mode B is localized further downstream, along the outer part of the flame and grows radially away from the axis of the jet. The adjoint mode

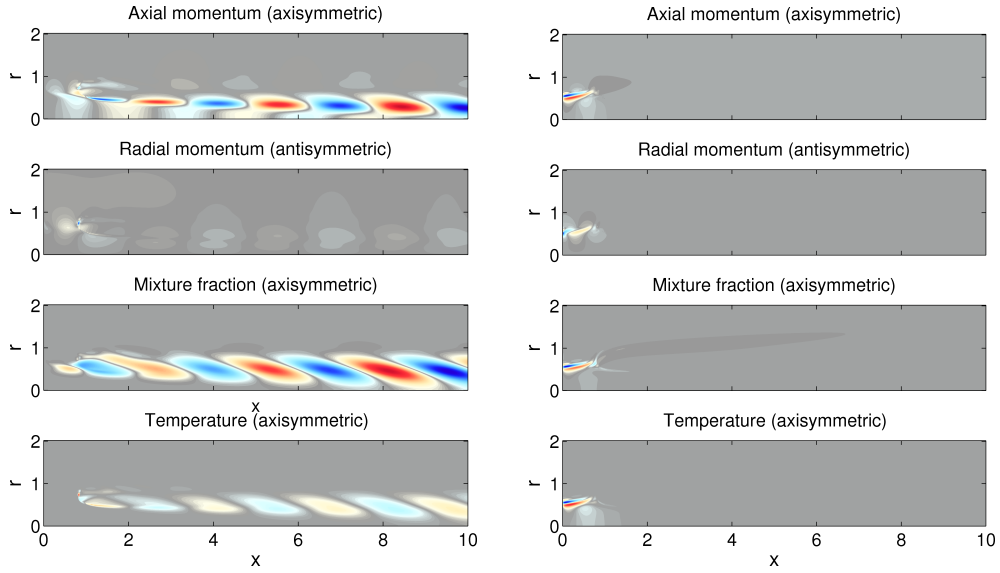

(a) Direct global mode (b) Adjoint global mode

Figure 7.4: The real parts of the direct and adjoint global modes for mode A, with $\lambda = -0.0833 + 1.978\mathrm{i}$

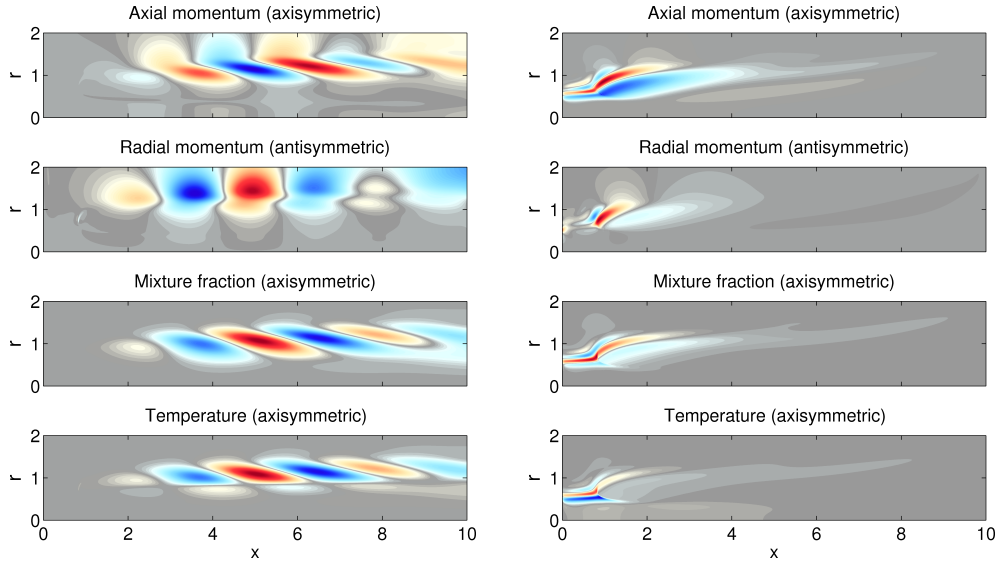

(a) Direct global mode (b) Adjoint global mode

Figure 7.5: The real parts of the direct and adjoint global modes for mode B, with $\lambda = 0.0098 + 0.216\mathrm{i}$

shape is dominant in both the premixing zone as well as just downstream of the flame base. This imaginary part of the eigenvalue corresponds to a Strouhal number of $St = 0.034$, which agrees well with the Strouhal number ($St = 0.035$) of the low-frequency oscillations observed by Nichols & Schmid (2008) in their nonlinear simulations. In recent experiments on buoyant globally unstable methane diffusion flames, Li & Juniper (2012) found that the flames oscillate at around $St = 0.049$. This is not expected to match the results here because buoyancy is neglected in this thesis. Nevertheless, the similar order of magnitude of the Strouhal numbers suggests that mode B may be similar to the global instability that arises in buoyant jet diffusion flames. In Chandler's original study, a local stability analysis around the steady base flow in figure 7.2 found a region of absolute instability in the flame region (§4.5 of Chandler (2010)). Chandler, however, did not find the global mode B, and therefore, concluded that this region of absolute instability in the flame was too weak to cause global instability. The results of this section, however, show that this region of local absolute instability does support a linear global mode.

The structural sensitivity, as defined by Giannetti & Luchini (2007) for the incompressible Navier–Stokes equations in the velocity-pressure formulation, is given by the dyadic product of the direct and adjoint global mode velocity vectors. For the LMN formulation used in this thesis, the equivalent quantity is the dyadic product of the direct and adjoint global mode momentum vectors, $S_{ij} = \hat{\mathbf{m}}_i \hat{\mathbf{m}}_j^+$. The components of this tensor represent the effect of changes in the feedback between the different components of the momentum on the eigenvalue of the global mode. The Frobenius norm of this tensor for modes A and B are shown in figure 7.6. For mode A, this quantity is maximal at $(x, r) = (0.35, 0.58)$, while, for mode B, this quantity is maximal at $(x, r) = (3.27, 1.03)$. According to Giannetti & Luchini (2007), this identifies the region in space which is most sensitive to perturbations in the inherent feedback mechanism driving the instability: the wavemaker region. This means that the wavemaker for mode A lies is the shear layer in the premixing region of the lifted flame, while the wavemaker for mode B lies in the

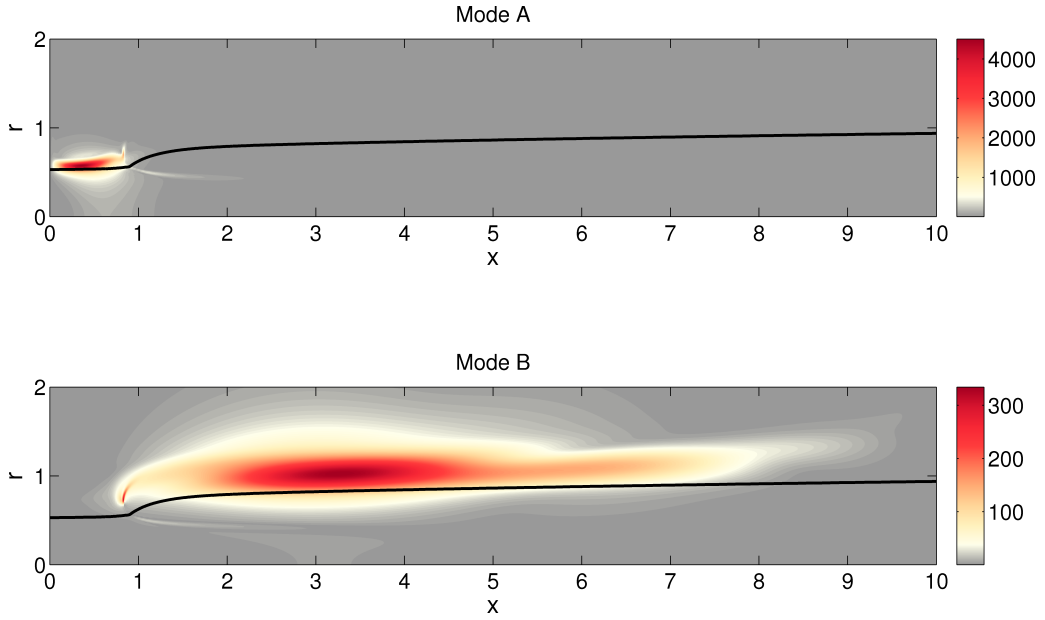

Figure 7.6: The wavemaker, as defined by 2.24 for modes A and B. This is equivalent to the definition of Giannetti & Luchini (2007).

shear layer along the outer surface of the flame. This confirms the conclusion of Nichols & Schmid (2008) that mode A corresponds to the jet imparting its global instability frequency onto the flame but shows that, in contrast to the conclusions of Nichols & Schmid (2008), that the flame can support a self-sustaining mode - mode B corresponds to an an instability of the flame itself.

For variable-density and reacting flows, however, more information about the nature of the instability can be obtained by considering the structural sensitivity for the entire state vector and not just the momentum vector. For the flames in this chapter, this leads to a 4×4 tensor, which represents the effect of changes in the feedback between m_x, m_r, Z and T on the eigenvalue of the global mode. Comparison between sensitivities involving momentum, temperature and mixture fraction are valid as long as the adjoint global mode has been normalized according to 2.21, which is true for the results presented here. The sensitivity tensors for modes A and B are shown in figures 7.7 and 7.8 respectively. For mode A, the eigenvalue is most sensitive at the flame base to changes in the feedback of the temperature into the axial and radial

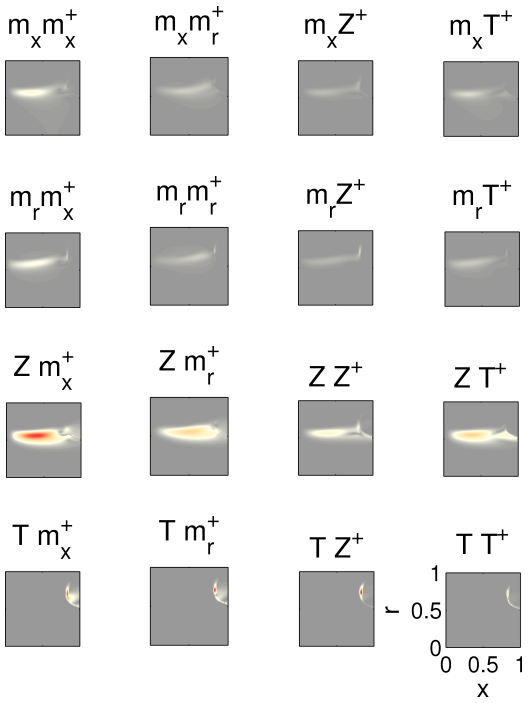

Figure 7.7: The components of the structural sensitivity tensor $\hat{\mathbf{q}}(\hat{\mathbf{q}}^+)^*$ for mode A. The shading on all the plots is equal and goes from 0 (grey) to 24606 (red).

momentum equations. In the shear layer in the premixing zone, changes in the feedback of the mixture fraction into the momentum equations have a moderate effect. The temperature and mixture fraction, however, only affect the momentum equations indirectly through the density. Both these types of feedback, therefore, involve feedback involving the perturbation density and momentum. For mode B, the same feedback mechanism is dominant but in a different location - the outer shear layer of the flame.

7.3.1 Comparison to previous studies

In order to confirm that mode B accounts for the spectral peaks at the low Strouhal number in the nonlinear simulations of Nichols & Schmid (2008), the global modes are calculated for two other values of Damkohler number,

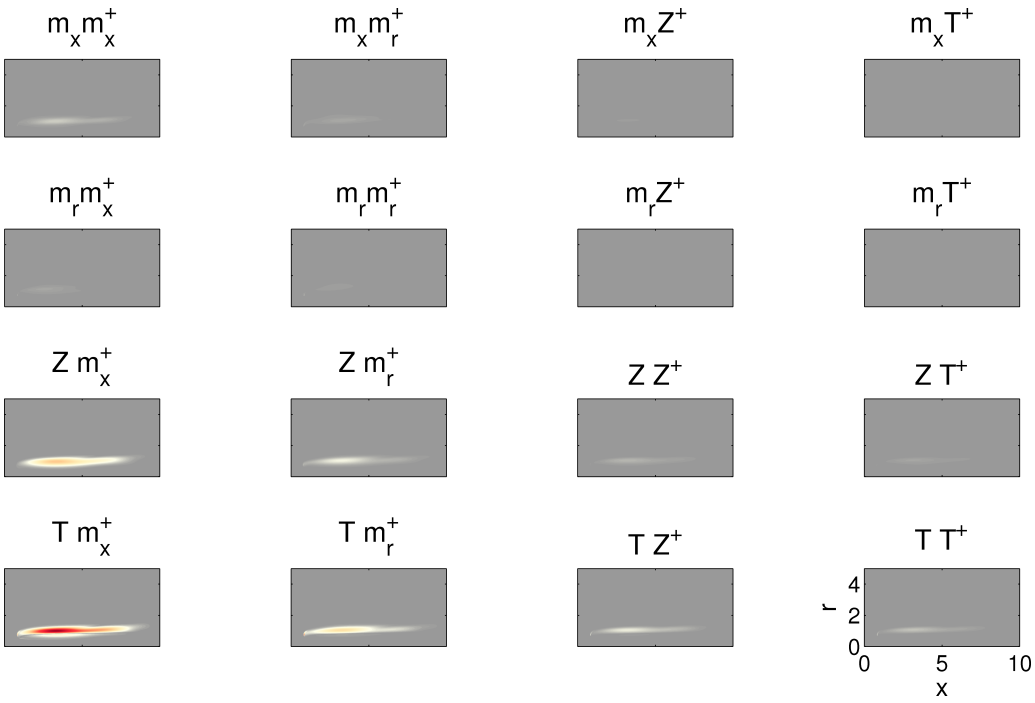

Figure 7.8: The components of the structural sensitivity tensor $\hat{\mathbf{q}}(\hat{\mathbf{q}}^{+})^{*}$ for mode B. The shading on all the plots is equal and goes from 0 (grey) to 5287 (red).

$Da = 500,000$ and $Da = 700,000$. For both cases, the growth rates and frequencies for modes A and B are compared to the spectra obtained by Nichols & Schmid (2008). The results are summarized in tables 7.1 and 7.2.

The linear growth rates for mode A match the observations in the nonlinear DNS which show flames with higher Da being more stable. The agreement between the linear global mode frequency and the nonlinear frequency is better for $Da = 600,000$ than for $Da = 500,000$ because the flame at $Da = 500,000$ is more unstable and is far from the bifurcation point.

The linear growth rates for mode B decrease as Da is increased. This agrees with the results in figure 3 of Nichols & Schmid (2008) which show that the low-frequency spectral peak for $Da = 600,000$ is smaller than the low-frequency spectral peak for $Da = 500,000$. The linear global mode frequencies for mode B agree well with those observed in the nonlinear simulations for $Da = 500,000$ and $Da = 600,000$.

Nichols *et al.* (2009) suggested that the low-frequency oscillations in the nonlinear simulations could be due to beating between resonant modes that arise due to the streamwise confinement that the flame base imposes on the low-density jet in the premixing zone. In order to confirm this theory, resonant mode calculations were performed for the flame with $Da = 500,000$. The results are shown in figure 7.9, at a location $x = 0.0391$, which corresponds to the closest grid slice to the results reported in Nichols *et al.* (2009). This location was used based on the value of k and ω of the saddle point. Figure 7.9(a) shows the saddle point of the local angular frequency at $\omega_0 = 1.05 + 0.281\mathrm{i}$. The solid line shows the line of constant local growth rate, ω_i, that pass through the saddle point, and the dashed line shows the resonant line, which satisfies criteria 1 and 3 in equation (5) of Nichols *et al.* (2009). The solid dots show the resonant modes that are allowed, according to criterion 2 in equation (5) of Nichols *et al.* (2009), for the lift-off height of the flame ($H = 1.913$). The solid dots in figure 7.9(b) show the resonant modes along the resonant line: there are 2 unstable resonant modes, with

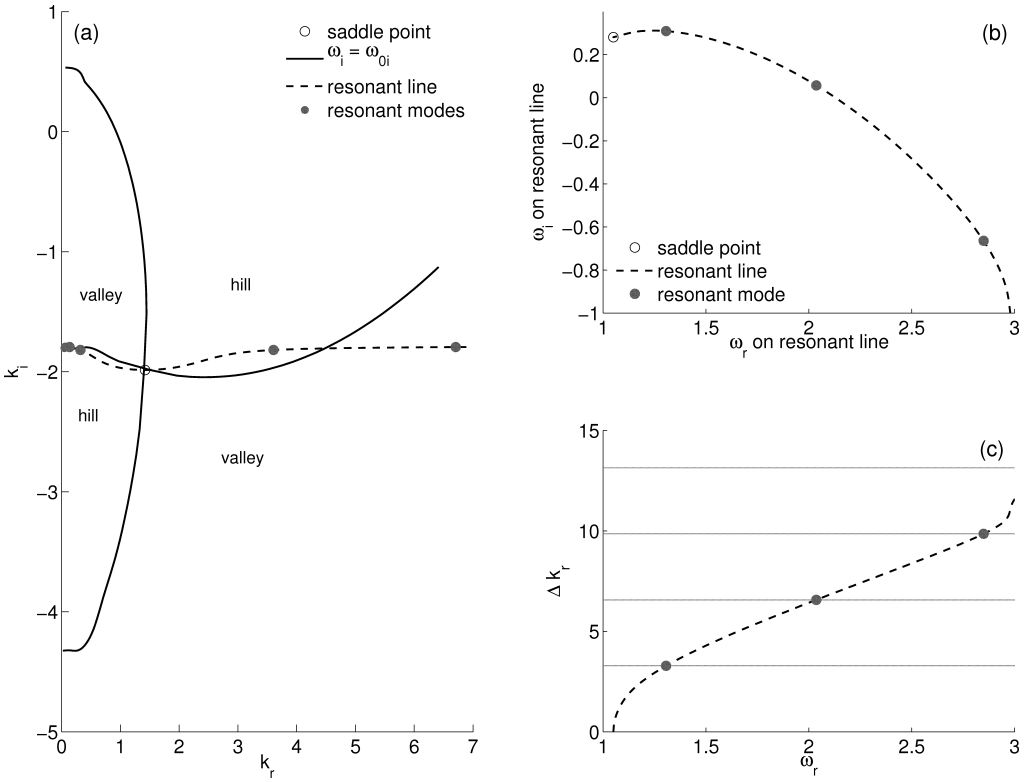

Figure 7.9: The saddle point and resonant modes for a lifted diffusion flame with $Da = 500,000$ at $x = 0.039$ near the inlet. (a) The saddle point (circle), which is at (ω_{0i}, k_{0i}), the lines of constant ω_i that pass through the saddle point (solid lines), and the resonant line (dashed line), with valid resonant modes (solid dots) in the complex k-plane. (b) The growth rate, ω_i, and frequency, ω_r, of the resonant line and modes relative to the saddle point. (c) The resonant line and modes in the $(\omega_r, \Delta k_r)$ plane. The resonant modes (solid dots) are equidistant in the vertical direction. This determines the spacing along the ω_r axis, which is then used in (b).

$\omega_g = 1.31 + 0.31\mathrm{i}$ and $\omega_g = 2.04 + 0.06\mathrm{i}$, and an infinite number of stable resonant modes.

Nichols *et al.* (2009) suggest that the low-frequency mode could be due to beating between the two unstable resonant modes. The difference in frequency between the 2 unstable resonant modes is 0.73, which corresponds to a Strouhal number of $St = 0.12$. This is almost 5 times greater than the frequency in the nonlinear simulations for this Da ($St = 0.025$). Calculating the difference in frequencies between the other stable resonant modes also gives frequencies which are several times larger than the nonlinear frequency. Similar results are obtained for a streamwise location $x = 0.97$, which is roughly half way within the premixing region.

These results show that the low-frequency oscillations observed in the nonlinear simulations are not caused by beating between resonant modes, and support the conclusion that the low-frequency oscillations observed in the simulations of Nichols & Schmid (2008) are caused by a linear global instability, originating in the outer shear layer of the flame. Although the theory of resonant modes put forward by Nichols *et al.* (2009) is valid, it is not responsible for the low-frequency oscillations observed in Nichols *et al.*'s simulations.

7.4 Sensitivity to a control force

In this section, the sensitivity of the growth rate and frequency of modes A and B to steady forces is presented. Figure 7.10 shows the sensitivity of mode A to steady body forces and a steady heat source. As for the low-density jet considered in chapter 4, the sensitivity pattern for mode A of the lifted diffusion flame, in particlar the sensitivity to axial forcing and heat input, roughly follows the streamline pattern in figure 7.2. The eigenvalue is most sensitive to a steady axial force in the lean side of the fuel-oxidizer shear layer upstream of the flame base. A radial force has most effect at the jet

	Linear global stability analysis		Nichols *et al* (2008)
Da	Growth rate σ	Frequency, St	Nonlinear St
$500,000$	0.159	0.217	0.284
$600,000$	-0.083	0.315	0.284
$700,000$	-0.459	0.141	stable

Table 7.1: Comparison of growth rates and frequencies for mode A from a linear global stability analysis with frequencies from table 1 of Nichols & Schmid (2008).

	Linear global stability analysis		Nichols *et al* (2008)
Da	Growth rate σ	Frequency, St	Nonlinear St
$500,000$	0.020	0.027	0.025
$600,000$	0.010	0.034	0.035
$700,000$	-0.010	0.037	stable

Table 7.2: Comparison of growth rates and frequencies for mode B from a linear global stability analysis with the low-frequency oscillations observed in figure 3 of Nichols & Schmid (2008).

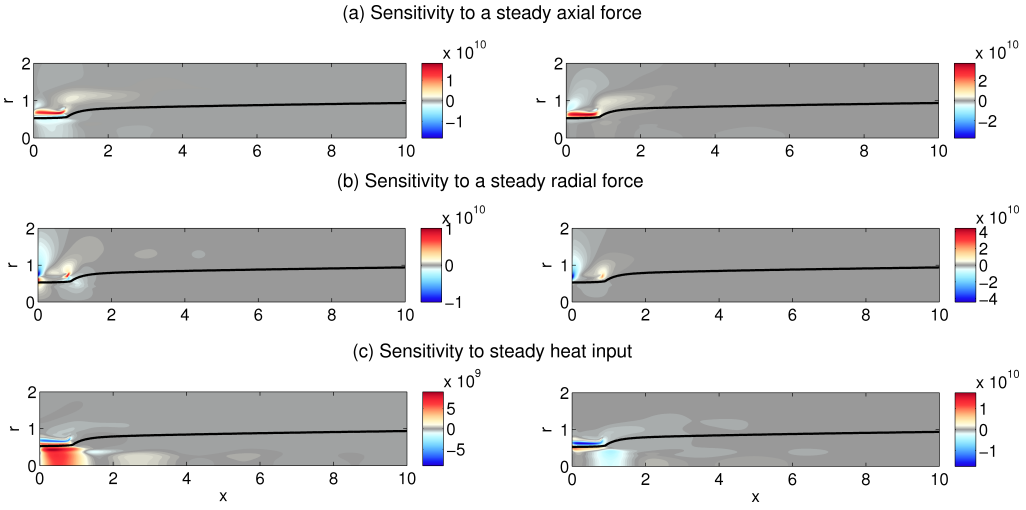

Figure 7.10: The sensitivity of the marginally stable eigenvalue of mode A for the lifted flame in figure 7.2 at $Da = 600,000$, to steady forcing, $\nabla_{\bar{\mathbf{F}}}\lambda$. The colours show the sensitivity of the growth rate (left), and frequency (right).

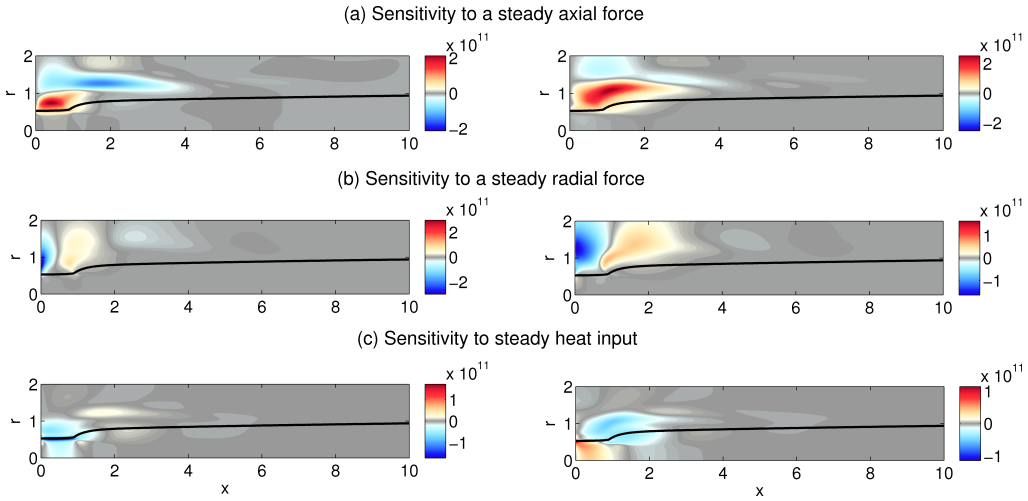

Figure 7.11: The sensitivity of the marginally stable eigenvalue of mode B for the lifted flame in figure 7.2 at $Da = 600,000$, to steady forcing, $\nabla_{\bar{\mathbf{F}}}\lambda$. The colours show the sensitivity of the growth rate (left), and frequency (right).

exit plane and at the flame base. Heating the core of the fuel jet upstream of the flame base is destabilizing. This is similar to the low-density jet in chapter 4. In general, the sensitive regions are concentrated around the jet shear layer and flame base. From a practical point of view, however, it would be difficult to use a control device in these regions because the flame would tend to attach to the control device.

For mode B, on the other hand, regions of moderate to high sensitivity extend up to two jet diameters away from the jet axis and beyond. Passive control of this mode may, therefore, be a feasible option. A previous study by Toong *et al.* (1965) found that the flicker of a diffusion flame on a burning cylinder could be stabilized by placing a non-burning control cylinder on either side of the burning cylinder. From the top frame of figure 7.11, it can be deduced that the drag force from a thin control ring has a strong effect on the eigenvalue: close to the flame it stabilizes mode B, while further from the flame, it destabilizes mode B. The drag force from a control ring also has a equivalently strong effect on the frequency of this mode: close to the flame, it increases the frequency, while further from the flame, it decreases

the frequency. For reference, Toong *et al.* (1965) observed the frequency of oscillations to increase but this is expected to depend on the exact location of the control cylinders. It is interesting that, in contrast to mode A, heating the core of the fuel jet (which may not be feasible), or the flow around the fuel jet just downstream of the exit plane is stabilizing.

It is worth noting that the sensitivity to steady forcing for both modes of the lifted-flame have a very large magnitude ($O(10^{10})$) compared to the sensitivity to steady forcing for the non-reacting flows considered in chapters 4, 5 and 6 ($O(10^5) - O(10^7)$). This high sensitivity is caused by the linearization of the reaction rate around the base flow mixture fraction and temperature profiles. In particular, the eigenvalue is extremely sensitive to changes in the base flow mixture fraction profile. Physically, this means that, a control device affects the growth rate and frequency of the global modes by affecting the base flow mixture fraction profile, which then affects the reaction rate. The high sensitivity also means that even a tiny perturbation will cause a large change in the base flow, making these linear sensitivity maps inaccurate in predicting the magnitude of the change in the eigenvalue. This is because the linear stability analysis is strictly valid only for infinitesimal perturbations. For finite perturbations, the accuracy of the linear analysis can be improved by incrementing the magnitude of the perturbation in stages, calculating a new steady base flow, and performing the linear sensitivity analysis around this new steady base flow at each stage.

7.5 Summary

A linear global stability analysis has been performed around a steady base flow for a lifted diffusion flame with $Da = 600,000$. The flow configuration studied is identical to that considered by Nichols & Schmid (2008) in a previous study. Two modes with $m = 0$ are found to be near the threshold of instability. The direct and adjoint global modes have been calculated for each of these modes. These have been used to identify the wavemaker responsible

for causing each mode and to calculate the sensitivity of the growth rate and frequency of each mode to steady control forces. The results from the linear global stability analysis have been used to identify the modes of instability observed in the nonlinear simulations of Nichols & Schmid (2008).

The first of these modes, labelled mode A, has a linear global frequency which is close to the frequency of the dominant mode observed in Nichols *et al.*'s nonlinear simulations. The wavemaker for this mode is located in the shear-layer in the premixing zone. This confirms that, in agreement with the local stability analysis used by Nichols & Schmid (2008), this mode is caused by instability of the low-density jet upstream of the flame base. The components of the structural sensitivity tensor reveal that the eigenvalue is most sensitive to feedback of the perturbation density into the linearized momentum equations at the flame base.

The second of these modes, labelled mode B, has a linear global frequency which is close to the frequency of the low-frequency oscillations observed in Nichols *et al.*'s nonlinear simulations. The wavemaker for this mode is located in the outer part of the shear layer in the flame. The components of the sensitivity tensor reveal that the eigenvalue is most sensitive to the same feedback mechanism as that of mode A, but in the shear layer in the flame. This shows that, in contrast to the conclusions of Nichols & Schmid (2008), the flame does support self-sustained oscillations. Nichols *et al.* (2009) suggested that the low-frequency oscillations observed in the nonlinear simulations could be caused by the streamwise confinement of the flow upstream of the flame base leading to resonant modes. This theory has been tested by calculating resonant modes for a lifted flame at $Da = 500,000$ and comparing the difference in frequencies between these resonant modes with the frequency observed in the nonlinear simulations. The resonant mode frequencies are several times larger than the frequency observed in the nonlinear simulations. The results from the linear global stability analysis in this chapter, however, show that the low-frequency oscillations observed in the nonlinear simulations can be more simply explained by linear global instability of mode B. This is con-

firmed by comparing the linear global mode growth rates and frequencies for both modes A and B to nonlinear results from Nichols & Schmid (2008) for flames at $Da = 500,000$ and $Da = 700,000$. The good agreement supports the conclusion that the low-frequency oscillations observed in the nonlinear simulations are due to a global instability of the flame.

For mode A, the growth rate and frequency are most sensitive to steady forces near the jet shear layer upstream of the flame base. This suggests that passive control of this mode may not be feasible because the flame is likely to attach to any control devices placed at or near the flame base. For mode B, on the other hand, regions upto two or three diameters away from the fuel jet are moderately sensitive to steady forces. Passive control of this mode may, therefore, be feasible. The sensitivity map shows a large region where the drag force from a thin axisymmetric control ring can stabilize this mode of instability.

8

Global stability and control of swirling diffusion flames

8.1 Introduction

In many combustion applications, swirl is used to improve mixing between fuel and oxidizer and to stabilize the flame through the influence of the vortex breakdown bubble. The use of swirl promotes non-axisymmetric modes of instability. These modes have been observed in previous numerical (Ranga Dinesh *et al.*, 2009) and experimental (Al-Abdeli & Masri, 2003) studies on non-premixed turbulent swirling flames, where they have been referred to as the *precessing vortex core* (PVC). Due to the complexity of the problem, there has not been, until now, a fundamental study of the hydrodynamic instability in swirling flames.

In this chapter, the techniques described in chapters 2 and 3 are used to study the origin and control of global instability in swirling diffusion flames. Two qualitatively different types of steady swirling flames are obtained. These are globally unstable to helical modes of instability, with $m = -1$. A structural sensitivity analysis is used to identify the origin of the helical modes of instability. Finally, the sensitivity of these helical modes to steady body forcing and heat input is calculated.

8.2 Flow configuration

A swirling jet of fuel exits into a large cylindrical domain of length X_{max} and radius R_{max}. The velocity profiles used at the inlet are the same as those in chapter 6. The mixture fraction of the fuel is chosen to have the same top-hat profile as the axial velocity. The temperature profile at the inlet is set to be uniform. The nondimensional base flow inlet profile is then given by:

$$
\begin{aligned}
y(0,r) &= \frac{1}{1+(e^{4r^2\log(2)}-1)^5}, && \text{(8.1a)}\\
\bar{Z}(0,r) &= y(0,r), && \text{(8.1b)}\\
\bar{\rho}(0,r) &= \frac{1}{(S_1-1)Z(0,r)+1}, && \text{(8.1c)}\\
\bar{m}_x(0,r) &= \bar{\rho}(0,r)\left(u_c+(1-u_c)y(0,r)\right), && \text{(8.1d)}\\
\bar{m}_r(0,r) &= 0, && \text{(8.1e)}\\
\bar{m}_\theta(0,r) &= \bar{\rho}(0,r)\left(2qre^{-(2r/0.9)^4}\right). && \text{(8.1f)}
\end{aligned}
$$

The flow variables are nondimensionalized by the jet diameter, jet centreline axial velocity and ambient density. The Reynolds number is defined in terms of the jet diameter, jet centreline axial velocity and jet density. The Prandtl number, $Pr = 0.7$, and Schmidt number, $Sc = 0.7$, describe the ratio of the diffusivity of temperature and mass, respectively to the diffusivity of momentum.

The density ratio parameter $S_1 = 7.0$ defines the ratio of the oxidizer density to fuel density. The reaction chemistry is chosen to be identical to that used in the previous chapter: the ratio of the adiabatic flame temperature to the ambient temperature defines the temperature ratio parameter $S_2 = 6.0$. The reaction chemistry is described by the mass stoichiometric ratio, $s = 2$, the equilibrium constant, $\kappa = 0.01$, the heat release parameter, $\alpha = 0.833$, and the Zeldovich number $\beta = 3$. The fuel-oxidizer mixture is

ignited by a Gaussian shaped impulse in the initial temperature profile at $(x, r) = (2.0, 0.5)$. The flames in this chapter are therefore similar to those in the previous chapter, with the exception that the flames are now swirling. Two qualitatively different types of swirling flames are studied in this chapter: the first is a swirling jet diffusion flame without co-flow, the second is a lifted swirling diffusion flame with strong co-flow.

8.3 Swirling jet diffusion flame, without coflow

The first type of swirling flame considered is obtained for $Re = 175$, $q = 2.05$ and $Da = 100,000$. The axial coflow parameter in (8.1d) is set to $u_c = 0.01$ to improve numerical stability. The governing equations are discretized on a grid with 255×513 points for a domain measuring 20×10 jet diameters in the radial and axial directions respectively.

A steady base flow is obtained using SFD. This is shown in figure 8.1. A vortex breakdown bubble exists between $0.5 < x < 3$ within the core of the fuel jet. The azimuthal velocity within the flame is less than half of the peak azimuthal velocity at inlet. The flame base is at $(x, r) = (1.0, 0.75)$. The flame has two distinct branches downstream of the flame base: the outer branch forms the outer surface of the flame, while the inner branch surrounds the vortex breakdown bubble. The flame is thicker and broader than the flame in the previous chapter because the flame in this chapter has been obtained for lower Da and Re.

8.3.1 Global stability and structural sensitivity

The steady base flow is found to be unstable to perturbations with $m = -1$. Figure 8.2 shows the eigenvalue spectrum that is obtained. The only unstable mode has an eigenvalue of $\lambda = 0.01 + 0.08\mathrm{i}$. The imaginary part of the eigenvalue corresponds to $St = 0.013$, which is a low frequency of oscillation. The real parts of the direct and adjoint global modes are shown in figure 8.3.

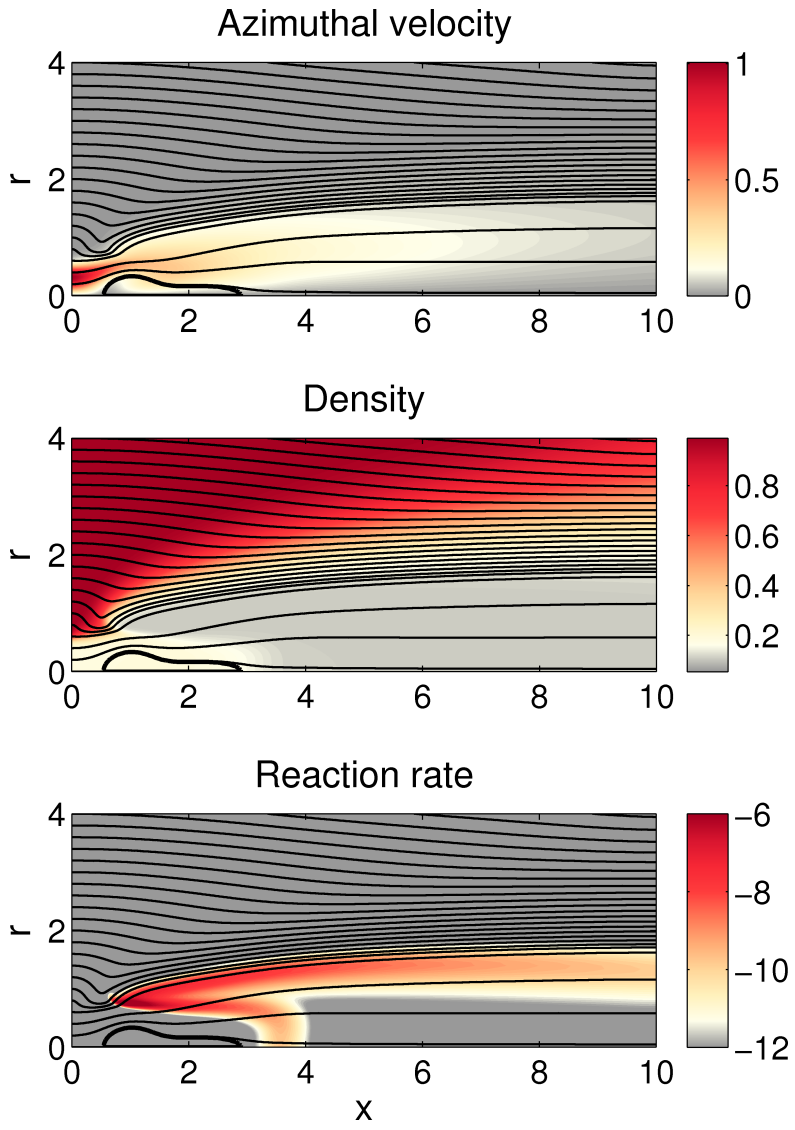

Figure 8.1: The steady baseflow for a swirling diffusion flame at $Re = 175$, $q = 2.05$ and $Da = 100,000$. The streamlines show the axial and radial velocity and the colours show, from the top, contours of (a) azimuthal velocity, (b) density, and (c) reaction rate, $\log(\bar{\omega})$. The thick black line shows the vortex breakdown bubble.

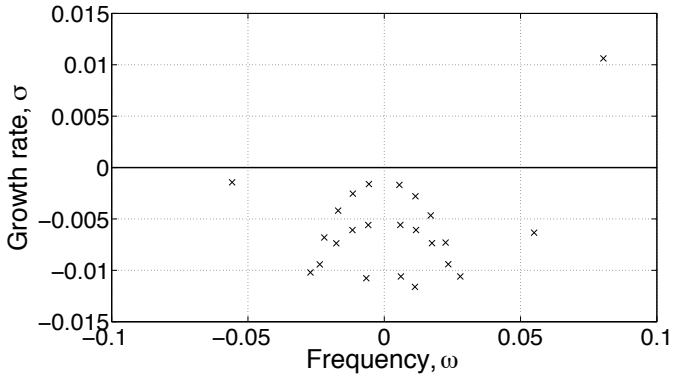

Figure 8.2: Eigenvalue spectrum for $|m| = 1$ for the flame shown in figure 8.1. The 25 least stable modes are shown. Modes with $\omega < 0$ correspond to $m = +1$, while modes with $\omega > 0$ correspond to $m = -1$.

The direct global mode has a large wavelength of around 8 jet diameters, and evolves along the flame surface. For this case, the adjoint global mode has been obtained by power-iteration rather than the Arnoldi method because power-iteration produced a converged mode in less computational time than ARPACK. The adjoint global mode has a similar structure to the adjoint global mode for mode B in figure 7.5(b).

The origin of this mode is identified using the structural sensitivity. The Frobenius norm of the structural sensitivity tensor, containing only momentum terms, is shown in figure 8.4. The wavemaker is located at the flame base. The full sensitivity tensor is shown in figure 8.5. It is clear that the eigenvalue is most sensitive to feedback from the temperature into the momentum equations, particularly the azimuthal momentum equation, at the flame base. This highlights the importance of density fluctuations in determining the growth rate and frequency of the unstable mode. The results suggest that this mode of instability arises from the flame rather than the breakdown bubble. It is not related to the spiral mode of vortex breakdown observed in chapters 5 and 6.

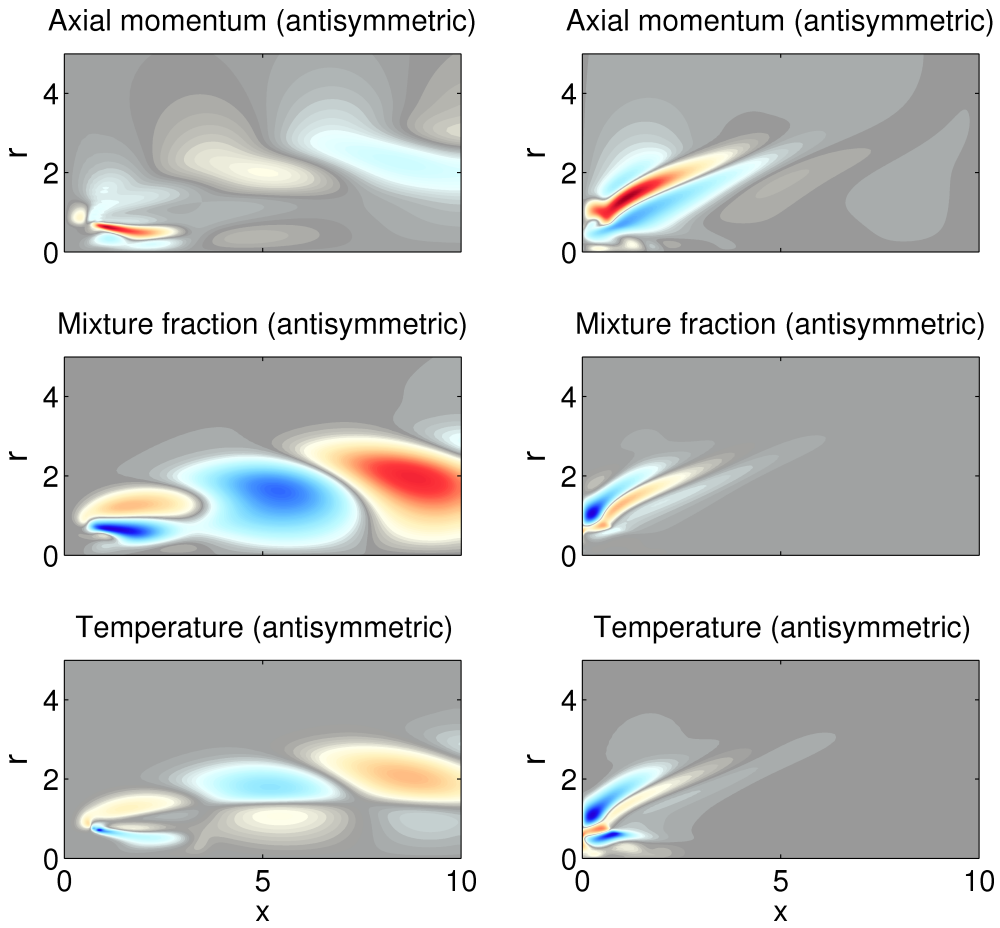

(a) Direct global mode

(b) Adjoint global mode

Figure 8.3: The real parts of the direct and adjoint global modes for the only unstable mode, with $m = -1$, for the flow in figure 8.1. The mode has eigenvalue $\lambda = 0.01 + 0.08\mathrm{i}$.

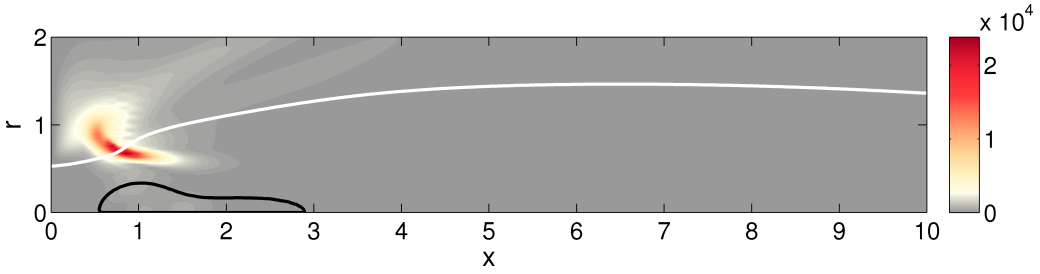

Figure 8.4: The wavemaker, as defined by 2.24 for the unstable mode shown in figure 8.3. This is equivalent to the definition of Giannetti & Luchini (2007).The thick white line shows the stoichiometric surface, which corresponds to $\bar{Z} = 0.333$.

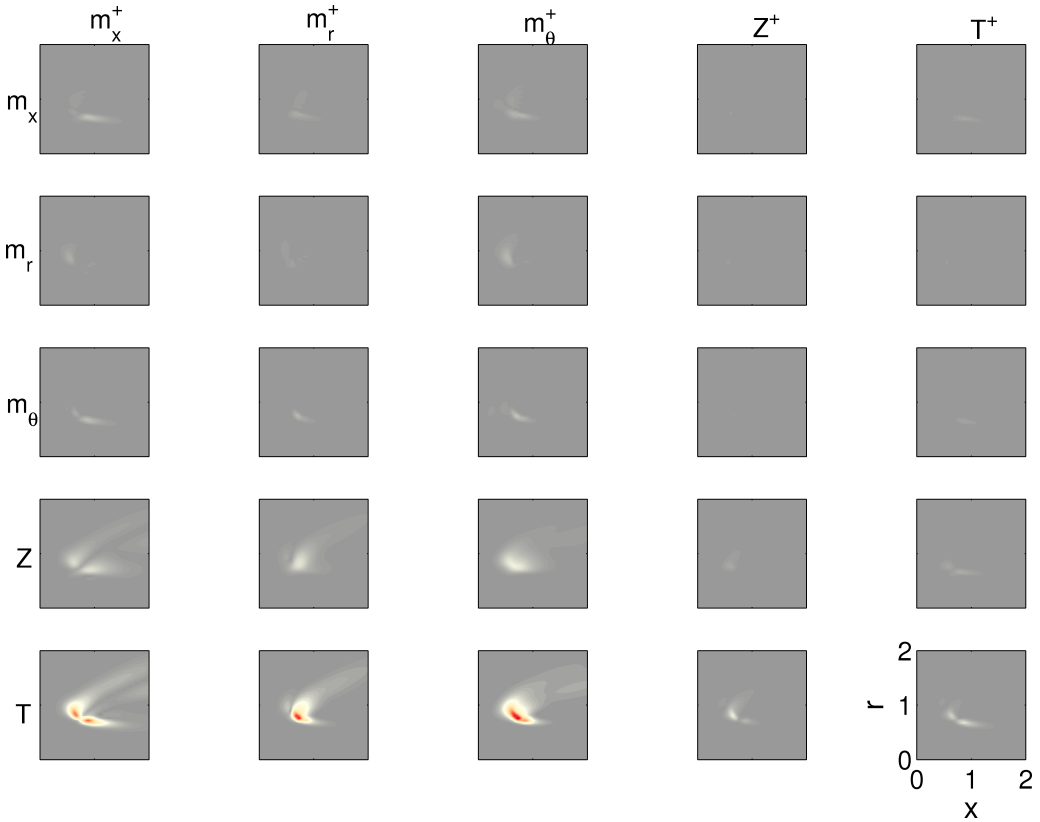

Figure 8.5: The components of the structural sensitivity tensor, $\hat{\mathbf{q}}_i(\hat{\mathbf{q}}_j^+)^*$, for the unstable mode shown in figure 8.3. The shading on all the plots is equal and goes from 0 (grey) to 305800 (red).

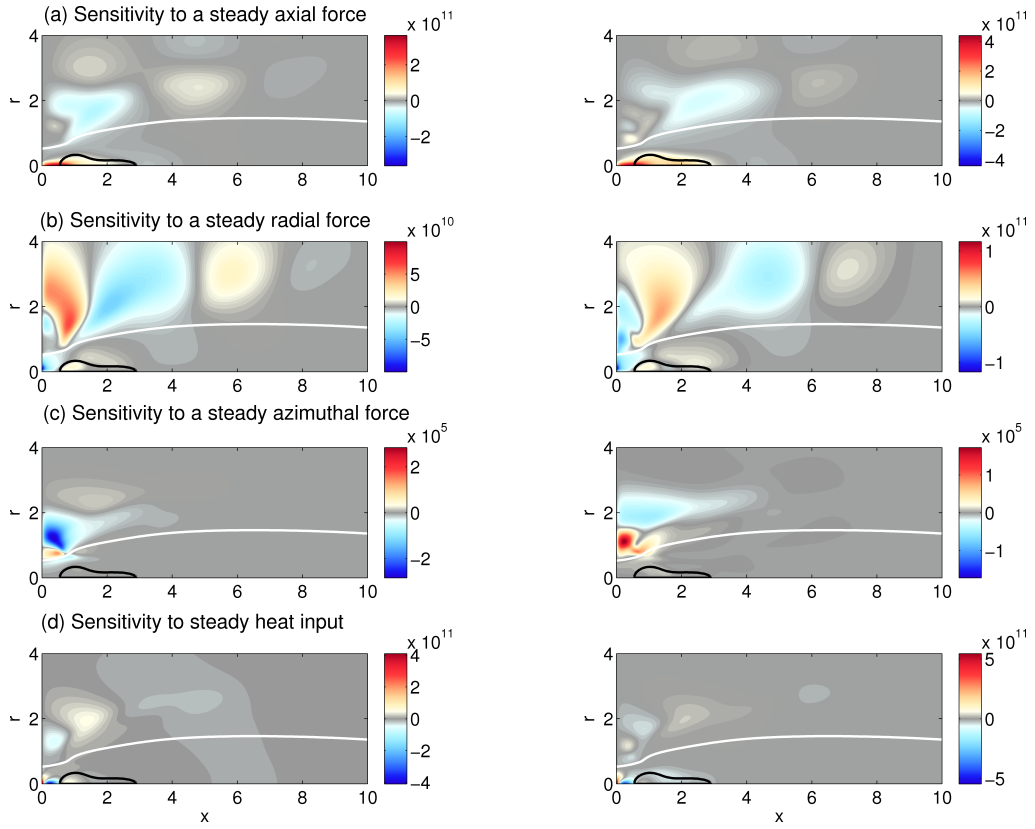

Figure 8.6: The sensitivity of the marginally unstable eigenvalue of the $m = -1$ mode in figure 8.3 to steady forcing, $\nabla_{\bar{\mathbf{F}}}\lambda$. The colours show the sensitivity of the growth rate (left), and frequency (right). The thick white line shows the stoichiometric surface, which corresponds to $\bar{Z} = 0.333$. The thick black line shows the vortex breakdown bubble.

8.3.2 Sensitivity to a control force

The direct and adjoint global modes are used to calculate the sensitivity of the growth rate and frequency of the unstable mode to steady body forcing and heat addition. The results are shown in figure 8.6. The mode is most sensitive to a steady axial force just upstream of the vortex breakdown bubble. Just as for mode B in the previous chapter, there are large regions away from the flame where the drag from a thin control ring can stabilize this mode. The sensitivies have very large magnitudes, just as in the previous chapter. This is again due to the eigenvalue being extremely sensitive to changes in the base flow mixture fraction profile. The sensitivity to a steady azimuthal

force is several orders of magnitude smaller than the sensitivity to steady axial and radial forces. This is because the base flow, and any change to it, is assumed to be axisymmetric. An axisymmetric steady azimuthal force does not affect the axisymmetric base flow mixture fraction profile and, therefore, has a smaller direct effect on the eigenvalue.

8.4 Swirling diffusion flame, with strong coflow

The second swirling flame considered is obtained for $Re = 200$ and $q = 2.00$ with $Da = 600,000$. The axial coflow parameter is set to $u_c = 1.0$. This means that the swirling jet of fuel is surrounded by a non-swirling flow of oxidizer with the same axial velocity as the fuel. The governing equations are discretized on a grid with 127×513 points for a domain measuring 10×10 jet diameters in the radial and axial directions respectively.

A steady base flow is obtained by time-stepping the axisymmetric equations of motion. This is shown in figure 8.7. A vortex breakdown bubble exists between $2.0 < x < 3.5$ within the core of the fuel jet. Compared to figure 8.1, this flame is stabilized further downstream at around $(x, r) = (4.0, 0.75)$. The flame has a conical base that sits partly within the breakdown bubble. The flame is visibly thinner than the flame in figure 8.1 because the Da used is higher here.

It can be seen that the flame base is not well-resolved. Ideally, a finer grid should be used. However, it was found that the grid resolution strongly limits the timestep used for the continuous adjoint of swirling reacting flows. A grid with 1.5 times the resolution presented here was tried - but the timestep used had to be around 50 times smaller for stability. The sixth-order spatial accuracy places a tight constraint on the maximum stable timestep that can be used in the code. If the grid-spacing changes by a factor N, the maximum stable time-step, theoretically, changes by a factor N^6. In addition, it has been found that adjoint codes typically require a time-step of around half the length of the time-step used in the direct code (Chandler, personal commu-

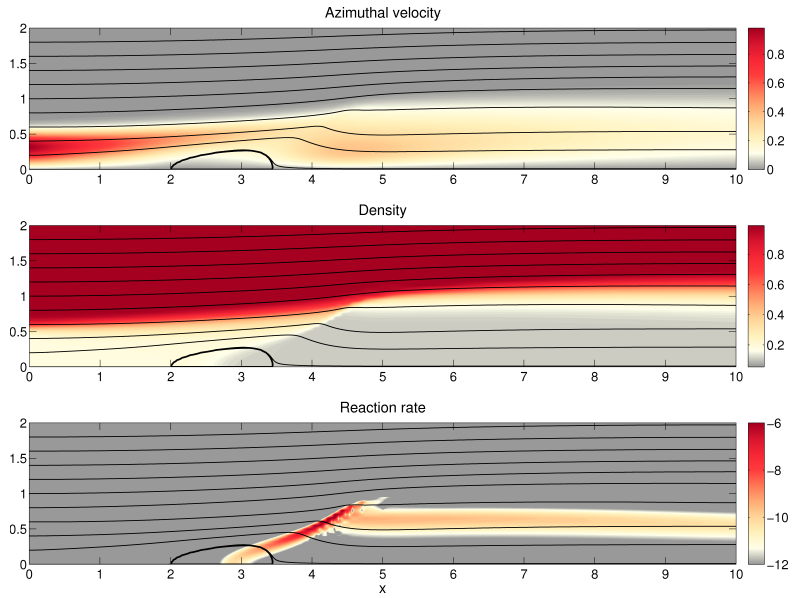

Figure 8.7: The steady baseflow for a swirling diffusion flame, with strong coflow, at $Re = 200$, $q = 2.00$ and $Da = 600,000$. The streamlines show the axial and radial velocity and the colours show, from the top, contours of (a) azimuthal velocity, (b) density, and (c) reaction rate, $\log(\bar{\omega})$. The thick black line shows the vortex breakdown bubble.

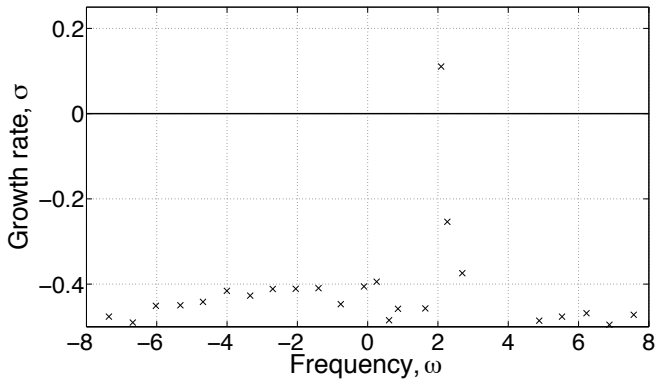

Figure 8.8: Eigenvalue spectrum for $|m| = 1$ for the flame shown in figure 8.7. The 25 least stable modes are shown. Modes with $\omega < 0$ correspond to $m = +1$, while modes with $\omega > 0$ correspond to $m = -1$.

nication, 2010). As a result of these complications, the adjoint global mode could not be obtained for the higher-resolution case in time for the completion of this thesis. The direct global mode, however, was obtained and is shown, together with the higher-resolution base flow in the appendix to this chapter. The discrepancy between the eigenvalues of the higer-resolution and lower-resolution direct global mode, calculated as $\text{abs}(\lambda_{high} - \lambda_{low})/\text{abs}(\lambda_{high})$, is 1.79%.

8.4.1 Global stability and structural sensitivity

The steady base flow is found to be unstable to perturbations with $m = -1$. Figure 8.8 shows the eigenvalue spectrum obtained. The only unstable mode has an eigenvalue of $\lambda = 0.11 + 2.09\text{i}$. The real part of the eigenvalue is relatively large, suggesting that the flow is far from the bifurcation point, and that the steady base flow shown in figure 8.7 will not exist in practice. The imaginary part of the eigenvalue corresponds to a higher frequency than that for the mode in §8.3. The real parts of the direct and adjoint global modes are shown in figure 8.9. The adjoint global mode has maximum amplitude near the axis, upstream of the vortex breakdown bubble and has a similar structure to the adjoint global mode for the $m = -1$ mode of spiral vortex

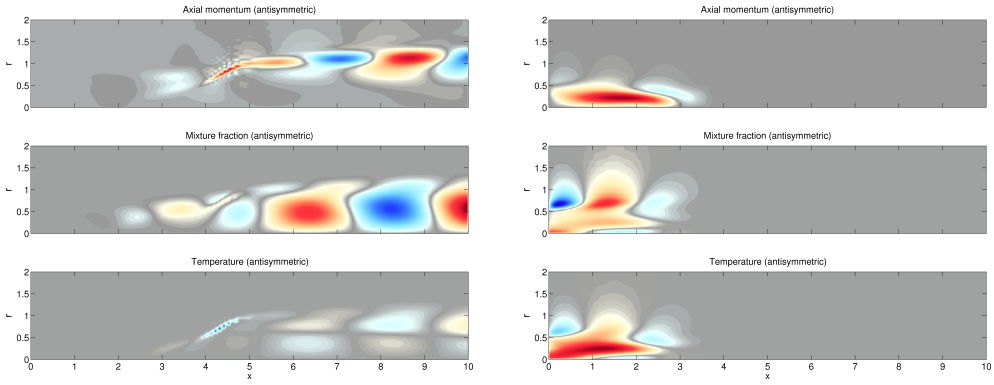

(a) Direct global mode (b) Adjoint global mode

Figure 8.9: The real parts of the direct and adjoint global modes for the only unstable mode, with $m = -1$, for the flow in figure 8.7. The mode has eigenvalue $\lambda = 0.11 + 2.09\mathrm{i}$.

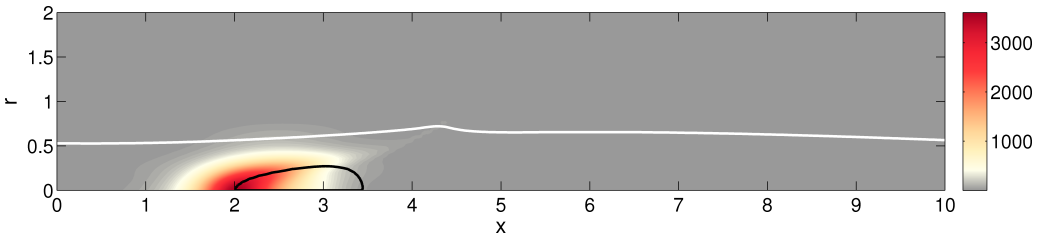

Figure 8.10: The wavemaker, as defined by 2.24 for the unstable mode shown in figure 8.9. This is equivalent to the definition of Giannetti & Luchini (2007).The thick white line shows the stoichiometric surface, which corresponds to $\bar{Z} = 0.333$.

breakdown in chapters 5 and 6.

The origin of this mode is identified using the structural sensitivity. The Frobenius norm of the structural sensitivity tensor, containing only momentum terms, is shown in figure 8.10. The wavemaker is located at the upstream end of the recirculation bubble, just as for the spiral mode of vortex breakdown in the Grabowski profile in chapter 5. The full sensitivity tensor is shown in figure 8.11. The eigenvalue is most sensitive to feedback from the temperature into the momentum equations, particularly the azimuthal momentum equation, along the edge of the recirculation bubble. However, it

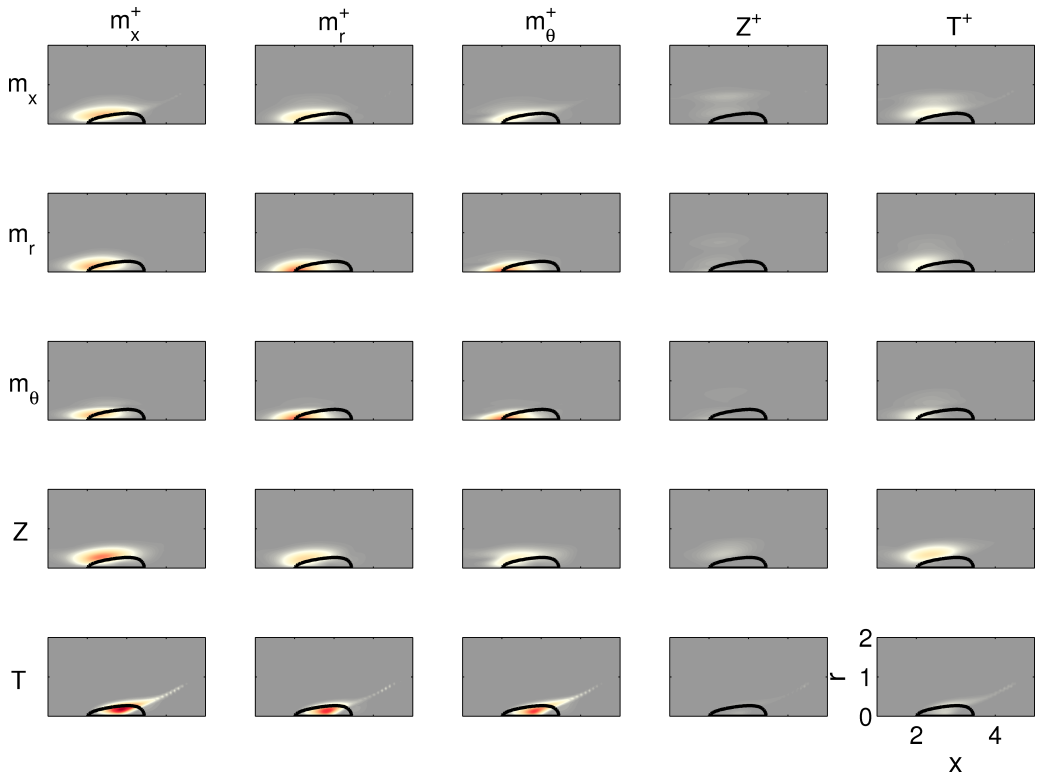

Figure 8.11: The components of the structural sensitivity tensor, $\hat{\mathbf{q}}_i(\hat{\mathbf{q}}_j^+)^*$, for the unstable mode shown in figure 8.9. The shading on all the plots is equal and goes from 0 (grey) to 2979 (red).

can be seen that feedback between the components of the momentum vector is only slightly less influential than feedback from temperature into the momentum. The nine frames in the top left corner are quite similar to the components in figure 5.7 in chapter 5. This confirms that this mode of instability arises from the vortex breakdown bubble and can be interpreted as the spiral mode of vortex breakdown - it is the same instability as that observed in chapters 5 and 6.

The origin of this mode is further investigated by setting $Da = 0$ in the linear global stability analysis. This sets the linearized heat release terms in the linearized LMN equations to zero. The unstable mode now has an eigenvalue of $\lambda = 0.07 + 2.08\mathrm{i}$, which means that it has a lower growth rate and almost similar frequency to the mode in figure 8.9. The direct and adjoint global modes are qualitatively similar to those in figure 8.9 and the wavemaker is found to be in the same location - the upstream stagnation point of the vortex breakdown bubble. Local stability analyses on reacting flows, for example Nichols & Schmid (2008) and Emerson *et al.* (2012), often neglect the linearized heat release terms in the stability analysis. The linear global stability for $Da = 0$ calculated here confirms that, for a mode that is not caused by the flame itself, such an approach can give useful predictions. However, such a local stability analysis is not expected to be accurate when the instability arises from the flame itself - such as the mode in figure 8.3.

8.4.2 Sensitivity to a control force

The direct and adjoint global modes are used to calculate the sensitivity of the growth rate and frequency of the unstable mode to steady body forcing and heat addition. The results are shown in figure 8.12. The mode is most sensitive to a steady axial force just upstream of the vortex breakdown bubble. In contrast to figure 8.6, however, most of the sensitive regions are located within the fuel jet and near the stoichiometric surface. Experimental validation of these sensitivity maps would, therefore, be difficult.

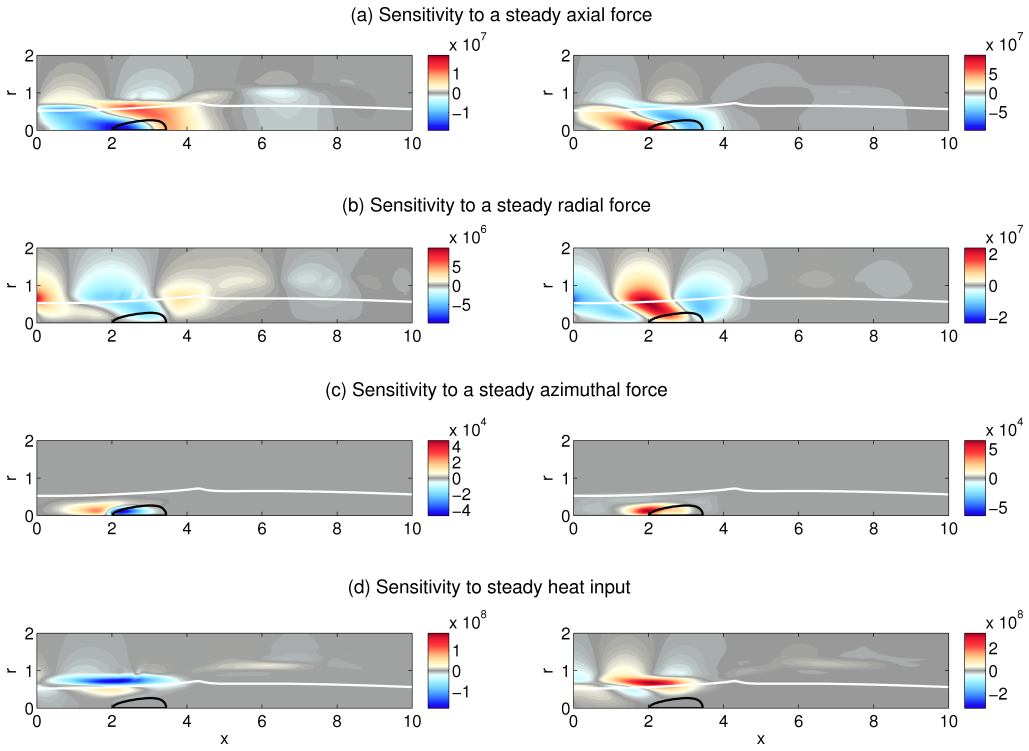

Figure 8.12: The sensitivity of the marginally unstable eigenvalue of the $m = -1$ mode in figure 8.9 to steady forcing, $\nabla_{\bar{\mathbf{F}}}\lambda$. The colours show the sensitivity of the growth rate (left), and frequency (right). The thick white line shows the stoichiometric surface, which corresponds to $\bar{Z} = 0.333$. The thick black line shows the vortex breakdown bubble.

8.5 Summary

This chapter has looked at the linear global stability of swirling diffusion flames. Two qualitatively different types of swirling flames have been considered. Both flames have vortex breakdown bubbles and are globally unstable to helical perturbations, with $m = -1$. The most unstable direct and adjoint global modes have been obtained. These have been used to identify the origin and mechanism of the global instability for each flame and to consider where a control force may be applied to either suppress or promote the instability.

The first type of flame that has been considered has negligible coflow of oxidizer around the fuel jet. In the steady base flow, the flame base sits close to the jet exit plane. This flame is unstable to a low-frequency, long-wavelength mode that grows radially outwards from the flame base along the flame surface. The wavemaker of this mode is located at the flame base. The components of the structural sensitivity tensor show that this mode of instability is caused by density fluctuations at the flame base, suggesting that this mode of instability is related to the flame itself and not to the vortex breakdown bubble. This mode of instability is sensitive to steady forcing away from the flame, and can, therefore, be practically controlled.

The second type of flame that has been considered has strong coflow of oxidizer around the fuel jet. In the steady base flow, the flame sits far downstream of the jet exit plane and vortex breakdown bubble. This flame is unstable to a high-frequency, short-wavelength mode that grows from upstream of the flame base. The wavemaker of this mode is located at the upstream stagnation point of the vortex breakdown bubble. The components of the structural sensitivity tensor show that this mode of instability is similar to the spiral mode of vortex breakdown observed in chapters 5 and 6.

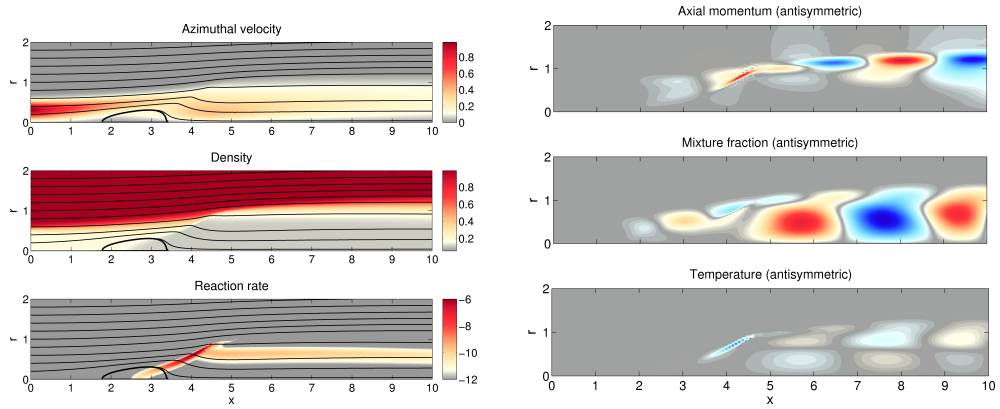

(a) Base flow (b) Direct global mode

Figure 8.13: (a) The steady base flow, and (b) The real parts of the direct global mode for the only unstable mode, with $m = -1$, for a higher resolution simulation of the flow in figure 8.7. This mode has eigenvalue $\lambda = 0.14+2.10\mathrm{i}$.

Appendix

The base flow and most unstable direct global mode for the flame considered in §8.4 are obtained on a grid with 181×725 points for a domain measuring 10×10 jet diameters in the radial and axial directions respectively. The base flow is shown in figure 8.13(a), and can be compared directly with figure 8.7. The most unstable direct global mode is shown in figure 8.13(b), and can be compared directly with figure 8.9(a).

9

Concluding remarks

9.1 Summary of work completed

The work presented in this thesis is part of a wider project that aims to calculate sensitivity maps for hydrodynamic instability in flows with strong density and velocity gradients, such as the flows found in fuel injectors in gas turbine combustion chambers. The aim of this thesis has been to extend the tools developed from a previous project (Chandler, 2010), and to apply these tools to study the origin and control of global instabilities in swirling jets and flames.

As a first step, though, these tools have been used to study the control of global instability in a low-density Helium jet. The direct and adjoint global modes have been used to identify the regions of the flow where the drag and heat transfer from a thin control ring can stabilize the flow. An adiabatic control ring has most effect in the shear layer just inside the jet, while a hot control ring has most effect just outside the jet. Heat transfer outside the jet has a strong effect on the growth rate and frequency of the unstable mode through entrainment. The control ring affects the eigenvalue primarily through changing the axial velocity and density profile of the base flow.

For the first time, these tools have also been applied to study the origin and passive control of spiral vortex breakdown using two model velocity pro-

files. The first is the Grabowski profile: this is well-studied numerically and is a good model for swirling flow in ducts. The second is the Billant profile: this is a good model for experimental measurements of velocities near the exit plane of swirling jets.

In each case, the direct and adjoint global modes have been calculated and combined using the structural sensitivity framework to identify the region of the flow that is responsible for causing spiral vortex breakdown, also known as the wavemaker. In order to identify the physical mechanisms that are active in the wavemaker, the separate components of the structural sensitivity have been examined for the first time. The direct and adjoint global modes have also been used to identify the regions of the flow where steady and unsteady control, such as a drag force or heat addition, can suppress or promote spiral vortex breakdown.

For both profiles, a steady breakdown bubble forms near the jet axis, and the flow around this bubble is globally unstable to a helical mode, with $m = -1$. For the Grabowski profile, at the point of instability, the wavemaker of this spiral mode is located just upstream of the vortex breakdown bubble. For the Billant profile, the wavemaker is located in the wake of the breakdown bubble. For both profiles, however, the same feedback mechanism is responsible for causing the spiral mode of vortex breakdown: this mechanism is related to conservation of angular momentum, and makes the eigenvalue most sensitive to feedback between the radial and azimuthal components of the perturbation momentum.

This helical mode of vortex breakdown is most sensitive to steady axial forcing in the wavemaker region. For both profiles, there are regions near the inlet where the drag from a thin control ring can affect the growth rate and frequency of the helical mode of vortex breakdown. Heat addition has no effect on the growth rate and frequency of the helical mode in a uniform-density flow. In a low-density swirling jet, however, heat addition near the inlet has a strong stabilizing effect on the helical mode of vortex breakdown.

These studies on non-reacting flows have provided a good background to investigate hydrodynamic instability in flames. The global stability of a non-swirling lifted diffusion flame, which was first studied by Chandler (2010), has been revisited, revealing more interesting physics. The lifted diffusion flame supports two modes of global instability. The first mode, originally identified by Chandler (2010), is a high-frequency mode caused by the instability of the low-density jet shear layer in the premixing zone. The second mode, identified for the first time in this thesis, is a low-frequency mode caused by an instability of the outer shear layer in the flame. The components of the structural sensitivity highlight the importance of feedback from the density fluctuations to the perturbation momentum in influencing the eigenvalue. The growth rates and frequencies of both these modes are extremely sensitive to changes in the base flow mixture fraction profile. Any control influence will, therefore, act primarily through the effect of the control device or technique on the mixture fraction, which affects the rate of reaction.

Finally, this thesis has considered the hydrodynamic stability of swirling diffusion flames with vortex breakdown. This is a good model for flames in real fuel injectors, albeit at much lower Reynolds numbers. The two types of swirling flames considered in this thesis show qualitatively similar behaviour to the lifted jet diffusion flames. The first type of flame is unstable to a low-frequency long-wavelength mode, with wavemaker located at the flame base. The second type of flame is unstable to a high-frequency, short-wavelength mode, with wavemaker located at the upstream edge of the vortex breakdown bubble. The first mode of instability is caused by density fluctuations at the flame base, while the second mode of instability is similar to the helical mode of vortex breakdown occuring in a reacting flow.

These results support the conclusion that, in addition to changing the velocity and density profiles of the base flow, the presence of reaction increases the influence of changes in the mixture fraction of the base flow on the eigenmode. This increased influence acts through the reaction term. In the flows

that have been considered in this thesis, the presence of reaction also adds an additional mode of hydrodynamic instability to flows. This additional mode has a low frequency of oscillation, and is sensitive to steady forcing even far from the flame. This suggests that passive control of this mode can be tested experimentally.

9.2 Main conclusions

The aim of this thesis has been to demonstrate the use of linear global stability and sensitivity analyses to study hydrodynamic instability in swirling reacting flows using the low Mach number equations, which is a significant advance on the state of the art. The main findings can be summarized as follows.

- Feedback from density perturbations has a strong influence on the hydrodynamic instability of reacting flows.

- Eigenmodes in reacting flows are very sensitive to changes in the species mixture fraction because these changes strongly influence the base flow.

- In a reacting flow, the wavemaker region is very sensitive to the flame configuration. In some cases, the wavemaker responsible for causing hydrodynamic instability in a reacting flow is very similar to its non-reacting counterpart. In other cases, however, the wavemakers of the reacting and non-reacting flows are quite different. This means that non-reacting or 'cold' simulations and experiments may not always capture the physical mechanisms that are important in the reacting flow.

- In stability analyses on flow profiles taken from reacting simulations and experiments, it may be very important to include the effect of heat release terms in the stability analysis.

9.3 Further work

From a scientific point of view, the structural sensitivity analysis presented in this thesis can be extended to derive more information about the mechanisms driving the global instability. In this thesis, the components of the structural sensitivity tensor have been compared to understand how feedback between the components of the state vector affects the global eigenvalue. This is the simplest way of interpreting the results, but it may not be the best way of interpreting the results. It is likely that more efficient ways of extracting physically relevant information can be derived.

From a computational point of view, the tools developed here can be made more efficient for the study of reacting flows. The main extension would involve improving resolution and accuracy, without increasing the overall computational effort. The use of a finite-element package, such as FEniCS, may seem, at first glance, an easy solution - especially with the advent of automatic differentiation softwares that automatically calculate the adjoint. However, the use of such a package for a reacting flow would be extremely computationally expensive. One possibility that can be implemented in the existing code is the use of a stretched grid or adaptive meshing. This would allow a higher resolution to be used only where it is needed. The Poisson solver in the code would then need to be replaced by a multigrid solver.

The techniques described in chapter 2 and 3 can be used to study hydrodynamic instability in premixed flames. This would require significant modification of the existing code because the mixture fraction equation is redundant: premixed flames have a uniform mixture fraction. Instead, the flame front needs to be tracked - for example by using a level-set method. Alternatively, an easier approach may be to use a progress variable instead. The progress variable is a scalar quantity that is equal to zero in the unburned fluid and one in the burned fluid. Its evolution obeys a conservation law. In these ways, it is similar to the mixture fraction used to study diffusion flames. Premixed flames also tend to be thinner than diffusion flames

and so, it is likely that the computational effort required to study premixed flames would be greater than that required to study the diffusion flames in this thesis.

In terms of the wider aim of obtaining sensitivity maps of real fuel injectors, the work in this thesis can be extended in two main ways. Firstly, the tools can be extended to consider flows with higher Reynolds numbers, which are turbulent. The large-scale coherent structures in these flows are most influential in determining the mixing properties and global dynamics of the flow. These large-scale coherent structures are affected by the fine scale turbulence in the flow. Direct numerical simulation of all the spatial scales in such a flow is not feasible. Therefore, turbulence models need to be included to model the effect of the fine-scale turbulence on the large-scale coherent structures. A linear global stability analysis can then be performed around the turbulent mean flow, and the techniques described in chapter 2 can then be applied to the least stable or most unstable modes that are found. Several recent studies have attempted this on incompressible flow around bluff-bodies (for example, Meliga *et al.* (2012*b*)), and, with the tools developed here, the same could be done for flames. Some work has already begun in this regard. For example, Gupta & Juniper (2013) have considered the use of explicit algebraic Reynolds Stress models in a local stability analysis of turbulent channel flows. Such a model is suitable for swirling flows typical of fuel injectors. The inclusion of such a model in the equations of motion is not conceptually difficult.

Secondly, the tools can be extended to include complex geometry and the possibility of shape modification. This favours the use of spectral element methods over the finite difference schemes used in this thesis. The adjoint base flow pressure provides the sensitivity of the eigenvalue to steady blowing and suction. This idea can be extended by including some form of a shape parameter in the derivation of the sensitivity functions in chapter 2. The sensitivity of the eigenvalue to a small change in this shape parameter can then be calculated. This can be used in an optimization routine to progres-

sively make small changes to the design, until a local maximum or minimum is reached. These ideas are currently being worked on in the research group.

Finally, the tools developed here can be useful in studying thermoacoustic oscillations. For a flame, the adjoint global mode represents the receptivity to external forcing close to the frequency of the global mode. It can be used to identify the regions of the flow that are most receptive to perturbations. In a thermoacoustic system, such perturbations may be caused by, for example, acoustic waves impinging on boundaries. The response of the flame to acoustic perturbations forms part of the feedback loop that drives thermoacoustic oscillations. By mapping this response, the tools can be used to better understand thermoacoustic oscillations. On a lighter note, this may perhaps even be of interest to Lord Rayleigh, wherever he may be, whose seminal work on thermoacoustic oscillations (Rayleigh, 1878*a*) preceded, and arguably, motivated his work on hydrodynamic stability. In his own words, 'Many, it may even be said, most of the still unexplained phenomena of acoustics are connected with the instability of jets of fluid.' (Rayleigh, 1878*b*)

"The work may be hard, and the discipline severe; but the interest never fails, and great is the privilege of achievement."

-Lord Rayleigh

References

Akervik, E., Brandt, L., Henningson, D. S., Hoepffner, J., Marxen, O. & Schlatter, P. 2006 Steady solutions of the Navier-Stokes equations by selective frequency damping. *Physics of Fluids* **18** (068102). 41, 53

Al-Abdeli, Y. M. & Masri, A. R. 2003 Stability characteristics and flowfields of turbulent non-premixed swirling flames. *Combustion Theory and Modelling* **7** (4), 731–766. 153

Batchelor, G. K. 1964 Axial flow in trailing line vortices. *Journal of Fluid Mechanics* **20** (4), 645–658. 9

Batchelor, G. K. 1967 *An introduction to fluid dynamics*. Cambridge University Press. 91

Benjamin, T. B. 1962 Theory of the vortex breakdown phenomenon. *Journal of Fluid Mechanics* **14** (4), 593 – 629. 74

Billant, P., Chomaz, J.-M. & Huerre, P. 1998 Experimental study of vortex breakdown in swirling jets. *Journal of Fluid Mechanics* **376**, 183–219. 107, 108, 109, 110, 111, 112, 119, 128, 130

Briggs, R. J. 1964 *Electron-stream interaction with plasmas*. MIT Press. 48

Broadwell, J. E. & Mungal, M. G. 1991 Large-scale structures and molecular mixing. *Physics of Fluid A* **3** (5), 1193–1206. 1

Brown, G. L. & Roshko, A. 1974 On density effects and large structure in turbulent mixing layers. *Journal of Fluid Mechanics* **64**, 775–816. 2

Butler, K. M. & Farrell, B. F. 1992 Three-dimensional optimal perturbations in viscous shear-flow. *Physics of Fluids A* **4**, 1637–1650. 6

Carton, X. & McWilliams, J. 1989 Barotropic and baroclinic instabilities of axisymmetric vortices in a quasi-geostrophic model. In *Mesoscale/Synoptic Coherent Structures in Geophysical Turbulence* (ed. J. Nihoul & B. Jamart), pp. 225–244. Elsevier. 110

Chakravarthy, S. R., Shreenivasan, O. J., Boehm, B., Dreizler, A. & Janicka, J. 2007 Experimental characterization of onset of acoustic instability in a nonpremixed half-dump combustor. *Journal of the Acoustical Society of America* **122** (1), 120–127. 2

Chandler, G. J. 2010 Sensitivity analysis of low-density jets and flames. PhD thesis, University of Cambridge. 9, 10, 11, 14, 21, 30, 31, 36, 39, 40, 45, 60, 133, 135, 137, 138, 140, 171, 173

Chandler, G. J., Juniper, M. P., Nichols, J. W. & Schmid, P. J. 2012 Adjoint algorithms for the Navier-Stokes equations in the low Mach number limit. *Journal of Computational Physics* **231** (4), 1900–1916. 50, 52, 69, 81

Chomaz, J.-M. 2005 Global instabilities in spatially developing flows: Non-normality and nonlinearity. *Annual Review of Fluid Mechanics* **37**, 357–392. 7, 9, 83, 96

Chomaz, J.-M., Huerre, P. & Redekopp, L. G. 1988 Bifurcations to local and global modes in spatially developing flows. *Physical Review Letters* **60** (1), 25–28. 5

Chorin, A J 1968 Numerical Solution of Navier-Stokes Equations. *Mathematics of Computation* **22** (104), 745–&. 40

Coats, C. M. 1996 Coherent structures in combustion. *Progress in Energy and Combustion Science* **22**, 427–509. 2

Coenen, W. & Sevilla, A. 2012 The structure of the absolutely unstable regions in the near field of low-density jets. *Journal of Fluid Mechanics* **713**, 123–149. 53

Constantinescu, G. S. & Lele, S. K. 2002 A highly accurate technique for the treatment of flow equations at the polar axis in cylindrical coordinates using series expansions. *Journal of Computational Physics* **183** (1), 165–186. 40, 46

Crow, S. C. & Champagne, F. H. 1971 Orderly structure in jet turbulence. *Journal of Fluid Mechanics* **48**, 547–591. 2

Drazin, P. G. & Reid, W. H. 1981 *Hydrodynamic Stability*, 2nd edn. Cambridge University Press. 4

Emerson, B., O'Connor, J., Juniper, M. & Lieuwen, T. 2012 Density ratio effects on reacting bluff body flow field characteristics. *Journal of Fluid Mechanics* **706**, 219–250. 166

Escudier, M. 1988 Vortex breakdown: observations and explanations. *Progress in Aerospace Sciences* **25** (2). 74

Gallaire, F. & Chomaz, J.-M. 2003 Mode selection in swirling jet experiments: a linear stability analysis. *Journal of Fluid Mechanics* **494**, 223–253. 109, 110, 111, 116, 118, 130

Gallaire, F., Ruith, M., Meiburg, E., Chomaz, J.-M. & Huerre, P. 2006 Spiral vortex breakdown as a global mode. *Journal of Fluid Mechanics* **549**, 71–80. 75, 76, 77, 79, 80, 93, 94, 95, 96, 104

Garnaud, X. 2012 Modes, transient dynamics and forced response of circular jets. PhD thesis, Ecole Polytechnique. 54

Garnaud, X., Lesshafft, L., Schmid, P. J. & Huerre, P. 2013 Modal and transient dynamics of jet flows. *Physics of Fluids* **25** (044103). 113

Giannetti, F. & Luchini, P. 2007 Structural sensitivity of the first instability of the cylinder wake. *Journal of Fluid Mechanics* **581**, 167–197. 7, 23, 50, 55, 76, 104, 140, 141, 159, 164

Grabowski, W. J. & Berger, S. A. 1976 Solutions of Navier-Stokes equations for vortex breakdown. *Journal of Fluid Mechanics* **75**, 525. 10, 75, 77, 78

Gupta, V. & Juniper, M. P. 2013 Linear stability analysis of turbulent channel flows: the effects of turbulence closure models. *Physics of Fluids* To be submitted. 176

Hall, M. G. 1972 Vortex breakdown. *Annual Review of Fluid Mechanics* **4**, 195 –. 74

Hallberg, M. P., Srinivasan, V., Gorse, P. & Strykowski, P. J. 2007 Suppression of global modes in low-density axisymmetric jets using coflow. *Physics of Fluids* **19** (014102). 50

Hallberg, M. P. & Strykowski, P. J. 2006 On the universality of global modes in low-density axisymmetric jets. *Journal of Fluid Mechanics* **569**, 493–507. 52

Hallberg, M. P. & Strykowski, P. J. 2008 Open-loop control of fully nonlinear self-excited oscillations. *Physics of Fluids* **20** (041703). 50

Heaton, C. J., Nichols, J. W. & Schmid, P. J. 2009 Global linear stability of the non-parallel Batchelor vortex. *Journal of Fluid Mechanics* **629**, 139–160. 9, 45, 113

Herrada, M. A. & Fernandez-Feria, R. 2006 On the development of three-dimensional vortex breakdown in cylindrical regions. *Physics of Fluids* **18** (084105). 76

Hill, D. C. 1992 A theoretical approach for analyzing the re-stabilization of wakes. *AIAA Paper 92-0067* . 7, 8, 23, 50, 76

Huang, Y. & Yang, V. 2009 Dynamics and stability of lean-premixed swirl-stabilized combustion. *Progress in Energy and Combustion Science* **35**, 293–364. 2

Huerre, P. & Monkewitz, P. A. 1985 Absolute and convective instabilities in free shear layers. *Journal of Fluid Mechanics* **159**, 151–168. 5

Huerre, P. & Monkewitz, P. A. 1990 Local and global instabilities in spatially developing flows. *Annual Review of Fluid Mechanics* **22**, 473–537. 5, 75

Jackson, C. P. 1987 A finite-element study of the onset of vortex shedding in flow past variously shaped bodies. *Journal of Fluid Mechanics* **182**, 23–45. 6

Juniper, M. P., Tammisola, O. & Lundell, F. 2011 The local and global stability of confined planar wakes at intermediate Reynolds number. *Journal of Fluid Mechanics* **686**, 218–238. 37, 47

Lambourne, N. C. & Bryer, D. W. 1961 The bursting of leading-edge vortices- some observations and discussion of the phenomenon. Reports and Memoranda 3282. Aeronautical Research Council. 74

Lehoucq, R. B., Sorensen, D. C. & Yang, C. 1998 ARPACK Users' Guide: Solution of Large-Scale Eigenvalue Problems with Implicity Restarted Arnoldi Methods. *SIAM* . 43

Leibovich, S. 1978 Structure of vortex breakdown. *Annual Review of Fluid Mechanics* **10**, 221 – 246. 74

Leibovich, S. & Stewartson, K. 1983 A sufficient condition for the instability of columnar vortices. *Journal of Fluid Mechanics* **126**, 335–356. 91

Lesshafft, L. 2007 Linear impulse response in hot round jets. *Physics of Fluids* **19** (024102). 37

Lesshafft, L., Huerre, P., Sagaut, P. & Terracol, M. 2006 Nonlinear global modes in hot jets. *Journal of Fluid Mechanics* **554**, 393–409. 50, 52

Lesshafft, L. & Marquet, O. 2010 Optimal velocity and density profiles for the onset of absolute instability in jets. *Journal of Fluid Mechanics* **662**, 398–408. 53

Li, L. K. B. L. & Juniper, M. P. 2012 Lock-in and quasiperiodicity in hydrodynamically self-excited flames: experiments and modelling. *Proceedings of the Combustion Institute* **34** (1). 69, 140

Liang, H. & Maxworthy, T. 2005 An experimental investigation of swirling jets. *Journal of Fluid Mechanics* **525**, 115–159. 109, 110, 130

Lucca-Negro, O. & O'Doherty, T. 2001 Vortex breakdown: a review. *Progress in Energy and Combustion Sciences* **27**, 431–481. 74

Ludwieg, H. 1960 Stabilitat der Stromung in einem zylindrischen Ringraum. *Z. Flugwiss.* **8** (5), 135–140. 74

Marquet, O., Sipp, D. & Jacquin, L. 2008*a* Sensitivity analysis and passive control of cylinder flow. *Journal of Fluid Mechanics* **615**, 221–252. 8, 50, 61

Marquet, O., Sipp, D., Jacquin, L. & Chomaz, J.-M. 2008*b* Multiple timescale and sensitivity analysis for the passive control of the cylinder flow. 5th AIAA Theoretical Fluid Mechanics Conference, 23-26 June 2008, Seattle, Washington. 25

Meliga, P. & Chomaz, J.-M. 2010 Global modes in a confined impinging jet: application to heat transfer and control. *Theoretical and Computational Fluid Dynamics* **25**. 8

Meliga, P. & Gallaire, F. 2011 Global instability of helical vortex breakdown. 6th AIAA Theoretical Fluid Mechanics Conference, 27-30 June 2011, Honolulu, Hawaii. 76, 79, 80, 81, 96

Meliga, P., Gallaire, F. & Chomaz, J.-M. 2012*a* A weakly nonlinear mechanism for mode selection in swirling jets. *Journal of Fluid Mechanics* . 76, 93, 96

Meliga, P., Pujals, G. & Serre, E. 2012*b* Sensitivity of 2-D turbulent flow past a D-shaped cylinder using global stability. *Physics of Fluids* **24** (061701). 176

Meliga, P., Sipp, D. & Chomaz, J.-M. 2010 Open-loop control of compressible afterbody flows using adjoint methods. *Physics of Fluids* **22** (5). 8, 61

Michalke, A. 1984 Survey on jet instability theory. *Progress in Aerospace Sciences* **21**, 159–199. 52

Monkewitz, P. A., Bechert, D. W., Barsikow, B. & Lehmann, B. 1990 Self-excited oscillations and mixing in a heated round jet. *Journal of Fluid Mechanics* **213**, 611–639. 50

Monkewitz, P. A., Huerre, P. & Chomaz, J.-M. 1993 Global linear stability analysis of weakly non-parallel shear flows. *Journal of Fluid Mechanics* **251**, 1–20. 67

Monkewitz, P. A. & Sohn, K. 1986 Absolute instability in hot jets and their control. AIAA Conference 1986. 110

Nichols, J. W. 2005 Simulation and stability analysis of jet diffusion flames. PhD thesis, University of Washington. 14, 39, 40

Nichols, J. W., Chomaz, J.-M. & Schmid, P. J. 2009 Twisted absolute instability in lifted flames. *Physics of Fluids* **21** (015110). 118, 135, 144, 146, 150

Nichols, J. W. & Schmid, P. J. 2008 The effect of a lifted flame on the stability of round fuel jets. *Journal of Fluid Mechanics* **609**, 275–284. 28, 29, 134, 135, 136, 137, 138, 140, 141, 142, 144, 146, 147, 149, 150, 151, 166

Nichols, J. W., Schmid, P. J. & Riley, J. J. 2007 Self-sustained oscillations in variable-density round jets. *Journal of Fluid Mechanics* **582**, 341–376. 40, 113

Oberleithner, K., Sieber, M., Nayeri, C. N., Paschereit, C. O., Petz, C., Hege, H.-C., Noack, B. R. & Wygnanski, I. 2011 Three-dimensional coherent structures in a swirling jet undergoing vortex breakdown: stability analysis and empirical mode construction. *Journal of Fluid Mechanics* . 92

Panda, J. & McLaughlin, D. K. 1994 Experiments on the instabilities of a swirling jet. *Physics of Fluids* **6** (1), 263–276. 2

Peckham, D. H. & Atkinson, S. A. 1957 Preliminary results of low speed wind tunnel tests on a gothic wing of aspect ratio 1.0. *Tech. Rep.*. Aeronautical Research Council. 74

Pier, B. 2002 On the frequency selection of finite-amplitude vortex shedding in the cylinder wake. *Journal of Fluid Mechanics* **458**, 407–417. 8

Pier, B. & Huerre, P. 2001 Nonlinear self-sustained structures and fronts in spatially developing wake flows. *Journal of Fluid Mechanics* **435**, 145–174. 8

Pier, B., Huerre, P. & Chomaz, J.-M. 2001 Bifurcation to fully nonlinear synchronized structures in slowly varying media. *Physica D* **148**, 49–96. 75, 79, 96

Poinsot, T. & Veynante, D. 2005 *Theoretical and Numerical Combustion*. R T Edwards. 30

Qadri, U. A. & Juniper, M. P. 2012 A theoretical approach to the passive control of spiral vortex breakdown. UKACC International Conference on Control, 3-5 September 2012, Cardiff, UK. 73

Qadri, U. A., Mistry, D. & Juniper, M. P. 2013 Structural sensitivity of spiral vortex breakdown. *Journal of Fluid Mechanics* **720**, 558–581. 73

Ranga Dinesh, K. K.J., Jenkins, K. W., Kirkpatrick, M. P. & Malalasekera, W. 2009 Identification and analysis of instability in non-premixed swirling flames using LES. *Combustion Theory and Modelling* **13** (6), 947–971. 153

Rayleigh, Lord 1878*a* The explanation of certain acoustical phenomena. *Nature* **18**, 319–321. 177

Rayleigh, Lord 1878*b* On the instability of jets. *Proceedings of the London Mathematical Sociey* **10**, 4–13. 177

Rayleigh, Lord 1880 On the stability, or instability, of certain fluid motions. *Proceedings of the London Mathematical Society* **11**, 57–70. 3

Reynolds, O. 1884 An experimental investigation of the circumstances which determine whether the motion of water shall be direct or sinuous, and of the law of resistance in parallel channels. *Philosophical Transactions of the Royal Society* **174**, 935–982. 3

Ruith, M. R., Chen, P., Meiburg, E. & Maxworthy, T. 2003 Three-dimensional vortex breakdown in swirling jets and wakes: direct numerical simulation. *Journal of Fluid Mechanics* **486**, 331–378. 75, 76, 77, 78, 79, 80, 81, 82, 93, 103, 110

Salwen, H. & Grosch, C. E. 1981 The continuous spectrum of the Orr-Sommerfeld equation. Part 2: Eigenfunction expansions. *Journal of Fluid Mechanics* **104**, 445–465. 6

Schmid, P. J. 2007 Nonmodal stability theory. *Annual Review of Fluid Mechanics* **39**, 129–162. 6

Sheard, G. J., Hourigan, K. & Thompson, M. C. 2005 Computations of the drag coefficients for low-Reynolds-number flow past rings. *Journal of Fluid Mechanics* **526**, 257–275. 58

Sipp, D., Marquet, O., Meliga, P. & Barbagallo, A. 2010 Dynamics and control of global instabilities in open flows: a linearized approach. *Applied Mechanics Review* **63** (030801). 8

Sivakumar, R. & Chakravarthy, S. R. 2008 Experimental investigation of the acoustic field in a bluff-body combustor. *International Journal of Aeroacoustics* **7** (3-4), 267–299. 2

Spall, R. & Snyder, D. 1999 Numerical simulations of vortex breakdown: Review and recent developments. *Recent Res. Developments on Heat, Mass and Momentum Transfer* **2**, 41–70. 75

Sreenivasan, K. R., Raghu, S. & Kyle, D. 1989 Absolute instability in variable density round jets. *Experiments in Fluids* **7**, 309–317. 50

Srinivasan, V., Hallberg, M. P. & Strykowski, P. J. 2010 Viscous linear stability of axisymmetric low-density jets: Parameters influencing absolute instability. *Physics of Fluids* **22** (024103). 50, 56

Strykowski, P. J. & Sreenivasan, K. R. 1990 On the formation and suppression of vortex 'shedding' at low Reynolds numbers. *Journal of Fluid Mechanics* **218**, 71–107. 7

Syred, N. 2006 A review of oscillation mechanisms and the role of the precessing vortex core (PVC) in swirl combustion systems. *Progress in Energy and Combustion Science* **32**, 93–161. 2

Tammisola, O. 2011 Numerical stability studies of one-phase and immiscible two-phase jets and wakes. PhD thesis, KTH Mechanics, Sweden. 8

Tammisola, O. 2012 Oscillatory sensitivity patterns for global modes in wakes. *Journal of Fluid Mechanics* **701**, 251–277. 87

Theofilis, V. 2003 Advances in global linear instability analysis of non-parallel and three-dimensional flows. *Progress in Aerospace Sciences* **39**, 249–315. 44

Toong, T.-Y., Salant, R. F., Stopford, J. M. & Anderson, G. Y. 1965 Mechanisms of combustion instability. *Proceedings of the Combustion Institute* pp. 1301–1313. 148, 149

Trefethen, L. N., Trefethen, A. E., Reddy, S. C. & Driscoll, T. A 1993 Hydrodynamic stability without eigenvalues. *Science* **261**, 578–584. 7

Vyazmina, E., Nichols, J. W., Chomaz, J.-M. & Schmid, P. J. 2009 The bifurcation structure of viscous steady axisymmetric vortex breakdown with open lateral boundaries. *Physics of Fluids* **21** (074107). 75

Wygnanski, I., Champagne, F. & Marasli, B. 1986 On the large-scale structures in two-dimensional small-deficit, turbulent wakes. *Journal of Fluid Mechanics* **168**, 31–71. 2

Zebib, A. 1987 Stability of viscous-flow past a circular-cylinder. *Journal of Engineering Mathematics* **21**, 155–165. 6